

Coupled roto-translational motion of the heliogyro applied to Earth-Mars cyclers

Master Thesis

Guido Monechi

Delft University of Technology

Coupled roto-translational motion of the heliogyro applied to Earth-Mars cyclers

Master Thesis

by

Guido Monechi

to obtain the degree of Master of Science
at the Delft University of Technology,
to be defended publicly on Friday February 10, 2023 at 9:30 AM.

Student number	4559827	
Project Duration:	August, 2021 - February, 2023	
Supervisor:	Dr. M. J. Heiligers	
Thesis committee:	Dr. P. N. A. M. Visser	Chair
	Dr. M. J. Heiligers	Supervisor
	Dr. A. Cervone	Examiner

Cover: Heliogyro concept from “Macneal-Schwendler corporation, Heliogyro preliminary design, Phase II Final Report, 1978”; High-resolution picture available at <https://www.planetary.org/space-images/heliogyro-solar-sail> [Last accessed on 25/01/2023]

An electronic version of this thesis is available at <http://repository.tudelft.nl/>.

Preface

This master thesis represents the conclusion of my studies (up until now...), a process that brought me all over the world and accompanied throughout most of my life. It consisted of many up and downs, unexpected delays (the length of my master thesis project for example), but also a lot of personal development and great times.

First and foremost, I would like to thank my thesis supervisor, Jeannette Heiligers, for all the incredible help she gave me throughout my thesis projects (both Bachelor and Master!). Working with you has been a pleasure, I could always express all doubts and issues and you always guided me towards the right direction. Your feedback has always been precise, on point, and complete, greatly increasing the quality of my work and making this research project an invaluable learning experience for me.

I would like to express my gratitude to all my friends in Italy, the Netherlands and Luxembourg for the support throughout these few years, especially the ones that shared with me many long working days at the Fellowship or the Aerospace faculty: Tullio, Nicolas, Roderick, Emilie, Michael and many others.

Special thanks to Charly who has been by my side for most of my master thesis project. We shared common doubts and struggles, but also many accomplishments and good times. Throughout the whole process you supported me, understood me, and motivated me like no one else could (as well as giving me a sunny place where to work and escape the cloudy and rainy weather of the Netherlands and Luxembourg...). Our weeks together in Spain and Portugal have been for sure the best times I had in the past year.

Finally, I would like to thank all my family for always encouraging me and supporting me in all possible ways. I am happy to finally conclude this big chapter of my life and I am looking forward for all future opportunities!

Guido Monechi
Luxembourg, January 2023

Executive Summary

Solar sailing is a propulsion method that exploits solar radiation pressure from the Sun to generate thrust. This is possible thanks to a large reflective sail which is used to reflect incoming sunlight, increasing the linear momentum of the sailcraft. Compared to traditional propulsion methods, solar sailing does not require propellant and therefore it is a highly attractive solution for high-energy missions. Research on the use of solar sailing as a propellant-less alternative to traditional propulsion methods has been performed since the late 1960s.

The heliogyro is one of the first sailcraft configurations that was investigated, with initial research started by R. H. MacNeal in the late 1960s. This helicopter-like sailcraft configuration consists of many high aspect-ratio reflective sail blades kept in tension by spinning the spacecraft. The orientation of each blade can be independently controlled, therefore affecting both the forces and moments generated by the sail. These characteristics make the heliogyro a promising sailcraft configuration as less structural mass is required to achieve the same sail area compared to traditional designs (which leads to better performance) and no additional attitude control system is needed thanks to the large control authority of the heliogyro over forces and moments.

After the initial investigation by MacNeal, little research has been performed on the heliogyro until recent years. Current research on the heliogyro focuses on the blades' structural dynamics, the sailcraft control moment authority and its potential use for space missions. Most research works related to the sailcraft dynamics and trajectory design do not explicitly model the sailcraft rotational motion and make several limiting assumptions such as ignoring the control of the blades' orientation. The accuracy of the results is therefore limited as the sailcraft translational motion is tightly coupled to its rotational motion and the control of the blades orientation is used to generate both control forces and moments which affect the sailcraft orientation and trajectory.

In order to fill this research gap, this thesis work investigates the coupling between the translational and rotational motions of the heliogyro, by developing and applying a novel model for the sailcraft motion for the design of time-optimal Earth-Mars heliogyro cycler trajectories. Cycler trajectories consist of periodic trajectories between the two planets and are designed using a two-body gravitational model and a simplified planetary ephemerides model. Two models of the coupled roto-translational dynamics of the sailcraft are developed, an averaged one suitable for mission design and a non-averaged for increased accuracy. The continuous optimal control problem describing the time-optimal Earth-Mars cycler trajectories is discretized through a multiple shooting transcription and solved using the software library WORHP ("We Optimize Really Huge Problems").

The resulting heliogyro trajectories are analyzed and compared to an equivalent traditional fixed-area sailcraft. For both sailcraft configurations the cycler period is found to be two synodic periods, demonstrating that the heliogyro can obtain comparable performance as a traditional fixed-area sailcraft without the use of an attitude control system, making it an attractive option for such interplanetary missions. The coupled roto-translational motion of the heliogyro is analyzed in-depth, showcasing the results for both two-dimensional and three-dimensional cases. In addition, it is shown that the averaged model obtains similar results as the more accurate non-averaged one, demonstrating that it is suitable for preliminary design of heliogyro trajectories. Finally, the sensitivity of the heliogyro trajectories is investigated, demonstrating the robustness of the achieved trajectories to changes in sailcraft performance, payload mass and spin rate.

The outcome of this research will serve as a starting point for future heliogyro mission designers, providing a novel dynamical model for preliminary trajectory design and an initial analysis on the capabilities of the heliogyro for interplanetary missions, highlighting the differences and potential advantages of the heliogyro compared to traditional fixed-area sailcraft.

Contents

Preface	i
Executive Summary	ii
Nomenclature	vi
1 Introduction	1
1.1 Solar Sailing	1
1.2 Heliogyro	2
1.3 Orbital cyclers	3
1.4 Research objective and questions	3
1.5 Report structure	4
2 Research article	5
3 Conclusion and recommendations	31
3.1 Conclusion	31
3.2 Recommendations	32
A Reference frames transformations	37
B Verification and validation	39
B.1 Verification	39
B.1.1 Reference frames transformations	39
B.1.2 SRP Forces and Moments	39
B.1.3 Dynamics	41
B.1.4 Multiple Shooting algorithm	46
B.2 Validation	47
B.2.1 Dynamics	48
B.2.2 Multiple shooting	50
C Numerical parameters selection	55
C.1 Constraint tolerance selection	55
C.2 Integrator step selection	55
C.3 Average force/ moment computation step selection	56
C.4 Numerical derivative step selection	56

List of Figures

1.1	Solar-sails configurations from [11]. From left to right: Square sail, Spinning disk sail, Heliogyro.	2
B.1	SRP forces (figures a) and c), <i>Inertial</i> reference frame) and moments (figures b) and d), <i>Despun</i> reference frame) corresponding to cases eight (figures a) and b)) and nine (figures c) and d)). Non-averaged results displayed with solid line, averaged with dashed lines.	40
B.2	Verification of SRP force and moment models, varying cone angle. Results from the implemented model in plot a), while the original results from Figure 4 of [37] in plot b).	42
B.3	Verification of SRP forces and moment models, varying pitch profiles. Results from the implemented model in plot a), the original results from Figure 5 of [37] in b).	43
B.4	Visualization of geometry and sail orientation for Cases 1 and 2 of the translational dynamics verification.	44
B.5	Closed Non-Keplerian orbit for heliogyro dynamics validation. Position and velocity of the heliogyro shown respectively in Figures a) and b), while the cone angle of the sailcraft plotted as a function of time in Figure c).	45
B.6	Visualization of the verification problem iteration process.	47
B.7	Visualization of resulting Jacobian and associated errors, multiple shooting implementation in plot a), fully numerical one in b), and the difference in c).	48
B.8	Comparison between propagated Earth-Mars spiral trajectory in a) and trajectory from [1] in b).	49
B.9	Difference between analytical and numerical solution for torque free motion of an axis-symmetric body. Figure a) (top and bottom row) shows the numerical solution, b) the analytical one, and c) the difference between the two.	51
B.10	Difference between analytical and numerical solution for constant lateral moment motion of spinning sailcraft. Figure a) (top and bottom row) shows the numerical solution, b) the analytical one, and c) the difference between the two.	51
B.11	Benchmark, initial and optimal solution trajectory related to the 1D Goddard's rocket problem [48].	53
B.12	Initial, perturbed and optimal solution trajectory related to the multiple shooting algorithm validation.	54
C.1	Final position error analysis as a function of integrator time-step, for segments in the EM and ME leg.	56
C.2	Averaged SRP force and moment model errors as a function of numerical integration steps.	57
C.3	Sensitivities of numerical derivative to numerical steps.	57

List of Tables

B.1	Optimal result of the verification problem.	47
B.2	States and controls used for heliogyro problem validation. All values scaled as explained in the paper, positions in AU, velocity in AU/syn periods, angles in radians, angular speeds in RPM.	48
B.3	Parameters of Goddard's rocket 1D problem [48].	52
B.4	Initial state, control and perturbation for the heliogyro multiple shooting validation. . . .	52

Nomenclature

List of acronyms

Acronym	Definition
ACS	Attitude Control System
ACS3	Advanced Composite Solar Sail System
EM	Earth-Mars
IAC	International Astronautical Conference
JAXA	Japan Aerospace eXploration Agency
ME	Mars-Earth
MMOI	Mass Moment Of Inertia
NASA	National Aeronautics and Space Administration
NEA	Near-Earth Asteroid
NKO	Non-Keplerian Orbit
NLP	Non-Linear Programming
RCD	Reflectivity Control Devices
RK	Runge-Kutta
RPM	Rotations Per Minute
SRP	Solar Radiation Pressure
STM	State Transition Matrix

List of symbols

Symbol	Definition
A	Area
a	Heliogyro parameter used in Appendix B
acc	Acceleration
B	<i>Body</i> reference frame
$\hat{\mathbf{b}}_i$	<i>Body</i> reference frame i^{th} axis
C	Arbitrary constant used in Appendix B
D	<i>Despun</i> reference frame
$\hat{\mathbf{d}}_i$	<i>Despun</i> reference frame i^{th} axis
\mathbf{F}	Force vector
\mathbf{f}	Fitness vector
H	Angular momentum magnitude
\mathbf{H}	Angular momentum vector
I	<i>Inertial</i> reference frame
$\hat{\mathbf{i}}_i$	<i>Inertial</i> reference frame i^{th} axis
J	Mass moment of inertia
k	Arbitrary constant used in Appendix B
L_i	<i>Blade i</i> reference frame
\uparrow	<i>Solar</i> reference frame second axis
m	Mass
\mathbf{M}	Moment vector
N	Number of variable defined by subscript
$\hat{\mathbf{p}}$	<i>Solar</i> reference frame third axis
P	Orbital period
r	Position magnitude

Symbol	Definition
R	Rotation matrix
r	Sailcraft position vector
<i>S</i>	<i>Solar</i> reference frame
\$	<i>Solar</i> reference frame first axis
<i>T</i>	Thrust magnitude
<i>t</i>	Time
<i>V</i>	Velocity
<i>u</i>	Control input variable
U	Guidance input vector
u	Control input vector
<i>x</i>	Arbitrary variable
X	State vector
x	Arbitrary vector
α	Cone angle
β	Sail lightness number
γ	Arbitrary angle
θ	Second Euler angle describing heliogyro orientation
φ_i	Blade <i>i</i> pitch angle
Λ	Drag
λ	Arbitrary variable used in Appendix B
μ	Standard gravitational parameter
ξ_i	Angle between blade <i>i</i> and blade 1
ρ	Density
ϕ	First Euler angle describing heliogyro orientation
χ	Vector of design variables
ψ	Third Euler angle describing heliogyro orientation
ψ_i	Blade <i>i</i> orientation angle
ω	Angular velocity vector
<u>Other notation</u>	
$\dot{\square}$	First order time derivative
$\hat{\square}$	Unit-vector
$[IJ]$	Rotation from reference frame <i>I</i> to <i>J</i>
$\Delta\square$	Change in variable
<u>Superscripts</u>	
\overline{T}	Transposed
$[*]$	Expressed in reference frame *
<u>Subscripts</u>	
0	Initial
1, 2, 3	Denote axis of a reference frame
<i>b</i>	Blades
<i>base</i>	Baseline
<i>eff</i>	Effective
<i>f</i>	Final
<i>hp</i>	Half-p pitch profile
<i>max</i>	Maximum
<i>r</i>	Reduced
<i>rad</i>	Radial
<i>SRP</i>	Solar Radiation Pressure
<i>t</i>	Transfer
<i>tang</i>	Tangential
\odot	Sun

1

Introduction

This chapter introduces the required background for important concepts related to this thesis work and presents the relevance of the research work. Firstly, an historical and technical background of solar sailing is given in section 1.1, followed by a description of the heliogyro in section 1.2. Later, the concept of orbital cyclers is introduced in section 1.3, with a special focus on the use of solar-sail propulsion for such trajectories. Finally, the research objective and questions are presented in section 1.4, followed by an overview of the structure of this thesis report in section 1.5.

1.1. Solar Sailing

Solar sailing is a promising propulsion method that exploits Solar Radiation Pressure (SRP) reflecting over large reflective surfaces (the sail) to generate thrust [1]. Compared to traditional propulsion methods, it does not require propellant and therefore it is a highly attractive solution for high-energy missions [2].

The idea that light could exert pressure was first theorized by J. C. Maxwell in 1873 and experimentally proved by P. Lebedew in 1900 [1, 3]. In the 1920s, F. Sanders and K. Tsiolkovsky were the first to suggest that SRP could propel spacecraft [1, 3, 4]. Nonetheless, the concept of solar sailing was not developed until the 1950s/1960s, when the first mentions and research about solar sails appeared in fiction and scientific literature [1, 4]. In the 1970s National Aeronautics and Space Administration (NASA) initiated efforts to develop a mission to rendezvous with Halley's comet which was about to approach its perihelion in 1986. This was the first mission where solar sailing was seriously considered as one of the potential propulsion methods and several studies were performed analyzing the feasibility of different solar-sailing concepts [1, 4]. In the end, solar-electric propulsion was chosen over solar sailing as a propulsion method and the mission was later canceled due to budget constraints [1].

Research and development of solar sailing continued in later years, culminating with the launch of first sailcraft in space, IKAROS, by Japan Aerospace eXploration Agency (JAXA) in 2010 [5]. After IKAROS, three other sailcraft were sent to space: NanoSail-D2, LightSail-1 and LightSail-2 [6, 7]. Recently, Artemis I was launched carrying the Near-Earth Asteroid (NEA) Scout mission, a sailcraft with the objective to rendezvous and explore a NEA [8]. Several other sailcraft missions have been proposed and may be launched in the near-future, such as Advanced Composite Solar Sail System (ACS3) and the Solar Cruiser Mission [9, 10].

In order to generate a suitable amount of thrust, sails need to be extremely large and light. Common parameters used to describe the sailcraft performance are the lightness number, the characteristic acceleration and the solar loading parameter. Different sail configurations have been proposed over the years, with the main ones illustrated in Figure 1.1.

The square sail configuration (also called "traditional fixed-area sail" configuration in this document) consists of a fixed-area sail supported by rigid spars which provide stiffness and load-bearing functions to the sail. Most of the aforementioned launched missions use this configuration as it is the most common sail design due to its relative simplicity. The main downsides of this configuration are the high support structure weight and the complexity of the deployment [1].

Disk solar-sail designs utilize a central hub and a flexible sail which is deployed and kept in tension by

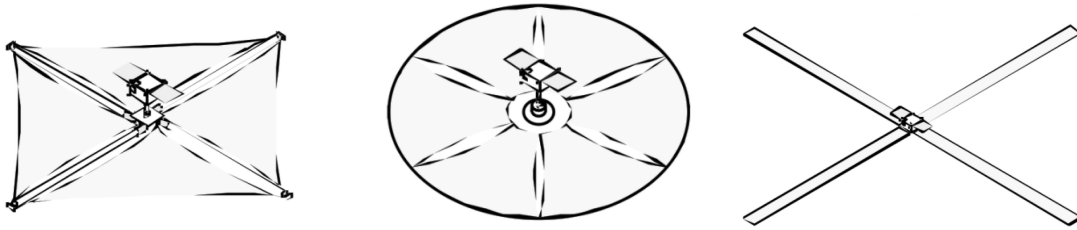


Figure 1.1: Solar-sails configurations from [11]. From left to right: Square sail, Spinning disk sail, Heliogyro.

spinning the sailcraft. Additional structures such as radial spars and an external hoop might be needed for additional rigidity. The main advantage of this design compared to the previous configuration is the lower structural mass as structural rigidity is provided by the spin of the sailcraft [1, 3].

The heliogyro is a similar concept to disk solar sails and relies on its rotation to maintain the tension of the sail. The sail consists of multiple high aspect-ratio blades whose pitch angle can be independently controlled, similarly to a helicopter rotor. This configuration allows for easy packing and deployment (through spin), as well as reduced structural mass and potentially higher control authority. The main downsides compared to other configurations are structural uncertainties related to the sail membrane, such as bending and twisting [1, 3]. A more in-depth description of the heliogyro concept is given in section 1.2.

In general, direction and magnitude of the SRP force exerted by the sail can be controlled by varying the sail orientation relative to the Sun. In traditional fixed-area square sails and spinning disk solar sails, the attitude of the sail needs to be modified through the use of an independent Attitude Control System (ACS). Similarly to traditional spacecraft, thrusters and reaction wheels can be used to generate the control moment, but they are usually inefficient for sailcraft due to the large mass moment of inertia of the sail [12]. Changing the position of the center of mass of the sailcraft is an effective method to generate control moments, for example by using moving masses actuated by control-booms [12–15]. Alternatively, one of the most common methods is the use of control vanes, small sails placed at the corners of the main sail, whose orientation can be modified to generate moments on the sailcraft [12, 13, 16]. Another popular attitude control method (used by IKAROS [17]) is the use of Reflectivity Control Devices (RCD) which control the reflectivity characteristics of the sail surface, therefore allowing for the modulation of thrust and generation of moments [18]. In contrast to the aforementioned methods, the heliogyro can modulate and orient SRP forces by modifying the orientation of the blades, generating control moments without the need of an additional ACS, as further discussed later in section 1.2.

1.2. Heliogyro

As discussed in section 1.1, the heliogyro is a specific design of spinning solar-sail consisting of several high-aspect ratio reflective sail blades that maintain their stiffness by spinning the sailcraft. Stowage and deployment are simple as the flexible blades can be stowed in spools which can be deployed by the centrifugal forces generated by the spacecraft spin [19]. Attitude control of the spacecraft and thrust vector control can be achieved by pitching each blade independently. The blade pitch can be achieved by rotary actuators at the root of each blade [19, 20], which can also be complemented by the use of RCDs at the blade tip to reduce issues related to torsional stability and bending [21]. Overall, the heliogyro has significant advantages over traditional fixed-area square sailcraft: structural weight can be reduced as less supporting structure is needed and stowage and deployment is easier [22]. However uncertainties on the structural stability of the blades exist, as well as the inherent issue of spinning sails due to their large angular momentum which leads to more issues for the sailcraft attitude control compared to three-axis stabilized sailcraft [1, 3].

The heliogyro sailcraft concept was first proposed by R. H. MacNeal in 1967 [23] and further developed as one of the potential concepts for NASA's Halley's comet rendezvous mission [24]. The design was selected over a traditional square fixed-area sailcraft due to its advantages in the deployment phase [4] but was later abandoned in favor of a solar-electric propulsion solution [1]. Interest in and research on the heliogyro subsided over the following years, with a few exceptions such as a design study by a group of MIT students in the 1990s and subsequent follow-up research by R. Blomquist, one of the original group members [25, 26]. In the 2010s, renewed interest in solar sailing led to further re-

search on the heliogyro, culminating with the HELIOS mission proposal by NASA [19, 27]. The HELIOS mission concept consisted of a low-cost heliogyro based on the design from MIT [25], with the objective of demonstrating several technologies associated with the heliogyro [27]. The most complete overview of past and recent research on the heliogyro is given in the PhD thesis of D. Guerrant [22]. Recent research about the heliogyro focuses on several of the most uncertain parts of the design. Potential issues related to structural stability and dynamics of the long flexible blades have been investigated [20, 28–31], but no unsolvable stability and control issues have been found for the heliogyro sail membranes [27]. Further research has been performed on the control of the heliogyro and its potential for space missions [32–36]. Nonetheless, several unknowns about the sailcraft motion still remain.

In order to control the forces and moments generated by the sailcraft, the orientation (pitch angle) of the blades can be modified. Taking inspiration from helicopters, literature proposes the use of three blade pitch profiles to define the law controlling the pitch angles of the blades: collective, cyclic, and half-p [27]. The inverse mapping from desired SRP force and moment to the blades pitch profiles is non-trivial and does not have a general analytical solution [33]. D. Guerrant and D. Lawrence investigated the control moment authority of the heliogyro, proposing several attitude control tactics for different mission scenarios and analyzing the influence of each pitch profile on the generated control moments [22, 37]. J. Heiligers, D. Guerrant, and D. Lawrence complemented the previous work by analyzing the orbit control authority of the heliogyro for solar-sail halo orbits, demonstrating that the heliogyro outperforms traditional fixed-area sailcraft for orbit control [32]. As both attitude and orbital control are performed by controlling the orientation of the blades, the rotational and translational motion of the sailcraft are tightly coupled. Nonetheless, most existing studies on the heliogyro do not model explicitly the control input defining the pitch profile of the blades and often ignore the sailcraft rotational motion by simply simulating its translational motion.

1.3. Orbital cyclers

Orbital cyclers are a type of trajectory which periodically move between two celestial bodies. Cyclers have a period equal to a multiple of the synodic period of the two celestial bodies. The most famous cycler is the Aldrin cycler, a simple cycler trajectory between Earth and Mars [38]. The main issues with cyclers that use traditional propulsion methods are the need for frequent and high-energy maneuvers to ensure the continuity of the cycler and the high relative velocity between the spacecraft and the planets during the encounters [38].

Solar-sail cyclers provide an elegant solution directly tackling the two main issues of cyclers which use traditional propulsion. By using solar-sail propulsion the high-energy requirements of the trajectory can be satisfied without the need for additional propellant, removing the relative velocity between the planet and the sailcraft during the planetary encounters [39–41]. Preliminary studies have investigated the feasibility and potential of these solar-sail “stop-over” cyclers, showing that cycler trajectories between Earth and Mars with a period of two or three synodic periods (approximately 4–6 years) are possible with mid-term sail performance [39–41].

Such periodic trajectories could for example be used to support the human exploration and settlement of Mars, by providing a continuous logistic link between the two planets.

1.4. Research objective and questions

As mentioned in the previous sections, the motion and control of the heliogyro have been analyzed in the past [32, 37] using several simplifying assumptions and without considering the coupling between the rotational and translational dynamics. This research work will focus on filling this gap with the following research objective: “Investigating the coupled roto-translational motion of the heliogyro and evaluating its performance and capabilities compared to fixed-area sails for time-optimal Earth-Mars cycler trajectories; by developing a model of the heliogyro’s coupled roto-translational dynamics and designing, simulating, and analyzing time-optimal cycler trajectories as a function of payload ratio, using mid-term sail performance”. From the research objective, the following research questions are defined:

1. How can the rotational and translational motions of the heliogyro be coupled?
2. How can time-optimal heliogyro Earth-Mars cycler trajectories be designed while considering the coupled roto-translational motion of the sailcraft?

3. Can the heliogyro obtain similar performances as an equivalent fixed-area sailcraft for an Earth-Mars cyler, without the need for a separate ACS?
4. How sensitive are heliogyro time-optimal Earth-Mars cyler trajectories to the sailcraft design parameters such as lightness number, payload ratio and spin-rate?

1.5. Report structure

The core of the thesis work is the research paper titled “Coupled roto-translational motion of the heliogyro applied to Earth-Mars cyclers” included in chapter 2. This paper was presented at the International Astronautical Conference (IAC) in Paris in September 2022 and is included in the conference proceedings.

Within the research article, a detailed background of the existing research on the heliogyro is given in section 1. In section 2 the models of the SRP force and moment acting on the sail are developed, followed by the model of the heliogyro’s coupled roto-translational dynamics in section 3. The used heliogyro design and the optimal control problem are described in section 4, followed by an explanation of the adopted trajectory design approach in section 5. Finally, the results are presented in section 6 and the conclusions are provided in section 7.

After the research article, the conclusions and recommendations are presented in chapter 3. Finally, appendices A, B and C contain a description of the reference frames transformations used throughout the research work, the verification and validation procedures, and the rationale behind the selection of several numerical parameters used, respectively.

2

Research article

Coupled roto-translational motion of the heliogyro applied to Earth-Mars cyclers*

Guido Monechi^a

^a*Faculty of Aerospace Engineering, Delft University of Technology, Kluyverweg 1, Delft, The Netherlands 2629 HS, G.Monechi@student.tudelft.nl*

**Based on the manuscript presented at the International Astronautical Congress, IAC 2022, Paris, France, 18-22 September 2022. Copyright by IAF*

Solar sailing is a flight-proven low-thrust propulsion technology with strong potential for innovative scientific missions. All previous solar-sail missions employed a solar-sail system design consisting of four triangular sail quadrants supported by deployable booms. As an alternative to such a fixed and flat sail-system design, this paper investigates the dynamics of the heliogyro. The heliogyro is a helicopter-like sail design that utilizes a set of long slender blades which are deployed and flattened by spin-induced tension and whose orientations can be individually controlled. The main advantages of such a design are the easier stowage and deployment, and potentially lower structural mass. Moreover, the individual blade orientation allows higher authority on the forces and moments produced by the sail, but at the same time complicates the heliogyro dynamics. The heliogyro's translational and rotational motions are strongly coupled, with non-trivial relationships between the control inputs and the forces and moments produced by the sail. The purpose of this paper is to investigate, for the first time, the coupled roto-translational motion of the heliogyro. As tantalizing application, the paper analyzes the heliogyro's performance for Earth-to-Mars stopover cycler trajectories, which could aid the exploration of Mars by providing recurrent propellant-less logistics links between Earth and Mars. Two numerical models to describe the heliogyro coupled roto-translational dynamics are derived; a spin-averaged and a non-averaged model. To design time-optimal heliogyro Earth-to-Mars stopover cycler trajectories, a multiple shooting algorithm is employed and the feasibility of the concept is demonstrated. The resulting trajectories are then compared to those of a traditional fixed-area and flat sail-system design, demonstrating that the heliogyro can perform similar trajectories as the traditional fixed-area and flat sailcraft, without the need for an additional system to control the sailcraft attitude.

Nomenclature

Symbols			
A	Total sail area	r	Distance
$\mathcal{A}\mathcal{R}$	Aspect ratio	\mathbf{r}	Position vector
a	Amplitude angle pitch profiles	\mathbf{S}	Sensitivity matrix
\mathbf{a}	Acceleration vector	\mathbf{s}	Solar radiation direction
\mathbf{b}	Boundary condition vector	\mathbf{U}	Guidance input vector
C	Speed of light	\mathbf{u}	Control vector
c	Chord length	\mathbf{X}	State vector
\mathbf{c}	Defect constraint vector	α	Cone angle
\mathbf{F}	Force vector	β	Sail lightness number
\mathbf{f}	Fitness vector	β_0	Sail lightness number with no payload
\mathbf{I}	Identity matrix	δ	Clock angle
J	Mass moment of inertia	ϵ	Bus mass ratio
\mathbf{J}	Mass moment of inertia matrix	η	Sail efficiency
k	Constant	θ	Second sailcraft attitude angle
L	Luminosity	ϑ_i	Blade i pitch angle
\mathbf{M}	Moment vector	$\boldsymbol{\kappa}$	Smoothness constant vector
m	Mass	λ	Payload ratio
N	Number	μ	Standard gravitational parameter
$\hat{\mathbf{n}}$	Sail normal direction	ξ_i	Angle between blade i and blade 1
O	Objective	σ	Solar loading parameter
P	Solar radiation pressure	$\boldsymbol{\Upsilon}$	Planetary target state
R	Blade span	\mathbf{v}	Additional target constraints vector
		Φ	State transition matrix
		ϕ	First sailcraft attitude angle

φ	Phase angle pitch profiles
χ	Vector of design variables
ψ	Third sailcraft attitude angle
ψ_i	Blade i orientation angle
ω	Angular velocity vector

Other notation

$\dot{\square}$	First order time derivative
$\ddot{\square}$	Second order time derivative
$\hat{\square}$	Unit-vector
$\bar{\square}$	Averaged value
$[IJ]$	Rotation from reference frame I to J

Superscripts

E	Earth
k	Denotes k phase/leg
M	Mars
T	Transposed
$[*]$	Expressed in reference frame *

Subscripts

$\bar{1}, 2, 3$	Denote axis of a reference frame
a	Arrival
b	Blade
bus	Bus
c	Cycler
co	Collective
cy	Cyclic
d	Departure
e	Empty
hp	Half-pitch
pv	Position-velocity
r	Reduced
t	Transfer
s	Segments
sa	Sail system
syn	Synodic
sc	Sailcraft
u	Payload
w	Waiting
\odot	Sun

Acronyms

ACS	Attitude Control System
EM	Earth-Mars
ME	Mars-Earth
MMOI	Mass Moment Of Inertia
NLP	Non-Linear Programming
RPM	Rotations Per Minute
SRP	Solar Radiation Pressure
STM	State Transition Matrix

1. Introduction

Solar sailing is a promising propulsion method that exploits the Solar Radiation Pressure (SRP) over a large highly reflective sail membrane to generate thrust [1]. It is a highly attractive option for high-energy missions and space exploration as the thrust is produced without the use of propellants [1]. Solar sailing was first considered as an option in the early 1970s for the design of the Comet Halley Rendezvous Mission, which was later canceled [1]. Since then, solar-sailing technology has significantly progressed and its feasibility has been proven by missions such as IKAROS [2], NanoSail-D2 [3], and LightSail 1 and 2 [4]. Exciting upcoming missions such as NEA Scout [5], Solar Cruiser [6], and ACS3 [7] will continue to increase the technology readiness level and further establish solar sailing as a serious option for any future solar-system exploration mission.

The solar-sail designs of all previously mentioned missions consist of a square-shaped fixed-area sail supported by deployable booms, but other sailcraft designs have been proposed as well. Among the alternative sailcraft designs, the heliogyro stands out as a promising option due to the many potential advantages over square-shaped fixed-area sailcraft. The heliogyro was developed by Richard MacNeal in the late 1960s and was one of the two sailcraft designs proposed for the aforementioned Comet Halley Rendezvous Mission [1, 8, 9].

The heliogyro sailcraft consists of a central hub where the bus and payload are located and several slender sail blades kept in tension by spinning the sailcraft. The orientation of the sail blades (pitch angle) can be modified to control the generated SRP forces and moments, thereby giving the sailcraft a higher control authority compared to traditional fixed-area sailcraft [10, 11]. As moments can be generated and controlled by pitching the sail blades, no separate Attitude Control System (ACS) for the heliogyro is needed, in contrast to fixed-area solar sails that need a system such as sail vanes, sliding masses, or reflectivity control devices to control the sailcraft attitude [12, 13]. As the heliogyro's blades can be stored on spools during launch and can be deployed through the sailcraft spin, the heliogyro has a significantly easier stowage and deployment process compared to traditional fixed-area solar sails. In addition to that, less supporting structure is required to support the sail thanks to the spin-induced rigidity, potentially allowing for lower mass, larger sailcraft performance, and better scalability compared to traditional fixed-area sailcraft [1].

After the initial developments by MacNeal [8, 9] and subsequent research on the heliogyro by

Blomquist [14, 15, 16], limited research was performed in the following years. Interest in the heliogyro increased again in the 2010s with NASA’s HELIOS mission proposal [17], a conceptual low-cost sailcraft to showcase heliogyro technology developments ongoing at NASA [18]. A complete overview of the heliogyro sailcraft design and ongoing research is given in Guerant’s PhD thesis [19]. Current research about the heliogyro is focused on the major uncertainties of the sailcraft concept: the dynamics, structural stability, and control of the flexible sail blades [20, 21, 22, 23]; as well as the modeling of the rotational and translational dynamics of the sailcraft for mission design [10, 24, 25, 26].

In the scarce amount of research on the heliogyro, the rotational and translational dynamics of the sailcraft are usually analyzed independently. Limiting assumptions are often introduced, such as modeling the sailcraft’s area as variable and neglecting the sail blades’ orientations. These sail blades’ orientations directly control *both* the SRP forces and moments generated by the sail, which directly influence *both* the rotational and translational motion of the sailcraft. Such forces and moments are strongly dependent on the position and orientation of the sailcraft relative to the Sun. The rotational and translational dynamics of the sailcraft are therefore tightly coupled and should be analyzed as such.

The purpose of this paper is to develop, for the first time, two models describing the *coupled* roto-translational dynamics of the heliogyro: a spin-averaged model and a non-averaged model. The non-averaged model models the heliogyro rotational motion including the spin-rotation, while the spin-averaged model only models the translational and spin-axis motion, averaging the forces and moments over the heliogyro’s spinning rotation. This spin-averaged model is used to design heliogyro stop-over cycler trajectories between Earth and Mars for validation and to showcase its capabilities. A stop-over solar-sail cycler between Earth and Mars can provide a continuous propellant-less logistic connection between the two planets, periodically transporting cargo without the need for refueling. Solar-sail cyclers have been analyzed in the past [27, 28, 29] demonstrating that a solar-sail cycler with a period of two Earth-Mars (EM) synodic periods (approximately 780 Earth days) is possible with mid- to far-term sailcraft performance [28, 29].

To achieve the aforementioned purpose, this paper is organized as follows. Firstly, in section 2, the heliogyro SRP forces and moments models are described. These models are used for the development of the sailcraft coupled roto-translational dynamics,

presented in section 3. Section 4 defines the cycler problem analyzed in this paper, while the trajectory design methodology is presented in section 5. The resulting heliogyro cycler trajectories are presented in section 6 with a comparison to equivalent fixed-area sailcraft cycler trajectories and an analysis of the coupled roto-translational motion of the heliogyro. The conclusions are presented in section 7.

2. Heliogyro force & moment models

In this section, the models to compute the heliogyro SRP force and moment vectors are presented. Firstly, in subsection 2.1, a set of reference frames are defined. Later, in subsection 2.2, the “pitch profiles” describing the sail blade orientation are presented, followed by the non-averaged and spin-averaged force and moment models in subsections 2.3 and 2.4, respectively.

2.1 Reference frames definition

Several reference frames need to be defined to model the heliogyro dynamics. Note that the reference frames in this work slightly differ from the ones in similar works on the heliogyro [10, 11, 24].

Firstly, two Sun-centered reference frames are defined and visualized in Figure 1. The *Solar* reference frame $S(\hat{\mathbf{s}}, \hat{\mathbf{I}}, \hat{\mathbf{p}})$ is defined with axis $\hat{\mathbf{s}}$ along the Sun-spacecraft vector, $\hat{\mathbf{I}}$ parallel to the ecliptic plane and perpendicular to $\hat{\mathbf{s}}$, and axis $\hat{\mathbf{p}}$ that completes the right-handed reference frame ($\hat{\mathbf{p}} = \hat{\mathbf{s}} \times \hat{\mathbf{I}}$). The *Solar* reference frame is complemented by the *Inertial* reference frame $I(\hat{\mathbf{i}}_1, \hat{\mathbf{i}}_2, \hat{\mathbf{i}}_3)$, which does not rotate during the propagation of the dynamics, with $\hat{\mathbf{i}}_1$ along the same direction as the J2000 epoch mean vernal equinox, $\hat{\mathbf{i}}_3$ normal to the mean ecliptic plane, and $\hat{\mathbf{i}}_2$ completing the frame ($\hat{\mathbf{i}}_2 = \hat{\mathbf{i}}_3 \times \hat{\mathbf{i}}_1$). This frame is used as a base frame for all propagations as it is inertial.

Two other frames are defined, both with the origin at the center of mass of the heliogyro. First, the *Body* reference frame $B(\hat{\mathbf{b}}_1, \hat{\mathbf{b}}_2, \hat{\mathbf{b}}_3)$ is defined with $\hat{\mathbf{b}}_1$ along blade 1, $\hat{\mathbf{b}}_3$ along the heliogyro spin-axis, and $\hat{\mathbf{b}}_2$ completing the right-handed frame ($\hat{\mathbf{b}}_2 = \hat{\mathbf{b}}_3 \times \hat{\mathbf{b}}_1$). The direction of the $B(\hat{\mathbf{b}}_1, \hat{\mathbf{b}}_2, \hat{\mathbf{b}}_3)$ frame relative to the $I(\hat{\mathbf{i}}_1, \hat{\mathbf{i}}_2, \hat{\mathbf{i}}_3)$ frame is described through a rotation sequence of three Euler angles (3-2-3) ϕ , θ , and ψ , as shown in Figure 2. Second, the *Despun* reference frame $D(\hat{\mathbf{d}}_1, \hat{\mathbf{d}}_2, \hat{\mathbf{d}}_3)$ is defined. One of the most commonly used approaches for modeling heliogyros is to average force and moments over two rotations, thereby assuming that the spacecraft is rotating uniformly around its spinning axis $\hat{\mathbf{b}}_3$ [11]. When using this assumption it is useful to define the *Despun* reference frame, visualized in Figure 3a, with $\hat{\mathbf{d}}_1$ along

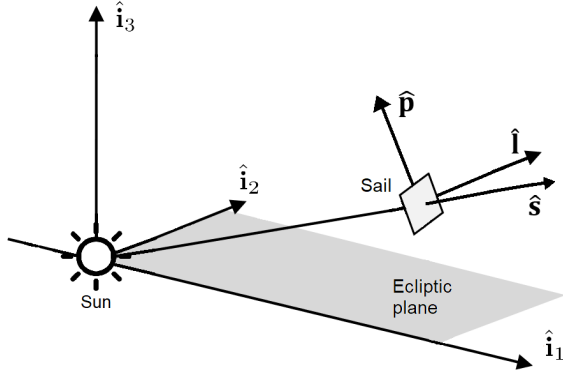


Fig. 1: Relation between the *Solar* and *Inertial* reference frames, adapted from [10].

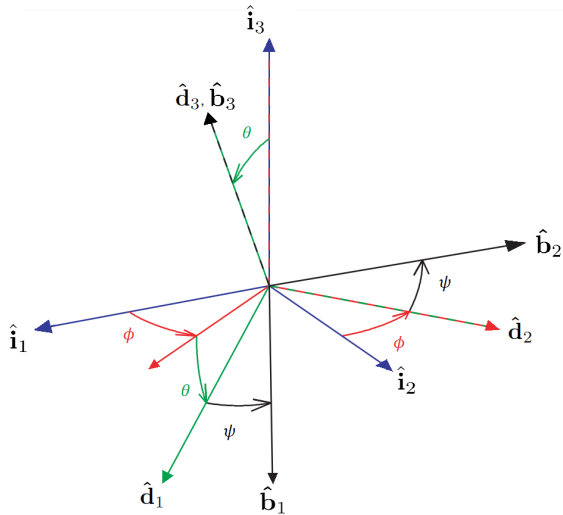


Fig. 2: Relation between the *Body*, *Despun* and *Inertial* reference frames, adapted from [30].

blade 1 at the start of a rotation, $\hat{\mathbf{d}}_3$ aligned with the heliogyro spin-axis, and $\hat{\mathbf{d}}_2$ completing the right-handed frame ($\hat{\mathbf{d}}_2 = \hat{\mathbf{d}}_3 \times \hat{\mathbf{d}}_1$). The *Despun* reference frame is one of the intermediate frames in the reference frame transformation from $I(\hat{\mathbf{i}}_1, \hat{\mathbf{i}}_2, \hat{\mathbf{i}}_3)$ to $B(\hat{\mathbf{b}}_1, \hat{\mathbf{b}}_2, \hat{\mathbf{b}}_3)$, as it is the result of the second rotation over the Euler angle θ , as shown in Figures 2 and 3a.

Finally, for each blade i , a local *Blade* reference frame $L_i(\hat{\mathbf{x}}_i, \hat{\mathbf{y}}_i, \hat{\mathbf{z}}_i)$ is defined, as shown in Figure 3b, centered at the central point of the i^{th} blade's root, with axes $\hat{\mathbf{x}}_i$, $\hat{\mathbf{y}}_i$ and $\hat{\mathbf{z}}_i$ along the i^{th} blade span, root chord and normal to blade i , respectively. Transformations between various frames are discussed in more detail in appendix A.

With the reference frames defined and before continuing the discussion on the blade pitch profile and force and moment models, it is useful to introduce two angles describing the direction of the SRP acceleration vector produced by the sailcraft. These angles are named the “cone” and “clock” angles (α and δ) and are defined relative to the sunlight direction, as shown in Figure 4. The cone angle α is defined as the angle between the sunlight direction $\hat{\mathbf{s}}$ and the SRP acceleration vector, while the clock angle δ is defined as the angle between the axis $\hat{\mathbf{p}}$, perpendicular to the sunlight direction, and the projection of the SRP acceleration vector on the $\hat{\mathbf{p}} - \hat{\mathbf{I}}$ plane [1].

2.2 Pitch profiles

Forces and moments acting on the heliogyro can be controlled by varying the pitch angle of each blade. Literature proposes three pitch control laws: collective, cyclic and half-p [8, 11, 14, 19, 25], as visualized in Figure 5. Each profile is explained in the following paragraphs including their effect when the spin-axis is aligned with the sunlight direction.

The collective profile pitches all blades at the same constant angle. It is useful to generate a spin-axis moment, for example during blade deployment, while also generating a force along the sunlight direction [19]. The half-p profile pitches the blades sinusoidally over two rotations generating significant torque in the $\hat{\mathbf{d}}_1 - \hat{\mathbf{d}}_2$ plane, which can be useful for slewing (spin-axis precession). In addition to this moment, the half-p profile also generates a force along the sunlight direction [19]. The cyclic profile pitches the blades sinusoidally over one rotation, generating a force along the sunlight direction and laterally, in the $\hat{\mathbf{d}}_1 - \hat{\mathbf{d}}_2$ plane. No moments are generated [19]. The capacity to generate a lateral force when the sail is perpendicular to the sunlight is unique to the heliogyro as fixed-sailcraft can only generate a force along the sunlight direction in such an attitude.

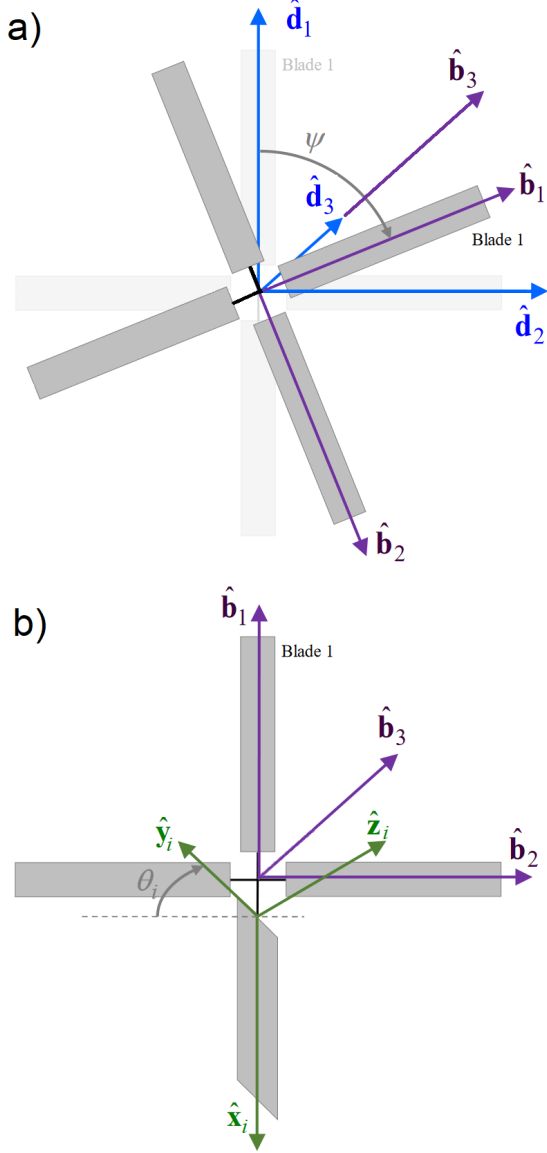


Fig. 3: Visualization of the reference frames *Despun*, *Body*, and *Blade*, adapted from [10]. In a) the relation between the *Despun* and *Body* reference frames is shown. In b) the *Body* and *Blade* reference frames are visualized.

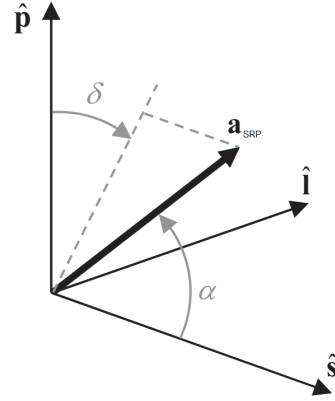


Fig. 4: Visualization of the cone and clock angles of the SRP acceleration vector, \mathbf{a}_{SRP} , adapted from [10].

At heliogyro orientations different from Sun-pointing, each pitch profile may generate forces and moments different from what is discussed above. Furthermore, multiple profiles can be used together to combine multiple effects (though note that forces and moments of different profiles do not super-impose [19]). The pitch angle of any blade i can be directly defined using five control variables [24]:

$$\vartheta_i(\psi_i) = -a_{co} + a_{cy} \sin(\psi_i - \varphi_{cy}) + a_{hp} \sin\left[\frac{1}{2}\left(\psi_i - \varphi_{hp} - \frac{\pi}{2} \text{sign}(a_{hp})\right)\right] \quad [1]$$

with a_{co} , a_{hp} , and a_{cy} the amplitudes of the collective, half-p, and cyclic profiles, φ_{hp} and φ_{cy} the phase angles of the half-p and cyclic profiles, and ψ_i as:

$$\psi_i = \psi + \xi_i; \quad \xi_i = 2\pi \frac{i-1}{N_b} \quad [2]$$

with N_b the number of heliogyro blades.

The phase angles φ_{hp} and φ_{cy} can be interpreted geometrically when the spin-axis is aligned with the sunlight direction: with positive half-p amplitude and zero half-p phase angles, a lateral moment is produced around the $\hat{\mathbf{d}}_1$ direction. A negative amplitude produces a lateral moment around the $-\hat{\mathbf{d}}_1$ direction. The phase angle rotates the direction of the lateral moment around the $\hat{\mathbf{d}}_3$ axis to span the full $\hat{\mathbf{d}}_1 - \hat{\mathbf{d}}_2$ plane. The same interpretation is valid for the lateral force of the cyclic profile through the phase angle φ_{cy} .

2.3 Non-averaged models

To derive the SRP force and moment vectors, the following assumptions are made: the solar radiation pressure is assumed to vary with an inverse square law, all sail membranes are assumed to be flat, and

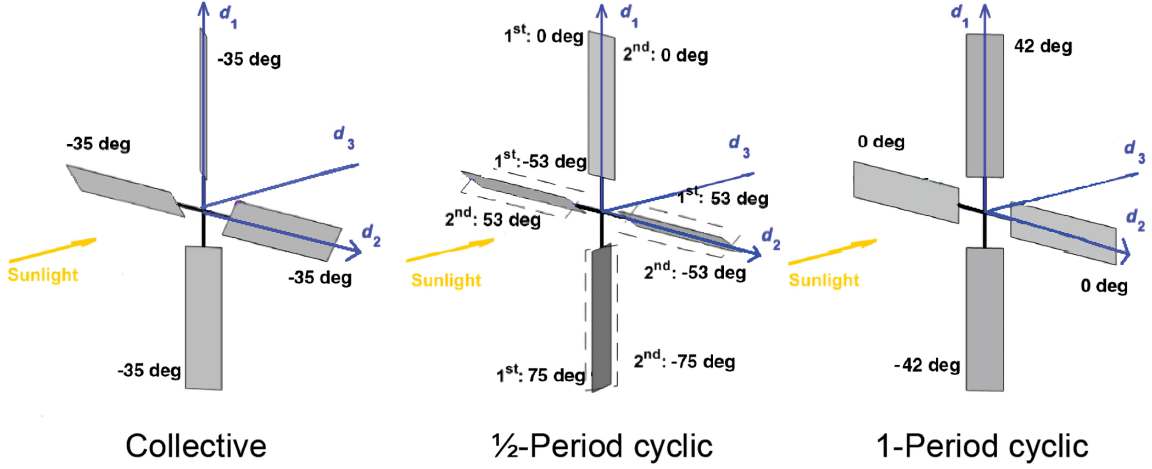


Fig. 5: Heliogyro blade pitch profiles, with dashed lines representing the blade pitch at the second rotation (for half-p), adapted from [10].

all photons are assumed to be reflected specularly. The SRP forces acting on each blade, expressed in the *Blade* reference frame as shown through the superscript L_i , can be defined as [1]:

$$\begin{aligned} \mathbf{F}_i^{[L_i]} &= \frac{2P\eta A}{N_b} \left(\hat{\mathbf{s}}^{[L_i]} \cdot \hat{\mathbf{n}}_i^{[L_i]} \right)^2 \hat{\mathbf{n}}_i^{[L_i]} \\ &= \frac{L_\odot \eta A}{2\pi C N_b \|\mathbf{r}^{[I]}\|^2} \left(\hat{\mathbf{s}}^{[L_i]} \cdot \hat{\mathbf{n}}_i^{[L_i]} \right)^2 \hat{\mathbf{n}}_i^{[L_i]} \end{aligned} \quad [3]$$

where P is the solar radiation pressure, η is the reflectivity coefficient of the sail material, A is the total area of the heliogyro sail, L_\odot is the solar luminosity constant, C is the speed of light, $\mathbf{r}^{[I]}$ is the heliogyro position relative to the Sun expressed in the *Inertial* reference frame with $\|\mathbf{r}^{[I]}\|$ as the sailcraft distance from the Sun, $\hat{\mathbf{s}}^{[L_i]}$ is the vector along the incoming solar radiation, and $\hat{\mathbf{n}}_i^{[L_i]}$ is the normal vector to the blade sail surface (these latter two expressed in the *Blade* reference frame) [10]:

$$\hat{\mathbf{n}}^{[L_i]} = \begin{bmatrix} 0 & 0 & \text{sign}(s_3^{[L_i]}) \end{bmatrix}^T \quad [4]$$

with $s_3^{[L_i]}$ the third component of the $\hat{\mathbf{s}}^{[L_i]}$ vector. The values used for constants such as C and L_\odot are documented in Table 1.

Table 1: List of constants.

Variable	Value	Unit
L_\odot	3.83×10^{26}	W
C	299792458	m/s
μ_\odot	1.327×10^{20}	m^3/s^2
r_E	1	AU
r_M	1.5237	AU

The total instantaneous SRP force acting on the heliogyro, specified in the *Inertial* reference frame, can be computed as:

$$\mathbf{F}^{[I]} = \sum_{i=1}^{N_b} \mathbf{F}_i^{[I]} = \sum_{i=1}^{N_b} [IL_i] \mathbf{F}_i^{[L_i]} \quad [5]$$

with $[IL_i]$ the rotation matrix from the *Blade* reference frame to the *Inertial* reference frame, see appendix A.

To compute the moment generated by the blades, the following assumptions are made: the SRP forces are uniformly distributed across the blade surfaces and the distance between the blades' root chord and the center of mass is neglected. Under these assumptions, the moments acting on the heliogyro around its center of mass (coincident with the origin of the *Body* reference) is computed in the *Body* reference frame (see the superscript $[B]$) as:

$$\begin{aligned} \mathbf{M}^{[B]} &= \sum_{i=1}^{N_b} \frac{R}{2} \hat{\mathbf{x}}_i^{[B]} \times \mathbf{F}_i^{[B]} = \frac{RL_\odot \eta A}{4\pi C N_b \|\mathbf{r}^{[I]}\|^2} \\ &\quad \sum_{i=1}^{N_b} \hat{\mathbf{x}}_i^{[B]} \times \left(\hat{\mathbf{s}}^{[B]} \cdot \hat{\mathbf{n}}_i^{[B]} \right)^2 \hat{\mathbf{n}}_i^{[B]} \end{aligned} \quad [6]$$

with R the blade span.

2.4 Averaged models

For long-term propagations, it is convenient to compute the average forces and moments over two spin rotations, averaging out high-frequency variations due to the periodic pitch profiles [19].

The averaged SRP force and moment can be computed by integrating the forces and moments acting on one of the blades (see Eq. 5 and 6) over two spin rotations of the heliogyro, dividing by 4π and multiplying by the number of blades:

$$\bar{\mathbf{F}}^{[I]} = \frac{L_{\odot}\eta A}{8\pi^2 C \|\mathbf{r}^{[I]}\|^2} \int_0^{4\pi} [IB] \left[\left(\hat{\mathbf{s}}^{[B]} \cdot \hat{\mathbf{n}}_1^{[B]} \right)^2 \hat{\mathbf{n}}_1^{[B]} \right] d\psi \quad [7]$$

$$\bar{\mathbf{M}}^{[D]} = \frac{RL_{\odot}\eta A}{16\pi^2 C \|\mathbf{r}^{[I]}\|^2} \int_0^{4\pi} [DB] \left[\hat{\mathbf{x}}_1^{[B]} \times \left(\hat{\mathbf{s}}^{[B]} \cdot \hat{\mathbf{n}}_1^{[B]} \right)^2 \hat{\mathbf{n}}_1^{[B]} \right] d\psi \quad [8]$$

with the bar hat indicating that the vector is averaged.

In Eq. 7 and 8, blade 1 was used to compute the averaged SRP force and moment, but any other blade would yield the same result. Finally, note that the force and moment vectors are now expressed in the *Inertial* and *Despun* reference frames and the effect of the pitch profile control variables is included in the direction of the normal of the first blade $\hat{\mathbf{n}}_1^{[B]}$.

The definite integrals in Eq. 7 and 8 are evaluated numerically using the trapezoidal rule with 50 segments. This number of segments is selected as a suitable compromise between accuracy of the result and required computational effort, as further explained in appendix C.3.

3. Coupled roto-translational dynamics

The rotational and translational motions of the heliogyro are deeply intertwined, as both the forces and moments affecting the dynamics are dependent on the sailcraft attitude, its position relative to the Sun, and the instantaneous pitch profile control variables. Consequently, in order to produce feasible heliogyro trajectories, the two motions need to be coupled and modeled simultaneously.

In this section, two novel models to characterize the heliogyro coupled roto-translational dynamics are presented, a non-averaged dynamical model and an spin-averaged dynamical model, similarly to the force and moment models from section 2. Firstly, the general basic rotational and translational models adopted are described in subsection 3.1. Later, in subsection 3.2, the non-averaged coupled roto-translational model is presented, followed by the spin-averaged one in subsection 3.3.

3.1 Adopted models

As the focus of this paper is on the *coupling* of the rotational and translational motions and not the fidelity of the resulting trajectories, a simple two-body dynamical model is adopted, similarly to other sailcraft cycler trajectories research [27, 28]. This model only accounts for the gravitational effect of the central body (Sun). Only interplanetary trajectories are analyzed, without any flybys and ignoring the planetary escape and capture phases.

As previously mentioned in subsection 2.1, the sailcraft attitude is described relative to the *Inertial* reference frame through the Euler angles ϕ , θ , and ψ . The heliogyro is assumed to be a rigid body and rotational dynamics are then described through Euler's rotation equations [31]:

$$\mathbf{J}^{[B]} \cdot \dot{\boldsymbol{\omega}}^{[B]} + \boldsymbol{\omega}^{[B]} \times (\mathbf{J}^{[B]} \cdot \boldsymbol{\omega}^{[B]}) = \mathbf{M}^{[B]} \quad [9]$$

where $\mathbf{J}^{[B]}$ is the heliogyro Mass Moment Of Inertia (MMOI) matrix, as later developed in subsection 4.1, $\boldsymbol{\omega}^{[B]}$ the sailcraft angular velocity vector relative to the *Inertial* reference frame, expressed in the *Body* reference frame, and the dot notation representing the first-order derivative relative to time.

The relationship between the Euler angle derivatives and body-fixed angular velocities $\boldsymbol{\omega}^{[B]}$ in the *Body* reference frame is obtained following the methodology presented in [30, 31]:

$$\begin{bmatrix} \dot{\phi} \\ \dot{\theta} \\ \dot{\psi} \end{bmatrix} = \frac{1}{s\theta} \begin{bmatrix} -c\psi & s\psi & 0 \\ s\theta s\psi & s\theta c\psi & 0 \\ c\theta c\psi & -c\theta s\psi & s\theta \end{bmatrix} \boldsymbol{\omega}^{[B]} \quad [10]$$

with s and c representing the sine and cosine functions.

3.2 Non-averaged model

The non-averaged model couples the full rotational motion of the heliogyro with the translational one and is described with a set of 12 first-order differential equations. The state \mathbf{X} is defined as:

$$\mathbf{X} = \left[\mathbf{r}^{[I]}, \dot{\mathbf{r}}^{[I]}, \phi, \theta, \psi, \boldsymbol{\omega}^{[B]} \right]^T \quad [11]$$

For brevity, the superscripts describing the reference frames in which the state variables and MMOI are defined will be omitted from now on.

Two sailcraft performance parameters are defined: the solar loading parameter σ as the ratio between the sailcraft total mass and its area and the sailcraft lightness number β as the ratio between the SRP acceleration and the solar gravitational acceleration [1]. The lightness number can be computed as [1]:

$$\beta = \frac{\eta L_{\odot} A}{2\pi C \mu_{\odot} m} = \frac{\eta L_{\odot}}{2\pi C \mu_{\odot} \sigma} \quad [12]$$

where m is the sailcraft mass and μ_\odot is the Sun's standard gravitational parameter, see Table 1.

Using the aforementioned simplified two-body model, Eq. 5, and Eq. 12, the time derivative of the heliogyro velocity $\dot{\mathbf{r}}$ is obtained as:

$$\dot{\mathbf{r}} = -\frac{\mu_\odot}{\|\mathbf{r}\|^2} \left[1 - \frac{\beta}{N_b} \sum_{i=1}^{N_b} [IL_i] \left(\hat{\mathbf{s}}^{[L_i]} \cdot \hat{\mathbf{n}}_i^{[L_i]} \right)^2 \hat{\mathbf{n}}_i^{[L_i]} \right] \quad [13]$$

The time-derivative of the Euler angles ϕ , θ , and ψ is computed using Eq. 10, while the time derivative of the body-fixed angular velocities $\boldsymbol{\omega}$ is found by rearranging and combining Eq. 6, Eq. 9, and Eq. 12:

$$\dot{\boldsymbol{\omega}} = \frac{\mu_\odot R \sigma \beta A}{2N_b \|\mathbf{r}\|^2} \mathbf{J}^{-1} \left[\sum_{i=1}^{N_b} \hat{\mathbf{x}}_i^{[B]} \times \left(\hat{\mathbf{s}}^{[B]} \cdot \hat{\mathbf{n}}_i^{[B]} \right)^2 \hat{\mathbf{n}}_i^{[B]} - \boldsymbol{\omega} \times (\mathbf{J} \cdot \boldsymbol{\omega}) \right] \quad [14]$$

3.3 Averaged model

Simulating the non-averaged rotational model of the heliogyro is computationally intensive due to the high-frequency variation of the Euler angle ψ , which represents the heliogyro rotation around its spin-axis. Therefore, an averaged model eliminating the ψ state is also developed, to be used for fast propagations and trajectory optimization, exploiting the spin-averaged force and moment models presented in subsection 2.4.

A set of nine first-order differential equations is used to model the averaged dynamics, with the full state $\bar{\mathbf{X}}$ as:

$$\bar{\mathbf{X}} = [\mathbf{r}, \dot{\mathbf{r}}, \phi, \theta, \omega_3]^T \quad [15]$$

where ω_3 is the third component of the body-fixed angular velocity vector $\boldsymbol{\omega}^{[B]}$.

Analogously to the non-averaged model, the translational dynamics are described using Eq. 13 as:

$$\dot{\mathbf{r}} = -\frac{\mu_\odot}{\|\mathbf{r}\|^2} \left[1 - \frac{\beta}{4\pi} \int_0^{4\pi} [IB] \left[\left(\hat{\mathbf{s}}^{[B]} \cdot \hat{\mathbf{n}}_1^{[B]} \right)^2 \hat{\mathbf{n}}_1^{[B]} \right] d\psi \right] \quad [16]$$

The averaged rotational motion can be described by rewriting Eq. 9 relative to the *Despun* reference frame, as done in the ‘‘Generalized Spinning Model’’ [32]:

$$\mathbf{J}^{[D]} \cdot \dot{\boldsymbol{\omega}}^{[D]} + \bar{\boldsymbol{\omega}}^{[D]} \times (\mathbf{J}^{[D]} \cdot \bar{\boldsymbol{\omega}}^{[D]}) = \bar{\mathbf{M}}^{[D]} \quad [17]$$

with $\mathbf{J}^{[D]}$ the MMOI in the *Despun* reference frame, equal to $\mathbf{J}^{[B]}$ due to the sailcraft's axis-symmetry, $\bar{\boldsymbol{\omega}}^{[D]}$ the angular velocity of the *Body* reference frame relative to the *Inertial* reference frame expressed in the *Despun* frame, and $\bar{\boldsymbol{\omega}}^{[D]}$ the angular velocity vector of the *Despun* frame relative to the *Inertial* frame:

$$\bar{\boldsymbol{\omega}}^{[D]} = [\omega_{\hat{\mathbf{a}}_1}, \omega_{\hat{\mathbf{a}}_2}, \omega_3]; \quad \bar{\boldsymbol{\omega}}^{[D]} = [\omega_{\hat{\mathbf{a}}_1}, \omega_{\hat{\mathbf{a}}_2}, 0] \quad [18]$$

When again omitting the superscripts indicating the frame in which the variables are defined, the time derivative of the angular velocity components in the *Despun* frame can be computed by rewriting Eq. 17 as [32]:

$$\dot{\bar{\boldsymbol{\omega}}} = \begin{bmatrix} -\frac{J_3}{J} \omega_3 \omega_{\hat{\mathbf{a}}_2} \\ \frac{J_3}{J} \omega_3 \omega_{\hat{\mathbf{a}}_1} \\ 0 \end{bmatrix} + \mathbf{J}^{-1} \bar{\mathbf{M}}^{[D]} \quad [19]$$

with J_3 indicating the MMOI around the heliogyro spin-axis $\hat{\mathbf{a}}_3$, while J represents the MMOI for the remaining (axis-symmetric) axes.

For a spinning sailcraft it is usually reasonable to assume that the change in spin-axis direction is much slower than the spinning and nutation motion, therefore leading to a slower time-variation of $\bar{\mathbf{M}}^{[D]}$ compared to the aforementioned motions [32]. Using these assumptions, an averaging method can be applied to Eq. 19 to isolate the low-frequency components from the angular velocities [32]:

$$\omega_{\hat{\mathbf{a}}_1} = \frac{-\bar{M}_{\hat{\mathbf{a}}_2}}{J_3 \omega_3}; \quad \omega_{\hat{\mathbf{a}}_2} = \frac{\bar{M}_{\hat{\mathbf{a}}_1}}{J_3 \omega_3}; \quad \dot{\omega}_3 = \frac{\bar{M}_{\hat{\mathbf{a}}_3}}{J_3} \quad [20]$$

where $\bar{M}_{\hat{\mathbf{a}}_1}$, $\bar{M}_{\hat{\mathbf{a}}_2}$, and $\bar{M}_{\hat{\mathbf{a}}_3}$ are the three components of $\bar{\mathbf{M}}^{[D]}$.

Finally, adapting Eq. 10 for the body-fixed angular velocity expressed in the *Despun* reference frame ($\bar{\boldsymbol{\omega}}$, setting ψ to zero), the following first-order averaged rotational equations of motion are found:

$$\begin{bmatrix} \dot{\phi} \\ \dot{\theta} \\ \dot{\omega}_3 \end{bmatrix} = \begin{bmatrix} \frac{\bar{M}_{\hat{\mathbf{a}}_2}}{J_3 \omega_3 \sin \theta} \\ \frac{\bar{M}_{\hat{\mathbf{a}}_1}}{J_3 \omega_3} \\ \frac{\bar{M}_{\hat{\mathbf{a}}_3}}{J_3} \end{bmatrix} \quad [21]$$

4. Problem definition

In this section, the problem to be solved is defined, starting with a description of the heliogyro's design in subsection 4.1. In subsection 4.2, the concepts related to the stop-over cyclers are presented. The optimal control problem is defined in subsection 4.3, while all simulation cases are presented in subsection 4.4.

4.1 Heliogyro design

The total sailcraft mass m is composed of the sail system assembly mass m_{sa} , the payload mass m_u , and the mass of the bus m_{bus} . The sailcraft empty mass m_e equals the sum of the sail system mass m_{sa} and bus mass m_{bus} . The bus mass ratio ϵ and the payload ratio λ are defined as:

$$\epsilon = \frac{m_{bus}}{m_e} = \frac{m_{bus}}{m_{bus} + m_{sa}} \quad [22]$$

$$\lambda = \frac{m_u}{m} \quad [23]$$

The total sailcraft mass can then be rewritten as:

$$\begin{aligned} m &= m_e + m_u = m_{sa} + m_{bus} + m_u; \\ 1 &= \frac{\sigma_{sa}A}{m} + \frac{m_{bus}}{m_{bus} + m_{sa}} \frac{m - m_u}{m} + \frac{m_u}{m} = \\ &= \frac{\sigma_{sa}A}{m} + \epsilon(1 - \lambda) + \lambda; \\ m &= \frac{\sigma_{sa}A}{(1 - \epsilon)(1 - \lambda)} \end{aligned} \quad [24]$$

where σ_{sa} is the sail system loading parameter defined as the ratio between the sail system mass m_{sa} and the sail area A .

The two sailcraft performance parameters introduced in section 3, solar loading σ and sail lightness number β , can be rewritten as:

$$\sigma = \frac{\sigma_{sa}}{(1 - \epsilon)(1 - \lambda)} \quad [25]$$

$$\beta = \frac{\eta L_{\odot} (1 - \epsilon) (1 - \lambda)}{2\pi C \mu_{\odot} \sigma_{sa}} = \beta_0 (1 - \lambda) \quad [26]$$

with β_0 representing the solar-sail lightness number with no payload.

A baseline heliogyro design is presented in Table 2, together with existing designs for heliogyros with mid-term sail performance [9, 14, 18, 19]. The blade aspect ratio \mathcal{AR} (ratio between blade span R and chord c) is conservatively selected to be 500, half of the maximum aspect ratio for which blades are expected to be still operable in space [16]. These parameters result in a blade span and chord of 912 and 1.8 meters, respectively, and a baseline zero-payload lightness number β_0 of 0.153. Note that the lightness number is larger than the expected lightness number

in the mid-term for a fixed-area sailcraft due to the increased performance of the heliogyro design [19], as mentioned earlier in section 1. The baseline case furthermore assumes a payload ratio λ of 0.347, which results in a lightness number β of 0.1. The heliogyro spin rate ω_3 influences the blade structural dynamics and stress experienced at the root of the blade [8]. A baseline value of 0.26 Rotations Per Minute (RPM) is selected based on the spin rate of MacNeal's *Halley's rendezvous heliogyro* design and other historical heliogyro designs [9, 16]. The spin rate is constrained to remain constant during the propagation of the dynamics due to structural reasons, in order to avoid situations where controlling the flexible blades might become unfeasible.

The MMOI of the fully-deployed heliogyro is dominated by the sail blades due to their length [19], allowing the assumption $R^2 \gg c^2$. Neglecting all other minor MMOI contributions apart from the sail blades (payload, bus, sail supporting structure, and so on) and modeling the blades as uniform-mass thin flat plates, the overall MMOI of the sailcraft is approximated as:

$$\begin{aligned} \begin{bmatrix} J_1 \\ J_2 \\ J_3 \end{bmatrix} &\approx m_{sa} \left(\frac{R^2}{3} + \frac{c^2}{12} \right) \begin{bmatrix} \frac{1}{2} \\ \frac{1}{2} \\ 1 \end{bmatrix} \approx \frac{m_{sa} R^2}{3} \begin{bmatrix} \frac{1}{2} \\ \frac{1}{2} \\ 1 \end{bmatrix} \\ &= \frac{A \sigma_{sa} R^2}{3} \begin{bmatrix} \frac{1}{2} \\ \frac{1}{2} \\ 1 \end{bmatrix} = \frac{A^2 \sigma_{sa} \mathcal{AR}}{3 N_b} \begin{bmatrix} \frac{1}{2} \\ \frac{1}{2} \\ 1 \end{bmatrix} \end{aligned} \quad [27]$$

4.2 Stop-over cyclers definition

In this paper, heliogyro trajectories for a stop-over EM cycler are designed. Stop-over indicates that the sailcraft's translational states (Cartesian position and velocity) match the planets' states at departure and arrival.

The trajectories of the two planets are initially approximated as circular and co-planar for simplicity and to allow for cycler periodicity. This approximation is considered valid as the focus of this paper is on the coupling of the sailcraft's translational and rotational motions, so the trajectories are supposed to be only preliminary estimates for mission design. The problem is therefore initially reduced to two-dimensions, with the third components of \mathbf{r} and $\dot{\mathbf{r}}$ constrained to zero, as well as the Euler angle θ limited to $\pm \frac{\pi}{2}$. However, note that the validity of the approach for the 3D case will be demonstrated in subsection 6.3.

The synodic period t_{syn} of Earth and Mars can be computed as:

Table 2: Sailcraft parameters used, based on heliogyro designs from [9, 14, 19]. Derived parameters in italic.

Variable Unit	σ_{sa} g/m ²	A m ²	ω_3 RPM	ϵ -	η -	λ -	N_b -	\overline{AR} -	β_0 -	β -	R m	c m	m kg	m_u kg
HELIOS [19]	<i>13.4</i>	990	1	<i>0.27</i>	<i>0.91</i>	<i>0</i>	6	<i>293.3</i>	<i>0.076</i>	<i>0.076</i>	220	0.75	18.3	<i>0</i>
Blomquist's design [14]	<i>10</i>	1200	0.33	<i>0.28</i>	<i>1</i>	<i>0.056</i>	8	<i>67</i>	<i>0.106</i>	0.1	100	1.5	18	1
Baseline design	7.2	20000	0.26	0.2	0.9	0.347	12	500	0.153	0.1	912	1.8	276	96
Halley's comet Rendezvous [9]	<i>6.14</i>	625000	0.26	0.18	<i>0.92</i>	<i>0</i>	8	<i>937.5</i>	<i>0.189</i>	<i>0.189</i>	7500	8	4698	<i>0</i>

$$t_{syn} = \frac{2\pi}{\sqrt{\frac{\mu_{\odot}}{r_E^3}} - \sqrt{\frac{\mu_{\odot}}{r_M^3}}} \quad [28]$$

with r_E and r_M the distance of Earth and Mars from the Sun, respectively, which are equivalent to the orbits' semi-major axes due to the circular orbit approximation. Using the values shown in Table 1, the synodic period is computed to be approximately 780 Earth days.

The total cyler period t_c will be the sum of all waiting times and transfer times:

$$t_c = t_t^{EM} + t_w^M + t_t^{ME} + t_w^E \quad [29]$$

where t_w^M and t_w^E are the waiting times at Mars and Earth, while t_t^{EM} and t_t^{ME} are the transfer times of the EM and Mars-Earth (ME) leg, respectively.

The waiting times are computed as:

$$\begin{aligned} t_w^M &= t_d^{ME} - t_a^{EM} + k^M t_{syn} \\ t_w^E &= t_d^{EM} - t_a^{ME} + k^E t_{syn} \end{aligned} \quad [30]$$

where t_a^{EM} , t_d^{EM} , t_a^{ME} and t_d^{ME} are the arrival and departing epochs of the EM and ME cyler legs and k^M and k^E are the smallest non-negative integers that make the waiting times positive. The transfer times of the two cyler legs t_t^{EM} and t_t^{ME} are computed as:

$$\begin{aligned} t_t^{EM} &= t_a^{EM} - t_d^{EM} \\ t_t^{ME} &= t_a^{ME} - t_d^{ME} \end{aligned} \quad [31]$$

The total period of the cyler will be a multiple of the Earth-Mars synodic period, and can be computed by summing all waiting and transfer times. The cyler problem is parameterized by the departure and transfer times of each leg. January 1st, 2024 at midnight (Barycentric Dynamical Time) is used as a reference time.

4.3 Optimal control problem definition

The heliogyro cyler problem can be described though an optimal control problem consisting of two legs, the EM leg and the ME leg. In order to limit the required computational effort, the problem dynamics for both legs are modeled through the averaged heliogyro dynamics described in subsection 3.3, and the problem is reduced to co-planar ($\hat{\mathbf{i}}_1 - \hat{\mathbf{i}}_2$ plane). Note that the assumption of averaged dynamics will be tested against the non-averaged dynamics in subsection 6.3.

The optimal control problem objective O is to minimize the sum of the transfer times t_t^{EM} and t_t^{ME} of the heliogyro cyler (which maximizes the waiting times at the two planets and the number of round-trips between them within a set time-frame):

$$\text{Minimize: } O = t_t^{EM} + t_t^{ME} \quad [32]$$

The reduced state vector $\bar{\mathbf{X}}_r(t)$ is composed of the four co-planar components ($\hat{\mathbf{i}}_1 - \hat{\mathbf{i}}_2$ plane) of the Cartesian position and velocities, the first Euler angle ϕ describing the heliogyro orientation on the $\hat{\mathbf{i}}_1 - \hat{\mathbf{i}}_2$ plane, and the spin rate ω_3 . The non-coplanar Cartesian position and velocities components are set to zero, while the second Euler angle is set to -0.5π . All states are unbounded, except the spin rate which is constrained to the baseline value of 0.26. The reduced control vector $\mathbf{u}_r(t)$ consists of the time-varying pitch profile angles a_{co} , a_{cy} , a_{hp} described in subsection 2.2, which are bounded between $\pm 0.5\pi$. The phase angles are not included for the co-planar case and are set to a constant value of -0.5π to generate forces only in the $\hat{\mathbf{i}}_1 - \hat{\mathbf{i}}_2$ plane and moments in $\hat{\mathbf{d}}_2$ direction. For both legs, the problem can be fully described at any epoch t through the heliogyro state $\bar{\mathbf{X}}_r(t)$ and control vector $\mathbf{u}(t)$.

For each leg, boundary conditions are set such that the heliogyro position and velocity match the ones of the origin and target planets (at the departure and arrival time, respectively):

Table 3: List of cases simulated. “Dec.” indicates “decreasing”, “inc.” indicates “increasing”.

Case ID	Dynamics	β^{EM}	β^{ME}	λ^{EM}	λ^{ME}	ω_3 [RPM]
1a	Averaged	0.1	0.1	0.347	0.347	0.26
1b	Non-averaged	0.1	-	0.347	-	0.26
1c	Averaged, 3D	0.1	-	0.347	-	0.26
2	Averaged	Dec. from β_0	Dec. from β_0	Inc. from 0	Inc. from 0	0.26
3	Averaged	Dec. from 0.1	β_0	Inc. from 0.347	0	0.26
4	Averaged	0.1	0.1	0.347	0.347	Inc. from 0.1

$$\begin{aligned}
 \mathbf{b}_d^{EM} &= \mathbf{X}_{pv}^{EM}(t_d^{EM}) - \Upsilon_{pv}^E(t_d^{EM}) = \mathbf{0} \\
 \mathbf{b}_a^{EM} &= \mathbf{X}_{pv}^{EM}(t_a^{EM}) - \Upsilon_{pv}^M(t_a^{EM}) = \mathbf{0} \\
 \mathbf{b}_d^{ME} &= \mathbf{X}_{pv}^{ME}(t_d^{ME}) - \Upsilon_{pv}^M(t_d^{ME}) = \mathbf{0} \\
 \mathbf{b}_a^{ME} &= \mathbf{X}_{pv}^{ME}(t_d^{ME}) - \Upsilon_{pv}^E(t_d^{ME}) = \mathbf{0}
 \end{aligned} \tag{33}$$

with \mathbf{b} representing the boundary condition constraint vector, Υ_{pv}^E and Υ_{pv}^M indicating Earth and Mars’ translational state respectively, and \mathbf{X}_{pv} as the sailcraft translational state.

4.4 Study cases

The cases analyzed in this paper are presented in Table 3 and further elaborated in section 6.

Case 1a is the baseline case, using the baseline heliogyro design described in subsection 4.1 and the averaged dynamical model from subsection 3.3 reduced to a 2D co-planar case, as explained earlier in subsection 4.2.

Cases 1b and 1c all use the same baseline heliogyro, but vary the dynamical model. Case 1b simulates part of the EM leg using the non-averaged dynamical model from subsection 3.2, in order to validate the assumptions of the averaged model and to analyze the heliogyro rotational dynamics. For this case the non-averaged state from Eq. 11 and the full pitch profiles control variables (a_{co} , a_{hp} , a_{cy} , φ_{hp} , and φ_{cy}) are used. Case 1c simulates the full EM leg using the averaged dynamical model but in 3D, in order to show the validity of the model also for out-of-plane motion of the sailcraft. For the latter case, a non-circular non-co-planar Keplerian approximation of the ephemerides of Earth and Mars is used [33]. The full averaged state from Eq. 15 is used (adding the non-co-planar position component, velocity component, and second Euler angle θ compared to the state from the baseline case 1a), as well as the full pitch profile control vector.

Cases 2, 3 and 4 all use the same state, controls and dynamics as the baseline case 1a, but vary a design

parameter of the heliogyro. Case 2 analyzes the sensitivity of the baseline trajectory to the payload ratio (equal for both the EM and ME leg) and therefore the sailcraft performance through the lightness number β . The payload ratio is varied from a value of zero to the maximum value for which the cyclor can still be performed within the same amount of EM synodic periods as the baseline case, using uniform steps in the lightness number steps of 0.005.

In case of a resupply mission to a Martian outpost, it might be convenient to maximize the payload ratio for the EM leg, and return to Earth with no payload. This is studied in Case 3, setting the ME payload ratio to zero and varying the EM payload ratio from the baseline value to the maximum value for which the cyclor can still be performed within the same amount of EM synodic periods as the baseline case. Uniform steps in the EM payload ratio of 0.025 are used.

Finally, Case 4 analyzes the sensitivity of the baseline trajectory to the spin rate ω_3 . The spin rate is varied from 0.1 RPM to the maximum value for which the cyclor can still be performed within the same amount of EM synodic periods as the baseline. Uniform steps in the spin rate of 0.01 RPM are used. Note that these simulations also potentially represent the sensitivity of the trajectory to design parameters that affect the heliogyro’s MMOI and generated moments such as N_b , A and \mathcal{R} .

5. Trajectory design

In this section, the methodology used to design the heliogyro cyclor trajectories is presented. A multiple shooting algorithm is adopted to transcribe the continuous problem into a Non-Linear Programming (NLP) problem, as described in subsection 5.1. It is preferable to initialize such algorithms with an initial trajectory close to the expected solution to aid convergence, therefore the generation of initial guesses is a critical step. The process of generating such guesses is presented in subsection 5.2.

5.1 Multiple shooting method

A multiple shooting algorithm is selected to transcribe the continuous problem into an NLP problem, as it is relatively simple to implement, has high parallelization potential, and has been used for similar solar-sailing and astrodynamics research works [34, 35]. Multiple shooting improves several issues of single-shooting algorithms, including more robustness for highly non-linear problems, with the downside of increasing the dimensionality of the problem [36, 37, 38].

The trajectory of each leg is split into several segments ($N_s + 1$ grid points, with N_s the number of segments) and the state and control vectors at each grid-point are included in the design variables to optimize. Each segment initial state is propagated numerically until the end of the segment and the differences (named defects) between the final propagated states and the initial states of the next segment are enforced to be zero using equality constraints, as shown in Figure 6.

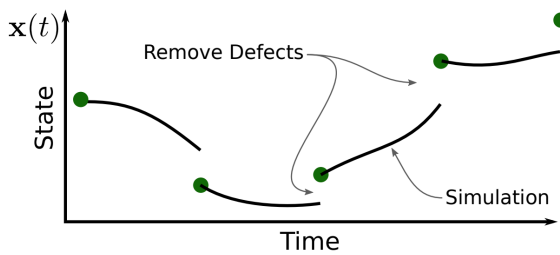


Fig. 6: Visualization of the multiple shooting transcription [38].

The initial and final propagation times are included in the design variables, such that the complete design variables vector χ describing both the EM and ME legs is:

$$\chi = [\bar{\mathbf{X}}_{r;1}^{EM}, \bar{\mathbf{X}}_{r;2}^{EM} \dots \bar{\mathbf{X}}_{r;N_s+1}^{EM}, \mathbf{U}_r^{EM}, t_d^{EM}, t_t^{EM}, \bar{\mathbf{X}}_{r;1}^{ME}, \bar{\mathbf{X}}_{r;2}^{ME} \dots \bar{\mathbf{X}}_{r;N_s+1}^{ME}, \mathbf{U}_r^{ME}, t_d^{ME}, t_t^{ME}] \quad [34]$$

with $\bar{\mathbf{X}}_{r;j}^k$ the heliogyro state (reduced averaged model, see subsection 4.3) of the j^{th} grid-point of leg k , and the vector \mathbf{U}_r^k as:

$$\mathbf{U}_r^k = [\mathbf{u}_{r;1}^k, \mathbf{u}_{r;2}^k \dots \mathbf{u}_{r;N_s+1}^k] \quad [35]$$

with $\mathbf{u}_{r;j}^k$ the reduced control vector (see subsection 4.3) of the j^{th} grid-point of leg k . The control vector is linearly interpolated as a function of time between the $N_s + 1$ grid-points. The subscript notation to indicate the reduced state and controls is omitted from now for simplicity.

For cases 1b and 1c the definition of the design vector is extended from the one in Eq. 34 with the complete control vectors and state vectors as described in subsection 4.4.

The number of segments for the optimization is set to 48, in order to match the number of available parallelization threads in the workstation used, maximizing computational efficiency. Analyses have been performed that highlight that a smaller number of segments often results in divergence problems, while a larger number does not significantly improve the quality of the solution (in terms of objective) and also leads to an increase in number of iterations to reach convergence, sometimes diverging.

The initial conditions of all segments are numerically propagated to the final time using a RK4 integrator, a constant time-step numerical integration method. Variable time-step methods were not considered as they can lead to discontinuities when propagating the State Transition Matrix (STM) [39], therefore leaving constant time-step methods as the most suitable choice. RK4 is chosen because of its popularity and high efficiency compared to other constant time-step numerical integration methods, in terms of numerical accuracy relative to the number of function evaluations [36, 40]. A time-step of 10^{-3} synodic periods (i.e. approximately one Earth day) is adopted as it was found to be a good compromise between numerical accuracy and computational effort, as further explained in appendix C.2.

Due to the multiple shooting transcription, the majority of the equality constraints are the defects enforcing a continuous trajectory between segments. For a segment j of leg k , the defect constraint relative to the following segment is defined as:

$$\mathbf{c}_j^k = \tilde{\bar{\mathbf{X}}}_{j+1}^k - \bar{\mathbf{X}}_{j+1}^k \quad [36]$$

where $\tilde{\bar{\mathbf{X}}}_{j+1}^k$ is the state at the beginning of segment $j+1$, propagated from the initial condition of segment j .

The boundary conditions from subsection 4.3 are applied at the initial and final segment as equality constrains. Two inequality constraints are set, enforcing that the waiting times at Earth and Mars are longer than 0.01 EM synodic periods (approximately a week). Additional constraints are added to enforce moments $\bar{M}_{\mathbf{a}_1}$ and $\bar{M}_{\mathbf{a}_3}$ to be equal to zero to keep the spin-rate ω_3 constant and restrict the sailcraft motion to be co-planar with the planets (except for cases 1b and 1c for which the motion is not constrained to be co-planar). Other constraints are added to ease the convergence of the optimizer. Firstly, inequality constraints limiting the time derivative of the pitch profiles angles within two degrees per day (absolute

value) are introduced, as large angular rates are not expected for long interplanetary trajectories. In addition to that, additional constraints (one for each control variable) are included to avoid sudden jumps of the control vector, by enforcing a maximum value of the norm of all “concavities” for the control at each grid-point j :

$$\sqrt{\sum_{j=1}^{j=N_s-1} (\mathbf{u}_{j+1}^k + \mathbf{u}_{j-1}^k - 2\mathbf{u}_j^k)^2} \leq \kappa \quad [37]$$

with κ as an arbitrary vector of constants tuned to achieve the desired results (0.01 radians).

The problem is scaled to avoid numerical errors, as the quantities involved have significantly different orders of magnitude. Positions are normalized in astronomical units, times are scaled by one EM synodic period, and angular velocities are expressed in RPM.

The heliogyro dynamics are implemented in Python. WORHP (version 1.14) is used to solve the discretized optimal control problem as it is particularly suited to solve highly dimensional non-linear problems, often used in space applications [41], it is robust, and has a Python interface through the Pygmo library [42]. As WORHP is a derivative-based solver, the derivatives of the constraints and objective relative to the design vector χ need to be computed.

During each propagation, the STM Φ and sensitivity matrix \mathbf{S} are computed through the numerical integration of the variational equations [40]:

$$\begin{aligned} \dot{\Phi}(t, t_j) &= \frac{\partial \dot{\bar{\mathbf{X}}}(t, \bar{\mathbf{X}}(t), \mathbf{u}(t))}{\partial \bar{\mathbf{X}}(t)} \Phi(t, t_j) \\ \dot{\mathbf{S}}(t, t_j) &= \frac{\partial \dot{\bar{\mathbf{X}}}(t, \bar{\mathbf{X}}(t), \mathbf{u}(t))}{\partial \bar{\mathbf{X}}(t)} \mathbf{S}(t, t_j) \\ &\quad + \frac{\partial \dot{\bar{\mathbf{X}}}(t, \bar{\mathbf{X}}(t), \mathbf{u}(t))}{\partial \mathbf{u}(t)} \end{aligned} \quad [38]$$

The derivatives needed to compute the STM, sensitivity matrices, and Jacobian matrices are computed numerically through central finite difference. The selection of suitable steps to compute the numerical derivatives is further discussed in appendix C.4.

Omitting the leg notation for simplicity, the derivatives of the defect constraints relative to the initial state of segment j , the initial state of segment $j + 1$, and the vector \mathbf{U} containing the control inputs for all segments are:

$$\begin{aligned} \frac{\partial \mathbf{c}_j}{\partial \bar{\mathbf{X}}_j} &= \frac{\partial \tilde{\bar{\mathbf{X}}}_{j+1}}{\partial \bar{\mathbf{X}}_j} = \Phi(t_{j+1}, t_j) \\ \frac{\partial \mathbf{c}_j}{\partial \bar{\mathbf{X}}_{j+1}} &= -\mathbf{I} \\ \frac{\partial \mathbf{c}_j}{\partial \bar{\mathbf{U}}} &= \frac{\partial \tilde{\bar{\mathbf{X}}}_{j+1}}{\partial \bar{\mathbf{U}}} = \mathbf{S}(t_{j+1}, t_j) \\ \frac{\partial \mathbf{c}_j}{\partial t_d} &= \mathbf{0} \\ \frac{\partial \mathbf{c}_j}{\partial t_t} &= \frac{\partial \tilde{\bar{\mathbf{X}}}_{j+1}}{\partial t_{j+1}} \frac{\partial t_{j+1}}{\partial t_t} \\ &= \left(\dot{\bar{\mathbf{X}}}(t_{j+1}, \bar{\mathbf{X}}_{j+1}, \mathbf{U}) - \mathbf{S} \right) \frac{1}{N_s} \end{aligned} \quad [39]$$

where \mathbf{I} is the identity matrix. For the last partial derivative, the first term in the parentheses represents the influence of the segment duration on the problem dynamics, while the second term represent the influence of “time-stretching” the control inputs due to the increased segment time on the propagated final state of the segment.

The non-zero derivatives of the boundary conditions are computed as follows:

$$\begin{aligned} \frac{\partial \mathbf{b}_d}{\partial \bar{\mathbf{X}}_{pv;1}} &= \frac{\partial \bar{\mathbf{X}}_{pv;1}}{\partial \bar{\mathbf{X}}_{pv;1}} = \mathbf{I} \\ \frac{\partial \mathbf{b}_d}{\partial t_d} &= -\dot{\Upsilon}_{pv} \\ \frac{\partial \mathbf{b}_a}{\partial \bar{\mathbf{X}}_{pv;N_s+1}} &= \frac{\partial \bar{\mathbf{X}}_{pv;N_s+1}}{\partial \bar{\mathbf{X}}_{pv;N_s+1}} = \mathbf{I} \\ \frac{\partial \mathbf{b}_a}{\partial t_d} &= -\dot{\Upsilon}_{pv} \\ \frac{\partial \mathbf{b}_a}{\partial t_t} &= \frac{\partial \bar{\mathbf{X}}_{pv;N_s+1}}{\partial \bar{\mathbf{X}}_{pv;N_s+1}} - \dot{\Upsilon}_{pv} = \mathbf{I} - \dot{\Upsilon}_{pv} \end{aligned} \quad [40]$$

with the planetary target state selected depending on each phase. All derivatives of the objective are zero except the ones relative to the transfer times:

$$\frac{\partial O}{\partial t_t^k} = 1 \quad [41]$$

The overall fitness vector \mathbf{f} containing the objective and the constraints is constructed as follows:

$$\mathbf{f} = \left[O, \mathbf{b}_d^{EM}, \mathbf{c}_1^{EM}, \dots, \mathbf{c}_{N_s}^{EM}, \mathbf{b}_a^{EM}, \mathbf{b}_d^{ME}, \mathbf{c}_1^{ME}, \dots, \mathbf{c}_{N_s}^{ME}, \mathbf{b}_a^{ME}, \mathbf{v}^{EM}, \mathbf{v}^{ME} \right]^T \quad [42]$$

with \mathbf{v} as the vector containing all implemented constraints except for the defects and boundary conditions.

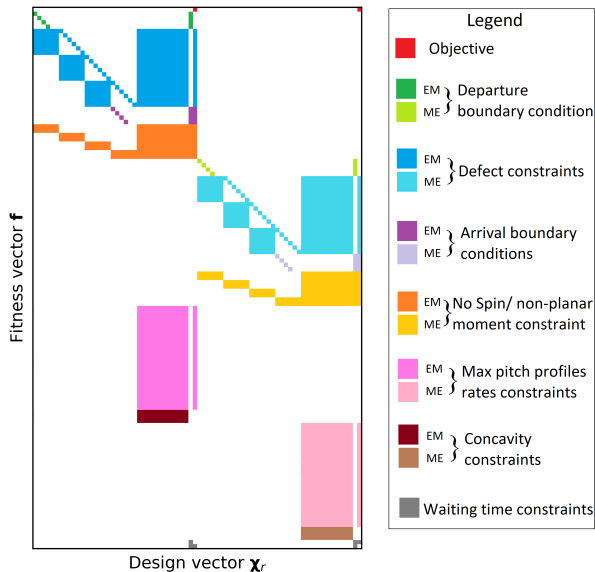


Fig. 7: Visualization of Jacobian matrix.

The Jacobian matrix $\frac{\partial \mathbf{f}}{\partial \mathbf{x}}$ is used by WORHP to progress each iteration. The matrix is constructed combining the aforementioned derivatives as shown in Figure 7, for cycler trajectories with three segments for each phase. All zero-terms are white, while all colored blocks correspond to the non-zero derivatives. Note that the order of the fitness vector \mathbf{f} in the figure may differ from the one in Eq. 42 due to specific the requirements of WORHP on the order of the constraints (it requires first all the equalities constraints followed by the inequality constraints), while the order of the design vector \mathbf{x} is as presented in Eq. 34.

For the objective (in red), only the transfer time derivative appears. The boundary conditions (in green and purple) are only dependent on the departure or the arrival state and the departure and arrival time. The part of the Jacobian related to the defects (in blue) contains the STMs (the large square diagonal boxes), the initial state of the following segments (the small diagonal blocks), the sensitivity matrices (the large vertical rectangles), as well as the time derivative relative to the transfer time (the rightmost blue columns). The remaining constraints (in pink, orange and brown) may depend on the state, the control inputs, and the departure and transfer times.

The Jacobian matrix $\frac{\partial \mathbf{f}}{\partial \mathbf{x}}$ is constructed and passed to WORHP at each iteration. As shown in the figure, the matrix is fairly sparse (even more so when additional segments are included). Its sparsity is exploited to lower the computational effort, by computing only the numerical derivative for the non-zero terms. On

the other hand, the Hessian matrix is approximated numerically within WORHP [41].

A tolerance of 10^{-4} is set on the scaled constraints to achieve easier convergence (see appendix C.1 for the rationale behind the selection of the value). Finally, a convergence criterion is set such that the optimizer stops when reaching a scaled optimality of 10^{-3} (see the *TolOpti* parameter from the WORHP user manual [43]). All other WORHP settings are set at the default value.

5.2 Initial guess generation

The generation of initial guesses is critical for the convergence of the NLP solver when dealing with a highly dimensional non-linear problem. The multi-step process visualized in Figure 8 is adopted, starting with a simple problem and increasing its complexity at each stage, such that for each step the solution of the previous problem can be used as initial guess. This approach is adopted to ease the convergence of the algorithm at each step.

The first step is to find suitable approximate departure dates for both the EM and ME leg, modeling the continuous low-thrust trajectory analytically using logarithmic spirals [1]. The transfer time can be approximated using [1]:

$$\begin{aligned}
 t_t^{EM} &= \frac{1}{3} \left(r_M^{3/2} - r_E^{3/2} \right) \sqrt{\frac{1 - \beta \cos^3 \alpha}{\beta^2 \mu_\odot \cos^4 \alpha \sin^2 \alpha}} \\
 t_t^{ME} &= \frac{1}{3} \left(r_E^{3/2} - r_M^{3/2} \right) \sqrt{\frac{1 - \beta \cos^3 \alpha}{\beta^2 \mu_\odot \cos^4 \alpha \sin^2 \alpha}}
 \end{aligned} \tag{43}$$

with the lightness number β set to 0.1 from the baseline heliogyro design described in subsection 4.1. The cone angle α is optimal at $\pm 35.26^\circ$ [1], positive if increasing the orbital semi-major axis and negative if decreasing it. After computing the transfer times, a grid-search is performed varying the departure times for both legs throughout a full EM synodic period to find their values that minimize the miss distance at arrival (from the target planet). The departure time of the ME trajectory is enforced to be after the arrival time of the EM trajectory. The logarithmic spiral trajectories (sailcraft position and velocity) and the departure and transfer times are used as an initial guess for the next step.

The second stage for initial guess generation numerically optimizes the trajectories of a fixed-area solar sail for both the EM and ME legs. The trajectories are combined into the cycler problem, with the waiting time constraints and the objective of minimizing the sum of transfer times, as explained in subsection 4.3. The dynamics used are those in Eq. 13

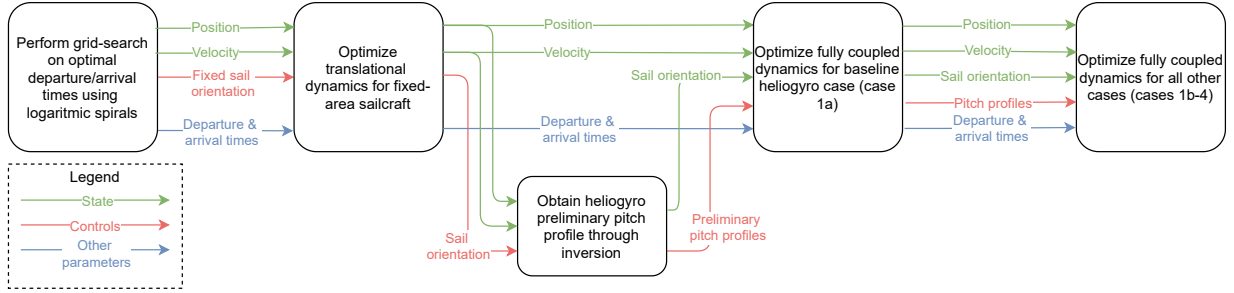


Fig. 8: Visualization of the process to generate initial guesses.

(therefore omitting the sailcraft rotational dynamics), with the SRP forces from the ideal model in Eq. 3 (setting N_b to 1). WORHP and the multiple shooting transcription are used to solve the optimal control problem, as explained in subsection 5.1, with the sailcraft state and design vector of each leg k as:

$$\begin{aligned} \mathbf{X}_{sc}^k &= [\mathbf{r}, \dot{\mathbf{r}}] \\ \boldsymbol{\chi}_{sc}^k &= [\mathbf{X}_{sc;1}^k \cdots \mathbf{X}_{sc;N_s+1}^k, \\ &\quad \phi_1 \cdots \phi_{N_s+1}, t_d^{ME}, t_t^{ME}] \end{aligned} \quad [44]$$

where the subscript sc indicates that it is the state/design vector for a fixed-area solar sail, other numerical subscripts indicating the segment number, and the Euler angle ϕ used as the only control variable (the problem is reduced to 2D as explained in subsection 4.2). The optimal control solution $\boldsymbol{\chi}_{sc}^k$ fully describes the optimal EM and ME trajectories for a fixed-area solar sail.

The fixed-area solar-sail trajectory is used as an input for the baseline case described in subsection 4.2 (case 1a). The Euler angle ϕ is converted from a control to a state, because the rotational dynamics are simulated in the baseline case. For each grid-point, the control vector with pitch profiles $\mathbf{u}_{r;j}^k$ is initialized by solving a reduced inverse problem [24], computing the amplitude angles (a_{co} , a_{hp} , and a_{cy}) that generate the required moment and sailcraft acceleration (Eq. 7 and 8) to match the initial guess. Firstly, the phase angles (φ_{hp} and φ_{cy}) are set to $-\frac{\pi}{2}$ to generate forces and moments in the required direction. The required time derivative $\dot{\phi}$ is computed numerically (central finite difference) from the initial guess and inserted into Eq. 8 to compute the required moment. The required acceleration is computed from the ideal model in Eq. 3 based on the ideal trajectory (\mathbf{r} and ϕ). Finally, the Nelder-Mead algorithm is used to numerically find the pitch profiles amplitude angles that minimize the acceleration and moments errors, with a convergence criterion of 10^{-7} m/s^2 and 10^{-7} Nm , respectively. This algorithm is selected as it is

simple, available through the SciPy library [44], does not require derivatives (which would have to be numerical for the averaged force and moment models) and works for multi-dimensional problems. In cases of failed convergence for specific time-steps, the converged solution of the nearest time-step is used.

The solution of case 1a is then used as an initial guess for all other cases. For the sensitivity analyses in cases 2 to 4 a continuation method is used such that the solution of the problem with the closest varying input parameter is used as an initial guess.

6. Results & discussion

In this section, the results of the cases defined in subsection 4.4 are presented, following the order described in Figure 8 and subsection 5.2. Cases are named following the nomenclature given in Table 3.

Firstly, the results of the systematic search to analyze the solar-sail cyler feasibility and optimal departure time are presented in subsection 6.1. The results of that analysis are used to generate a fixed-area solar sail cyler solution and the baseline heliogyro cyler solution (case 1a). These results are shown and compared in subsection 6.2. In subsection 6.3, an in-depth analysis of the heliogyro coupled-rotational motion is performed and presented, analyzing the non-averaged motion results (case 1b) and the non-planar averaged case (case 1c). Finally, in subsection 6.4, sensitivity analyses of the baseline heliogyro cyler are performed for varying lightness numbers, payload ratios of the EM leg, and spin-rates.

6.1 Cyler departure time systematic search

As explained in subsection 5.2, an analytical model is used to generate very preliminary interplanetary transfer trajectories. The results of the systematic search are shown in Figure 9, where the departure time of each leg is varied throughout two synodic periods (horizontal axis) and the miss distance at arrival is computed and displayed on the vertical axis.

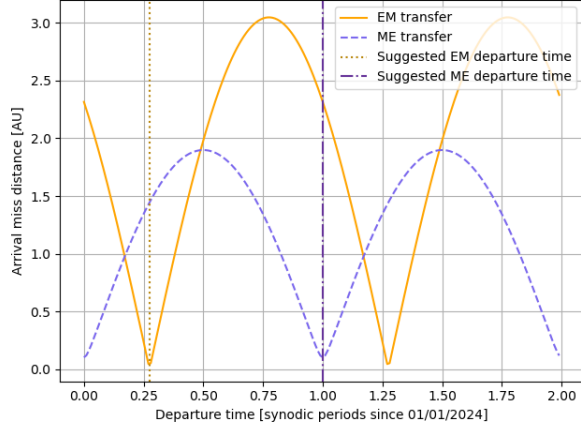


Fig. 9: Arrival miss distance as a function of departure time for both cyler legs, computed to generate the initial guess.

To generate the results, the initial state of the sailcraft from each departure time is forward propagated for 0.55 synodic periods, the transfer times of both the EM and ME legs found from Eq. 43. The miss distances at arrival are computed as the position differences between the sailcraft and the target planet at the arrival times.

The figure shows that for both legs the miss distance is periodic (one synodic period) and has minima around zero, as expected. From the figure, the first optimal opportunity to initiate the EM leg is approximately at $t_d^{EM} = 0.275$, while the optimal departure opportunity for the ME leg is at $t_d^{EM} = 1$. The difference between the departure times of the ME and EM legs is significantly larger than the transfer time of 0.55 synodic periods, therefore allowing the sailcraft to transfer between the two planets in time and indicating that a cyler with a period of two synodic periods is feasible. Note that the transfer times for later results are expected to be longer than this preliminary estimation as the planets' velocities are not matched using the analytical model approximation.

6.2 Heliogyro/fixed-area solar sail comparison

The cyler trajectories for the baseline heliogyro cyler (case 1a) and fixed-area solar sail cyler are generated solving the optimal control problems presented in subsection 5.1 and subsection 5.2, respectively.

The optimal fixed-area solar sail cyler solution is shown in Figure 10. In Figure 10a the two co-planar trajectories for the two legs are shown in the *Inertial* reference frame with arrows showing the magnitude and direction of the SRP acceleration. In Figure 10b

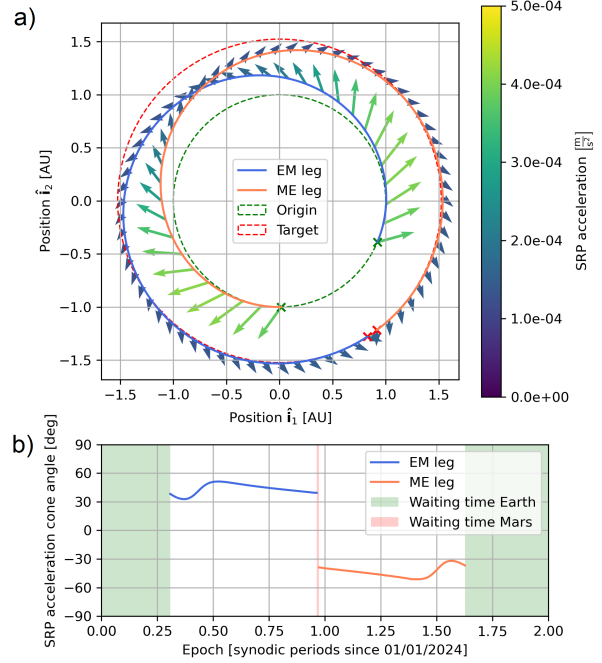


Fig. 10: Fixed-area solar-sail cyler solution. In a) the two legs are presented with arrows to show the force magnitude and direction, while in b) the cone angle of the SRP acceleration vector as a function of time is visualized.

the cone angle of the SRP acceleration vector is visualized as a function of time, while the clock angle is not shown as the problem is co-planar (therefore the clock angle is constant).

From the magnitude and color of the arrows, it can be seen that the SRP force magnitude is larger when the sailcraft is closer to the Sun, as expected. It can also be observed that the cone angle of the SRP acceleration vector varies around the analytical model optimum of ± 35.26 degrees and is axis-symmetric (around the horizontal axis) for the two legs. As expected, the cone angle is positive for the EM leg as the sailcraft needs to increase its velocity, and negative for the ME leg to slow down. Note that for fixed-area solar sails (using an ideal SRP force model) the cone angle of the SRP acceleration vector also describes the sail attitude, as the force is always aligned with the sail normal [1]. This is not necessarily the case for the heliogyro as will be demonstrated later.

Using the fixed-area sailcraft trajectory as an initial guess, the baseline heliogyro cyler solution is computed (case 1a). The transfer and waiting times of the heliogyro and fixed-area solar sail solutions are shown in the first two rows of Table 4, while the re-

sulting heliogyro trajectories for the two legs, as well as the required controls and cone angles of the SRP acceleration vector are shown in Figure 11.

As shown in the table, the total transfer time for the heliogyro is only marginally longer than the fixed-area sailcraft (less than 5%). This is a remarkable finding as the heliogyro is controlling both the sailcraft rotational and translational motion, meaning that no additional ACS is needed. This is not the case for the fixed-area sailcraft as the rotational dynamics are not taken into account and an additional suitably-sized ACS would be needed, degrading the sailcraft performance. In addition to this, as already mentioned in section 1 and subsection 4.1, fixed-area sailcraft in general would have a smaller zero-payload lightness number compared to heliogyros due to the heavier sail supporting structure, while in this research work they are taken as equivalent.

From Table 4 it is also clear that the waiting time at Mars is equal to 0.01 synodic periods (the minimum allowable value) for both cyclers. From these results, it can be concluded that the waiting time constraint at Mars is active and limiting for both cycler solutions.

The heliogyro cycler trajectories and the SRP acceleration magnitude and direction are displayed in Figure 11a. It can be seen that the heliogyro cycler legs appear to be similar to the fixed-area solar sail legs. The shorter waiting time at Earth of the heliogyro cycler is also visible when comparing with the fixed-area solar-sail trajectory in Figure 10, as also already highlighted previously in Table 4.

Figure 11b displays the cone angle of the SRP acceleration vector (this time *not* equivalent to the sailcraft orientation) as a function of time. The plot shows that the cone angle once again varies around the analytical optimal value of ± 35.26 degrees and is approximately axis-symmetric around the horizontal axis for the two legs, very similar to the fixed-area sailcraft shown in Figure 10b. The direction of the heliogyro's spinning axis is not shown in the figure but it differs up to a maximum of 7 degrees from the acceleration direction.

Finally, Figure 11c shows the controls pitch profiles $\mathbf{u}_r(t)$ as a function of time. A few large and sudden amplitude angle variations are visible and are attributed to the numerical noise of the derivatives used to solve the NLP problem, as previously explained in subsection 5.1. This effect is emphasized by the low sensitivity of the sailcraft state derivatives to the pitch profile angles, as some of the variations of three to five degrees have limited effects on the states derivatives. A relatively constant value (between five and six degrees) of the half-p amplitude (a_{hp}) is vis-

ible, while the other two pitch profile amplitudes oscillate around zero. The positive half-p amplitude is needed to generate moments around the $\hat{\mathbf{d}}_2$ axis that produce the required rotation rate of the sailcraft ($\dot{\phi}$, see Eq. 21) to keep the heliogyro's spinning axis direction close to the the sunlight direction as the sailcraft revolves around the Sun. On the other hand, the other pitch profile variations are needed to cancel out any moment around $\hat{\mathbf{d}}_3$ (to keep ω_3 constant) and provide the other required force and moment corrections to obtain the optimal trajectory.

Overall, comparing the fixed-area sailcraft cycler with the heliogyro cycler through Table 4, Figure 10, and Figure 11, it can be concluded that the cycler trajectories do not present any major differences. It is shown that the heliogyro performs similarly to the fixed-area solar sail, while not requiring an additional ACS that would degrade sailcraft performance.

6.3 Heliogyro coupled roto-translational motion

The coupled roto-translational motion of the heliogyro is analyzed in this subsection by analyzing the heliogyro motion of cases 1b and 1c from Table 3. Both cases use the heliogyro design from the baseline case 1a, but with different dynamical models.

Case 1b uses the non-averaged dynamical model from subsection 3.2 to validate the assumptions of the averaged model for the interplanetary trajectories analyzed within this paper. A one-week section of the EM leg is simulated and the results are visualized in Figure 12. In Figure 12a and b the position and velocity of the heliogyro are shown for the the averaged and the non-averaged models. It can be seen from the two plots that the two dynamical models produce extremely similar trajectories. The final averaged model error is negligible (less than one kilometer in position and one micrometer per second in velocity). Figure 12c shows the Euler angle ϕ describing the heliogyro orientation as a function of time, once again demonstrating the similarity between the averaged and non-averaged models. As seen in the detail, the non-averaged model produces some high-frequency variations, with the averaged model running through the average of the variations. The high-frequency variations are periodic with a frequency equal to $\frac{\omega_3}{2}$, corresponding to the period of the half-p profile.

In order to show that the trajectory design approach and coupled roto-translational model presented in this paper are also valid for non-co-planar cases, the EM leg is simulated in three dimensions with case 1c. The resulting EM leg solution is shown in Figure 13. The trajectory itself is shown in Figure 13a, with projections on the three planes of the *In-*

Table 4: Comparison of transfer and waiting times between fixed-area sailcraft cycler, heliogyro baseline cycler (case 1a) and cycler with zero-ME payload (case 2) .

	Transfer time [synodic periods]			Waiting times [synodic periods]	
	EM	ME	Total	Earth	Mars
Fixed-area solar sail	0.66	0.65	1.31	0.68	0.01
Baseline heliogyro (case 1a)	0.68	0.68	1.36	0.63	0.01
Zero-ME payload heliogyro (case 2; $\lambda^{EM} = 0.347$; $\lambda^{ME} = 0$)	0.65	0.55	1.20	0.75	0.05

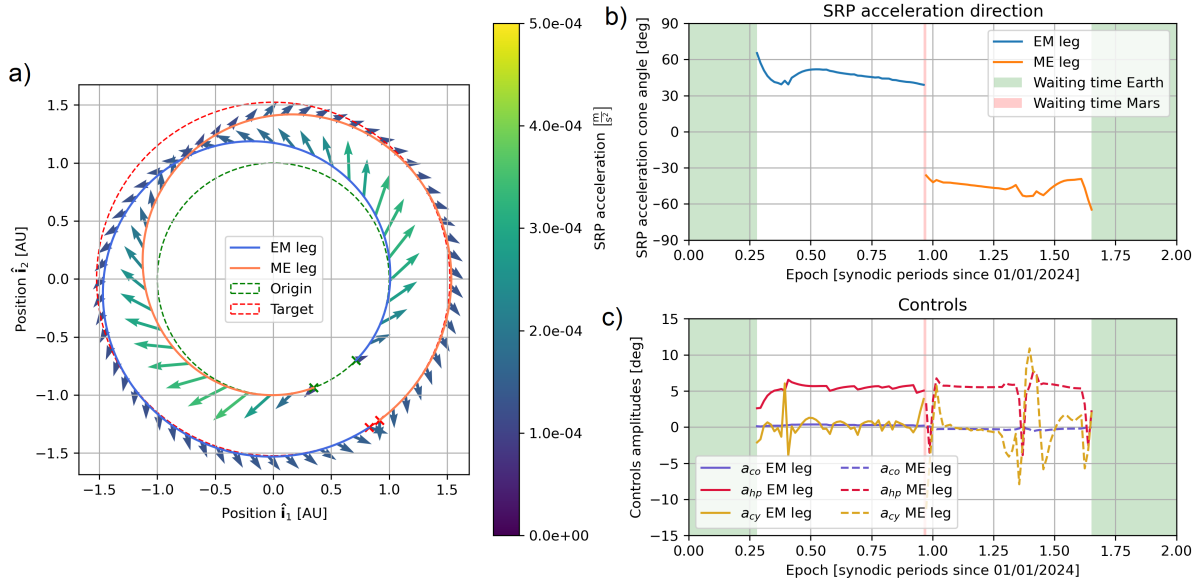


Fig. 11: Case 1a, baseline heliogyro cycler solution. In a) the two leg are presented, with arrows to show the force magnitude and direction, in b) the cone angle of the SRP acceleration vector as a function of time is visualized, while in c) the pitch profile controls $\mathbf{u}_r(t)$ are shown.

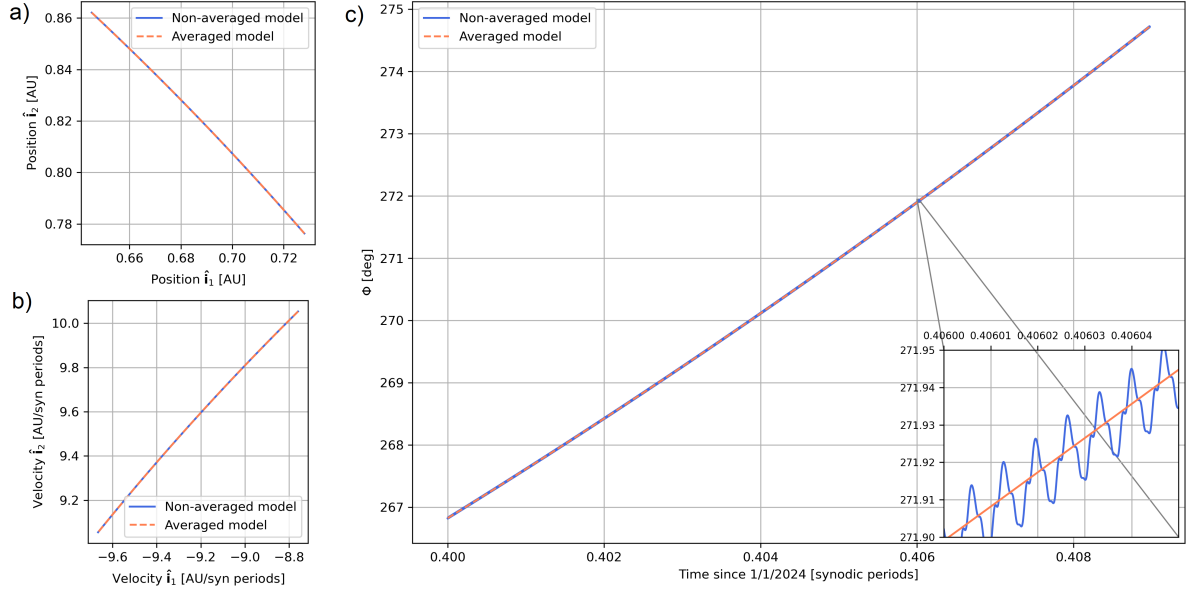


Fig. 12: Case 1a/1b, non-averaged model/averaged model comparison. Figures a) and b) display the position and velocity of the heliogyro, respectively, while c) shows the Euler angle ϕ describing the heliogyro orientation.

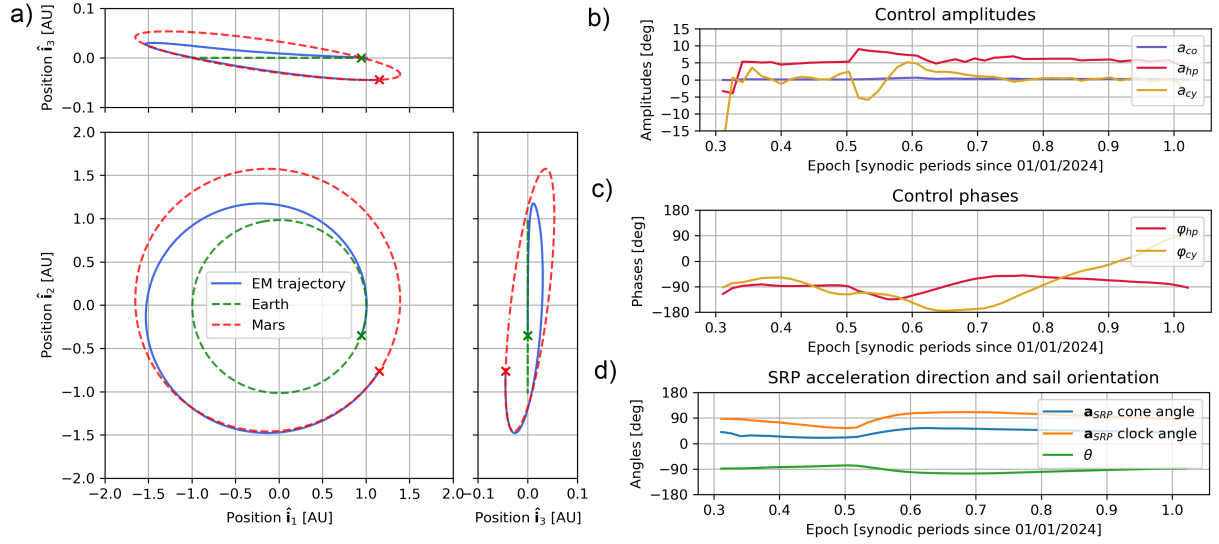


Fig. 13: Case 1c, non-co-planar EM trajectory. Figure a) shows the heliogyro trajectory on three perpendicular planes. Note that the \hat{i}_3 axis is stretched to show the heliogyro motion out of the \hat{i}_1 - \hat{i}_2 plane. The pitch profile controls \mathbf{u} are shown in b) and c) (amplitude and phases, respectively). Cone and clock angles of the SRP acceleration vector, as well as the second Euler angle θ describing the heliogyro orientation out-of-plane are displayed in d).

ertial reference frame $I(\hat{\mathbf{i}}_1, \hat{\mathbf{i}}_2, \hat{\mathbf{i}}_3)$. Note that the motion out of the $\hat{\mathbf{i}}_1$ - $\hat{\mathbf{i}}_2$ plane is exaggerated by stretching the $\hat{\mathbf{i}}_3$ axis. The control amplitudes and phases associated with the trajectory are shown in Figure 13b and c. The cone and clock angles of the SRP acceleration vector are displayed as a function of time in Figure 13d, as well as the second Euler angle θ that describes the heliogyro orientation out of the plane $\hat{\mathbf{i}}_1$ - $\hat{\mathbf{i}}_2$ plane. The first Euler angle ϕ is not displayed as it simply monotonically increases throughout the trajectory starting from a value around 180 and keeping the angle relative to the Sun around 35.26 degrees, similarly to case 1a.

As shown in Figure 13d, the second Euler angle θ is always approximately -90 degrees which indicates that the $\hat{\mathbf{d}}_1$ axis is always approximately aligned with the $\hat{\mathbf{i}}_3$ axis, meaning that the sailcraft spinning axis is always approximately lying on the ecliptic plane. The collective profile amplitude is close to zero throughout the trajectory, in order to generate zero moment $\bar{\mathbf{M}}_{\hat{\mathbf{d}}_3}$ (see Eq. 21). The half-p profile amplitude is a relatively constant positive angle in order to keep the heliogyro spin-axis close to the sunlight direction as the sailcraft revolves around the Sun.

As a reminder for the reader, in general a positive half-p amplitude with a zero phase angle produces a moment around the $\hat{\mathbf{d}}_1$ axis (the exact effect depends on the sailcraft orientation). The half-p phase angle rotates this moment around the $\hat{\mathbf{d}}_3$ to span the full $\hat{\mathbf{d}}_1$ - $\hat{\mathbf{d}}_2$ plane. The same is valid for the cyclic profile, which generates a lateral force component towards the $\hat{\mathbf{d}}_1$ axis with a positive amplitude and zero phase angle (in addition to a component in the $\hat{\mathbf{d}}_3$ direction, with the exact effect dependent on the sailcraft orientation). The lateral force component rotates around the $\hat{\mathbf{d}}_3$ axis as a function of the cyclic phase angle (positive phase angle produces a positive rotation) to span the full $\hat{\mathbf{d}}_1$ - $\hat{\mathbf{d}}_2$ plane.

Analyzing Figure 13c, the half-p phase angle varies around -90 degrees, to obtain a moment around $-\hat{\mathbf{d}}_2$ which produces a positive $\dot{\phi}$, see Eq. 21, considering that the Euler angle θ is approximately -90 degrees. Variations above -90 degrees also generate a moment component around the positive $\hat{\mathbf{d}}_1$ direction, therefore producing a positive $\dot{\theta}$, as explained in Eq. 21 and seen in Figure 13d. Similarly, half-p phase angles below -90 degrees produce negative $\dot{\theta}$. This movement out-of-plane is required to match Mars' orbital inclination.

The cone angle of the SRP acceleration vector has a similar profile as the one from case 1a explained earlier in subsection 6.2. The clock angle of the SRP acceleration vector varies around 90 degrees, meaning that the forces are mostly directed towards the $\hat{\mathbf{i}}$ axis, as expected, to increase the sailcraft tangential

velocity. Initially, the clock angle is slightly below 90 degrees, meaning the force vector is also pointing slightly towards the $\hat{\mathbf{p}}$ axis, which also corresponds approximately to the $\hat{\mathbf{d}}_1$ direction and the $\hat{\mathbf{i}}_3$ direction, as mentioned previously. This upward movement is needed to match Mars' orbital inclination. Later, the clock angle goes above 90 degrees, which allows the sailcraft to move towards $-\hat{\mathbf{i}}_3$ to reach Mars.

The generation of these out-of-plane ($\hat{\mathbf{i}}_1$ - $\hat{\mathbf{i}}_2$ plane) forces that are visible in the clock angle profile from Figure 13d can be explained by looking at the combination of amplitude and phase angles of the cyclic profile (a_{cy} and φ_{cy}): when the amplitude is positive and the phase is above -90 degrees, a force component towards $+\hat{\mathbf{d}}_1$ is generated (corresponding to a clock angle less than 90 degrees). A force component towards $+\hat{\mathbf{d}}_1$ is also generated when the amplitude is negative, and the phase angle is below -90 degrees. Instead, when the amplitude angle is positive and the phase angle is below -90 degrees, a force component towards $-\hat{\mathbf{d}}_1$ is generated (corresponding to a clock angle larger than 90 degrees).

Overall, the heliogyro is capable of completing the three-dimensional EM leg in 0.71 synodic periods, which constitutes an increase of less than 5% compared to the co-planar trajectory transfer time. Through the two cases, it is shown that the averaged model is suitable for modeling the coupled roto-translational motion of the heliogyro for co-planar interplanetary trajectories. In addition to that, it is demonstrated that the trajectory design approach is capable of solving the heliogyro interplanetary transfer problem also in the non-co-planar cases to generate more realistic trajectories.

6.4 Heliogyro trajectory sensitivity analysis

This subsection presents the sensitivity of the baseline cycler (case 1a) by independently varying the payload ratio of both legs (same for both legs, case 2), the payload ratio of only the EM leg (with payload ratio of the ME leg set to zero, case 3), and the spin-rate (case 4), as described in subsection 4.4 and Table 3.

The results of the sensitivity analysis relative to the payload ratio of both legs (and therefore lightness number, case 2) are visualized in Figure 14. The resulting cycler trajectories as a function of lightness number/payload ratio are shown in Figure 14a. Different colors indicate different lightness numbers/payload ratios. The transfer and waiting times of the resulting trajectories are shown in Figure 14b. It can be seen how the transfer times decrease for larger sailcraft performance, i.e. smaller payload ratio or larger lightness number, while the

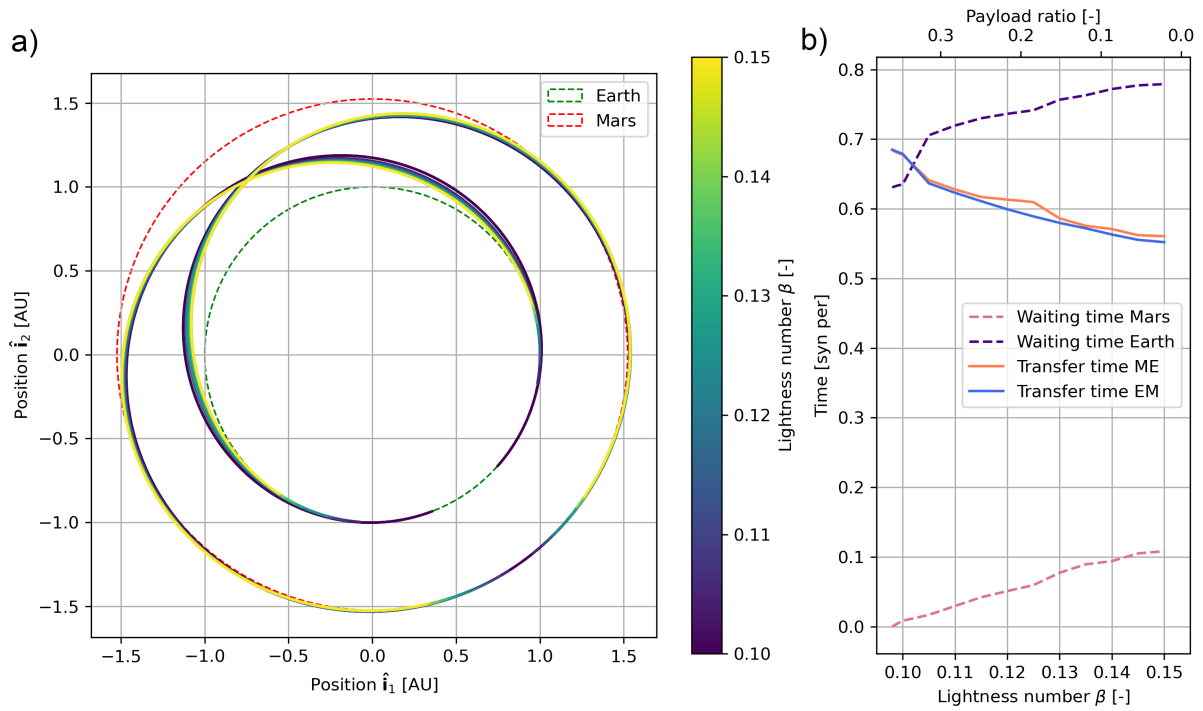


Fig. 14: Case 2, sensitivity analysis relative to the payload ratio of both legs/lightness number. In a) the cyclers trajectories are shown with different colors for each lightness number. In b) the transfer and waiting times are plotted as a function of lightness number.

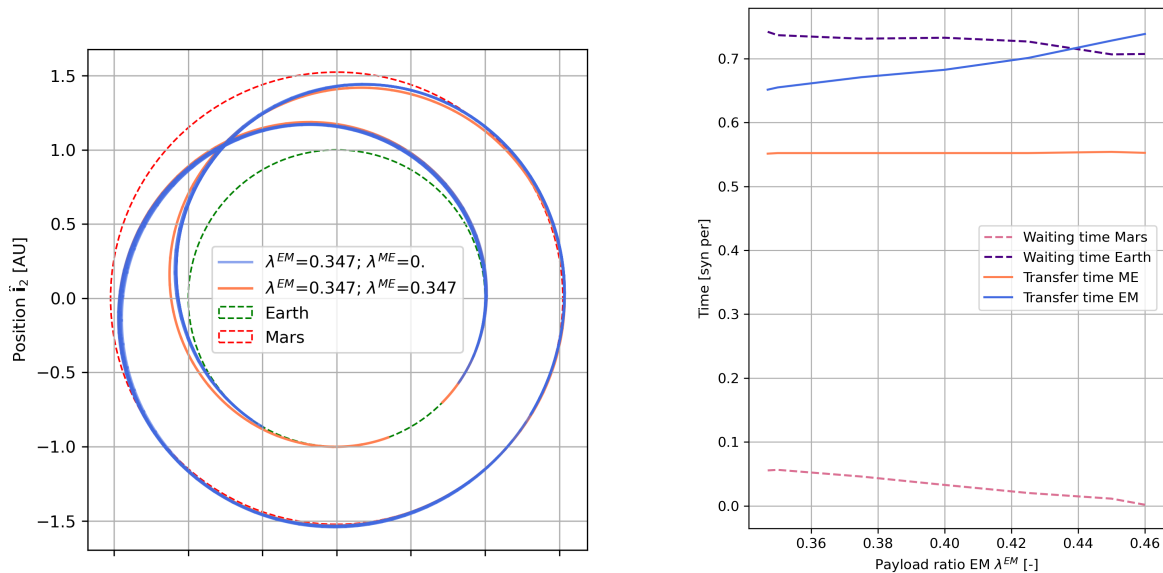


Fig. 15: Cyclers trajectory comparison between baseline case (case 1a) and cyclers with $\lambda^{EM} = 0.347$ and $\lambda^{ME} = 0$ (case 3).

Fig. 16: Case 3, cyclers transfer and waiting times as a function of EM payload ratio; with zero ME payload ratio.

waiting times increase, as expected. For all cases, the sum of all waiting and transfer times equals two synodic periods, the cycler period. The waiting time at Mars is the limiting constraint which makes the two-synodic periods cycler unfeasible for lightness numbers less than 0.098 ($\lambda = 0.36$). Furthermore, even at maximum lightness number, β_0 , the sum of the transfer times is above one synodic period, therefore indicating that a much larger sailcraft performance is needed for a one-synodic period cycler. Even if the sum of the transfer times would be slightly below one synodic period, the cycler would still not have a period of one synodic period due to the non-optimal relative position between Earth and Mars, which would force the sailcraft to have non-negligible waiting times.

The cycler trajectory when only transporting payload on the EM leg (case 3) is shown in Figure 15. Two trajectories are shown to highlight the differences: in orange the baseline cycler (case 1a, $\lambda^{EM} = 0.347$; $\lambda^{ME} = 0.347$) and in blue the case transporting payload only on the EM leg ($\lambda^{EM} = 0.347$; $\lambda^{ME} = 0$). The waiting and transfer times of the aforementioned cases are also shown in the second and third row of Table 4.

In the table it is shown that both transfer times of the zero-ME-payload are shorter. The difference between the two trajectories is also clearly visible in the figure. The EM leg of the zero-ME-payload cycler has a shorter transfer time and departs slightly later to arrive with more optimal conditions at Mars (as there are looser constraints on the returning ME leg because of the shorter transfer time). After waiting at Mars, the ME leg arrives back at Earth significantly earlier than the baseline cycler, due to the shorter transfer time due to the better sailcraft performance with zero-payload.

The waiting and transfer times of the cycler trajectories are displayed as a function of EM payload in Figure 16. Note that the ME payload ratio λ^{ME} is set to zero. Transfer times of the ME legs are constant, while the transfer time of the EM leg increases with increasing EM payload ratio. This is expected as the sailcraft performance is the same for all ME legs while it decreases for the EM legs with larger EM payload ratio. Waiting times also decreases with increasing EM payload ratio, up to the highest feasible EM payload ratio of 0.46 which makes the waiting time at Mars approach zero. By increasing the payload ratio of approximately 11% (from 0.347 to the maximum of 0.46), 60% more payload mass can be transported, making this option very attractive in case no payload needs to be transported from Mars to Earth.

Finally, the results of the sensitivity analyses of the

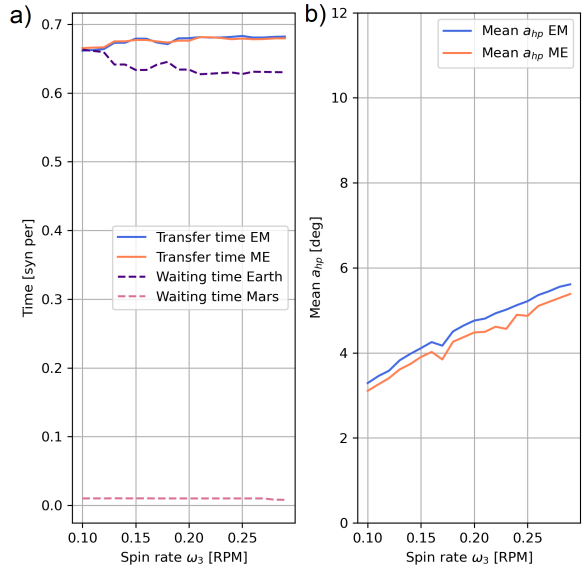


Fig. 17: Case 4, cycler sensitivity as a function of spin-rate ω_3 . In a) the waiting and transfer times are shown as a function of spin-rate, while in b) the mean amplitude of the half-p pitch profile is plotted as a function of the spin-rate.

cycler trajectories relative to the spin-rate ω_3 are displayed in Figure 17. In Figure 17a the transfer and waiting times are shown as a function of the spin-rate. The transfer time increases with increasing spin-rate, but the trend is not as clear as for the other sensitivity analyses. The mean amplitude of the half-p profile for each leg is shown as a function of spin-rate in Figure 17b. This is presented because the required moment to achieve the desired sailcraft rotation rate $\dot{\phi}$ varies as a function of the spin-rate ω_3 (see Eq. 21) and the generated SRP moment magnitude is dependent on the amplitude of the half-p profile a_{hp} . As expected, there is a direct proportionality between the required mean amplitude of the half-p profile and the sailcraft spin-rate. For a larger spin-rate, a larger moment is needed to generate the same sailcraft rotation rate $\dot{\phi}$ (gyroscopic stiffness, see Eq. 21). This larger moment is generated by increasing the amplitude of the half-p profile. The maximum spin-rate that still allows for a non-zero waiting time at Mars is 0.29 RPM.

Overall, the sensitivity analyses in this section demonstrate that the heliogyro has significant flexibility in terms of enabling a two-synodic period cycler even when varying many of the most critical design parameters.

7. Conclusion

Two novel models describing the heliogyro coupled roto-translational dynamics have been presented in this paper. The spin-averaged model was used to design Earth-to-Mars cyler trajectories with a cyler period of two Earth-Mars synodic periods (approximately 780 Earth days).

The heliogyro coupled roto-translational dynamical models were showcased and analyzed both in two and three dimensions, demonstrating that the spin-averaged model can be used for trajectory design as a part of preliminary mission design. The results of the non-averaged model were compared to the spin-averaged model demonstrating the validity of the assumptions underlying the spin-averaged model in the context of interplanetary trajectories.

The heliogyro trajectories were compared to fixed-area sailcraft cyler trajectories with equivalent sailcraft-performance. It was shown that the heliogyro achieves similar transfer times as the fixed-area sailcraft trajectories, without the need for an additional attitude control system that may degrade the sailcraft performance. Finally, several sensitivity analyses were performed to demonstrate the flexibility and robustness of the heliogyro design which demonstrated that a two-synodic-period cyler is feasible even when varying critical design parameters of the heliogyro.

References

- [1] C. McInnes. *Solar Sailing: Technology, Dynamics and Mission Applications*. Springer Praxis Books. Springer Berlin Heidelberg, 2010.
- [2] Y. Tsuda, O. Mori, R. Funase, et al. Achievement of IKAROS — Japanese deep space solar sail demonstration mission. *Acta Astronautica*, 82(2):183–188, 2013.
- [3] D. Alhorn, J. Casas, E. Agasid, et al. NanoSail-D: The Small Satellite That Could!, 2011.
- [4] D. A. Spencer, B. Betts, J. M. Bellardo, et al. The LightSail 2 solar sailing technology demonstration. *Advances in Space Research*, 67(9): 2878–2889, 2021.
- [5] T. R. Lockett, J. Castillo-Rogez, L. Johnson, et al. Near-Earth Asteroid Scout Flight Mission. *IEEE Aerospace and Electronic Systems Magazine*, 35(3):20–29, 2020.
- [6] J. B. Pezent, R. Sood, A. Heaton, et al. Preliminary trajectory design for NASA’s Solar Cruiser: A technology demonstration mission. *Acta Astronautica*, 183:134–140, 2021.
- [7] W. K. Wilkie. Overview of the NASA Advanced Composite Solar Sail System (ACS3) Technology Demonstration Project. In *AIAA Scitech 2021 Forum*, 2021.
- [8] R. MacNeal. The Heliogyro - An Interplanetary Flying Machine. Technical report, Astro Research Corporation, 1967.
- [9] Macneal-Schwendler corporation. Heliogyro preliminary design, phase II Final Report. Technical report, Jet Propulsion Laboratory, 1978.
- [10] J. Heiligers, D. Guerrant, and D. Lawrence. Exploring the Heliogyro’s Orbital Control Capabilities for Solar Sail Halo Orbits. *Journal of Guidance, Control, and Dynamics*, 40(10):2569–2586, 2017. Publisher: American Institute of Aeronautics and Astronautics.
- [11] D. Guerrant and D. Lawrence. Heliogyro Attitude Control Moment Authority via Blade Pitch Maneuvers. In M. Macdonald, editor, *Advances in Solar Sailing*, pages 667–686. Springer Berlin Heidelberg, Berlin, Heidelberg, 2014.
- [12] B. Wie. Solar Sail Attitude Control and Dynamics, Part 1. *Journal of Guidance, Control, and Dynamics*, 27(4):526–535, 2004.
- [13] B. Wie. Solar Sail Attitude Control and Dynamics, Part Two. *Journal of Guidance, Control, and Dynamics*, 27(4):536–544, 2004.
- [14] R. S. Blomquist. Design study of a solid-state heliogyro solar sail. Master’s thesis, MIT, 1990.
- [15] R. S. Blomquist. Solar blade nanosatellite development: Heliogyro deployment, dynamics, and control. In *AIAA/USU Conference on Small Satellites*, 1999.
- [16] R. S. Blomquist. *Heliogyro Control*. PhD thesis, Carnegie Mellon University, 2009.
- [17] W. K. Wilkie, J. E. Warren, M. W. Thompson, et al. The Heliogyro Reloaded. In *JANNAF 5th Spacecraft Propulsion Subcommittee Joint Meeting*, 2011.
- [18] W. K. Wilkie, J. E. Warren, L. G. Horta, et al. Heliogyro Solar Sail Research at NASA. In M. Macdonald, editor, *Advances in Solar Sailing*, Springer Praxis Books, pages 631–650. Springer, Berlin, Heidelberg, 2014.

- [19] D. Guerrant. *Performance quantification of heliogyro solar sails using structural, attitude, and orbital dynamics and control analysis*. PhD thesis, University of Colorado, 2015.
- [20] W. K. Wilkie, J. Warren, L. G. Horta, et al. Recent advances in heliogyro solar sail structural dynamics, stability, and control research. In *2nd AIAA Spacecraft Structures Conference*, page 0431, 2015.
- [21] S. C. Gibbs and E. H. Dowell. Solarelastic stability of the heliogyro. In *Advances in Solar Sailing*, pages 651–665. Springer, 2014.
- [22] D. Guerrant and D. Lawrence. Heliogyro solar sail blade twist stability analysis of root and reflectivity controllers. In *AIAA Guidance, Navigation, and Control Conference*, page 4842, 2012.
- [23] D. Guerrant and D. Lawrence. Nonlinear torsional dynamics and control of heliogyro solar sail blades. In *2nd AIAA Spacecraft Structures Conference*, page 0435, 2015.
- [24] J. Heiligers, D. Guerrant, and D. Lawrence. Solving the heliogyro’s inverse problem. In *AIAA/AAS Astrodynamics Specialist Conference*. American Institute of Aeronautics and Astronautics, 2016.
- [25] D. Guerrant and D. Lawrence. Tactics for Heliogyro Solar Sail Attitude Control via Blade Pitching. *Journal of Guidance, Control, and Dynamics*, 38(9):1785–1799, 2015. Publisher: American Institute of Aeronautics and Astronautics.
- [26] J. Kang and K.-C. Park. Computational Multi-body Dynamics of Heliogyro Solar Sail under Spin-Deployment. In *AIAA Scitech 2020 Forum*, Orlando, FL, 2020. American Institute of Aeronautics and Astronautics.
- [27] R. Stevens and I. M. Ross. Preliminary Design of Earth-Mars Cyclers Using Solar Sails. *Journal of Spacecraft and Rockets*, 42(1):132–137, 2005.
- [28] G. Mengali and A. Quarta. Solar-Sail-Based Stopover Cyclers for Cargo Transportation Missions. *Journal of Spacecraft and Rockets*, 44(4): 822–830, 2007.
- [29] M. Vergaaij and J. Heiligers. Time-optimal solar sail heteroclinic-like connections for an Earth-Mars cycler. *Acta Astronautica*, 152:474–485, 2018.
- [30] J. Diebel. Representing attitude: Euler angles, unit quaternions, and rotation vectors. *Matrix*, 58, 01 2006.
- [31] B. Wie. *Space Vehicle Dynamics and Control*. AIAA education series. American Institute of Aeronautics and Astronautics, 2008.
- [32] Y. Tsuda, T. Saiki, R. Funase, and Y. Mimasu. Generalized Attitude Model for Spinning Solar Sail Spacecraft. *Journal of Guidance, Control, and Dynamics*, 36(4):967–974, 2013. Publisher: American Institute of Aeronautics and Astronautics.
- [33] E. M. Standish, J. G. Williams, et al. Orbital ephemerides of the sun, moon, and planets. *Explanatory supplement to the astronomical almanac*, pages 279–323, 1992.
- [34] F. G. Losada. Controllability of solar-sail orbits in the Earth-Moon system. Master’s thesis, TU Delft, 2019.
- [35] G. G. Wawrzyniak and K. C. Howell. Numerical techniques for generating and refining solar sail trajectories. *Advances in Space Research*, 48(11): 1848–1857, 2011.
- [36] J. T. Betts. Survey of Numerical Methods for Trajectory Optimization. *Journal of Guidance, Control, and Dynamics*, 21(2):193–207, 1998.
- [37] J. T. Betts. *Practical Methods for Optimal Control and Estimation Using Nonlinear Programming, Second Edition*. Society for Industrial and Applied Mathematics, second edition, 2010.
- [38] M. Kelly. Transcription methods for trajectory optimization: a beginners tutorial. *arXiv: Optimization and Control*, 2017.
- [39] E. Pellegrini and R. P. Russell. On the Computation and Accuracy of Trajectory State Transition Matrices. *Journal of Guidance, Control, and Dynamics*, 39(11):2485–2499, November 2016.
- [40] O. Montenbruck and E. Gill. *Satellite Orbits*, volume 1. Springer-Verlag Berlin Heidelberg, 2000.
- [41] C. Büskens and D. Wassel. The ESA NLP Solver WORHP. In G. Fasano and J. D. Pintér, editors, *Modeling and Optimization in Space Engineering*, pages 85–110. Springer New York, New York, NY, 2013.
- [42] F. Biscani and D. Izzo. A parallel global multiobjective framework for optimization: pagmo. *Journal of Open Source Software*, 5(53):2338, 2020.

- [43] WORHP. Users' Guide to WORHP 1.14. Technical report, Steinbeis-Forschungszentrum Optimierung, Steuerung und Regelung, 2020.
- [44] P. Virtanen, R. Gommers, T. E. Oliphant, et al. SciPy 1.0: Fundamental Algorithms for Scientific Computing in Python. *Nature Methods*, 17:261–272, 2020.

3

Conclusion and recommendations

In this chapter the conclusion and recommendations of this thesis work are presented. First, in section 3.1 conclusions are given based on the original research questions from section 1.4. Later, in section 3.2, the recommendations and suggestions for future work are presented.

3.1. Conclusion

The main objective of this research work was to investigate the coupled roto-translational motion of the heliogyro, by developing a novel model and applying these models for the design of time-optimal Earth-Mars cyler trajectories.

Two models of the heliogyro coupled roto-translational dynamics have been successfully developed and showcased in the context of Earth-to-Mars cyler trajectories. In addition, the resulting heliogyro time-optimal Earth-to-Mars cyler trajectories have been compared to the time-optimal Earth-to-Mars cyler trajectories of an equivalent fixed-area sailcraft, demonstrating that the heliogyro is capable of achieving the same performance as a traditional fixed-area sailcraft.

These conclusions are complemented here by directly answering the research questions formulated in section 1.4:

1. *How can the rotational and translational motions of the heliogyro be coupled?*

Two novel models coupling, for the first time, the rotational and translational dynamics of the heliogyro have been developed, a spin-averaged model and a non-averaged one. The non-averaged model takes into account instantaneous SRP forces and moments acting on the sail and uses three Euler angles, three angular velocities and the position-velocity state of heliogyro to fully describe the state of the sailcraft. Instead, the averaged model computes spin-averaged SRP forces and moments, omitting the modelling of the sailcraft's spin-motion. The direction of the spinning axis is described through two Euler angles and is complemented by the spin-rate, the position, and the velocity of the sailcraft to fully model the heliogyro coupled roto-translational motion. The averaged model was shown to have similar results as the more accurate non-averaged one for the analyzed cases, while being significantly more computationally efficient. This makes it suitable to use for preliminary trajectory design of heliogyro missions.

2. *How can time-optimal heliogyro Earth-Mars cyler trajectories be designed while considering the coupled roto-translational motion of the sailcraft?*

The newly developed averaged model for the coupled roto-translational dynamics is suitable for the design of heliogyro trajectories in the case of time-optimal Earth-Mars cyler trajectories and similar scenarios due to its computational efficiency. The continuous optimal control problem (containing the averaged coupled roto-translational dynamics of the sailcraft) is transcribed into a discrete problem using a multiple shooting transcription which is subsequently solved using WORHP. The final solution is optimal for the tackled problem and takes into account the heliogyro coupled roto-translational motion of the sailcraft, for the first time within existing research about the heliogyro. The same general trajectory design methodology can be applied to other

heliogyro mission design problems, noting that the adopted solver and transcription method could be modified if necessary.

3. *Can the heliogyro obtain similar performances as an equivalent fixed-area sailcraft for an Earth-Mars cyler, without the need for a separate ACS?*

Yes, it can. The comparison between the resulting heliogyro trajectories and the ones for an equivalent lightness-number fixed-area sailcraft has shown that the heliogyro can achieve similar transfer times as the fixed-area sailcraft, completing the cyler in two synodic periods for the baseline heliogyro design, without the need for an ACS. Note that in practice an heliogyro sailcraft would have higher performance than an equivalent technology-level fixed-area sailcraft due to lower structural mass [22] and no need for a separate ACS. Therefore, the similarity between the heliogyro trajectories and the ones for an equivalent fixed-area sailcraft is even more impressive and highlights the significant potential of the heliogyro configuration.

4. *How sensitive are heliogyro time-optimal Earth-Mars cyler trajectories to the sailcraft design parameters such as lightness number, payload ratio and spin-rate?*

The sensitivity of the heliogyro time-optimal Earth-Mars cyler trajectories was analyzed by investigating how they vary as a function of the aforementioned parameters. As expected, increasing the lightness number (or equivalently decreasing the payload ratio) decreases the transfer times between the two planets. The minimum lightness number for which a two synodic period cyler was still possible was found to be 0.98, while the maximum lightness number tested (1.5) still resulted a cyler period of two synodic periods. In addition, it was also shown that by not transporting any payload from Mars to Earth the payload mass from Earth to Mars could be increased by up to 60% from the baseline case, a scenario that might be relevant in case of resupply missions for a Martian colony. Finally, it was shown that the impact of a varying spin-rate is limited, with increasing spin-rates increasing the gyroscopic effect and therefore requiring larger control inputs to generate larger SRP moments that modify the sailcraft orientation as it revolves around the Sun.

3.2. Recommendations

One of the major objectives of this research work was to develop a novel model for the coupled roto-translational dynamics of the heliogyro. This model was later applied to an interplanetary transfer case with a simplified gravitational model, but it can potentially be adapted to many other scenarios and serve as a basis for the mission design of any heliogyro mission and for future research on its capabilities. In this section recommendations for future work are described, proposing potential improvements of the model and suggesting new potential scenarios to analyze to learn more about the heliogyro capabilities.

Regarding the modeling of the heliogyro dynamics, the following recommendations are suggested (listing first the recommendations that would significantly improve the fidelity of the resulting trajectory):

- *Improve fidelity of gravitational and ephemerides model:*

In this work a simplified gravitational model was used, only taking into account the gravitational attraction of the Sun. A significant improvement in the accuracy of the results would be achieved by modifying the gravitational model to also take into account Earth and Mars's gravitational attraction. This could be done in many ways, for example including the planetary gravitational attractions as perturbing accelerations or adopting a more complex dynamical model. As done for a traditional solar-sail Earth-Mars (EM) cyler in [41], a patched circular three-body problem approach could significantly improve the accuracy of the resulting heliogyro trajectories. Special attention would be needed to ensure that correct transformations between inertial and rotating frames are implemented for the correctness of the heliogyro rotational dynamics. Depending on the adopted gravitational model and assumptions, different ephemerides models could be considered, for example including the inclination of the Martian orbit.

- *Improve fidelity of SRP force and moment models:*

A simplified model for the SRP forces and moments was adopted in this research work. One potential improvement for further research is to assess the impact of including more non-ideal effects in the force and moment models, as these can be significant [42, 43]. The effects of the sail blades' flexibility could also be included as the shape of the blade may severely affect the results.

In addition to improving the dynamical models related to the heliogyro motion, the capabilities of the sailcraft can be investigated further to analyze and uncover novel applications of the heliogyro. Using the newly developed models of the heliogyro coupled roto-translational motion, the following applications could be investigated (listing first recommendations that are potential continuations of the presented research work):

- *Analyze capabilities of heliogyro for planetary operations:*

Analyzing the capabilities of the heliogyro during planetary escape and capture would be extremely interesting to show the capabilities of the heliogyro and complement the work presented in this thesis. In fact, operations within the sphere of influence of a planet may be critical for heliogyro missions because of the large slew requirements and low orbital periods [22]. The coupled roto-translational motion dynamical model could be easily used for such scenarios by applying some minor modifications.

- *Explore capabilities of heliogyro for the design of novel non-Keplerian orbit families:*

The heliogyro has additional authority on the generated SRP forces and moments compared to traditional sailcraft. An example of this is the ability to generate forces that are not aligned with the direction of the incoming sunlight when the cone angle is zero. The vast existing research about non-Keplerian orbit achievable with traditional solar-sails design [1] could be complemented with novel families of non-Keplerian orbits only possible with the heliogyro, which may unlock exciting new mission concepts and opportunities. The coupled roto-translational dynamical model presented in this paper would be perfectly suitable for the task, with appropriate modifications depending on the scenario. An example of an achievable closed non-Keplerian orbit of the heliogyro designed using the averaged coupled roto-translational dynamical model is presented in subsection B.1.3.

- *Investigate orbit control capabilities of heliogyro:*

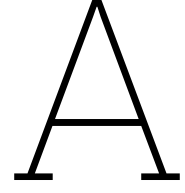
Orbit control authority of the heliogyro has been investigated using several simplifying assumptions and neglecting rotational dynamics, highlighting superior control capabilities of the sailcraft compared to traditional fixed-area square solar sails [32]. The same analysis could be performed with the novel coupled roto-translational dynamical model of the heliogyro to validate the findings with a more accurate model and investigate the effects of including pitch profile control and rotational motion.

Bibliography

- [1] C. McInnes. *Solar Sailing: Technology, Dynamics and Mission Applications*. Springer Praxis Books. Springer Berlin Heidelberg, 2010.
- [2] M. Macdonald and C. McInnes. Solar sail science mission applications and advancement. *Advances in Space Research*, 48(11):1702–1716, December 2011.
- [3] B. Fu, E. Sperber, and F. Eke. Solar sail technology—A state of the art review. *Progress in Aerospace Sciences*, 86:1–19, 2016.
- [4] L. Friedman, W. Carroll, R. Goldstein, et al. Solar sailing - The concept made realistic. In *16th Aerospace Sciences Meeting*, Aerospace Sciences Meetings. American Institute of Aeronautics and Astronautics, January 1978. doi: 10.2514/6.1978-82. URL <http://arc.aiaa.org/doi/10.2514/6.1978-82>.
- [5] Y. Tsuda, O. Mori, R. Funase, et al. Achievement of IKAROS — Japanese deep space solar sail demonstration mission. *Acta Astronautica*, 82(2):183–188, 2013.
- [6] D. Alhorn, J. Casas, E. Agasid, et al. NanoSail-D: The Small Satellite That Could!, 2011.
- [7] D. A. Spencer, B. Betts, J. M. Bellardo, et al. The LightSail 2 solar sailing technology demonstration. *Advances in Space Research*, 67(9):2878–2889, 2021.
- [8] T. R. Lockett, J. Castillo-Rogez, L. Johnson, et al. Near-Earth Asteroid Scout Flight Mission. *IEEE Aerospace and Electronic Systems Magazine*, 35(3):20–29, 2020.
- [9] W. K. Wilkie. Overview of the NASA Advanced Composite Solar Sail System (ACS3) Technology Demonstration Project. In *AIAA Scitech 2021 Forum*, 2021.
- [10] J. B. Pezent, R. Sood, A. Heaton, et al. Preliminary trajectory design for NASA's Solar Cruiser: A technology demonstration mission. *Acta Astronautica*, 183:134–140, 2021.
- [11] B. Wie. *Space Vehicle Dynamics and Control*. AIAA education series. American Institute of Aeronautics and Astronautics, 2008.
- [12] B. Wie. Solar Sail Attitude Control and Dynamics, Part 1. *Journal of Guidance, Control, and Dynamics*, 27(4):526–535, 2004.
- [13] B. Wie. Solar Sail Attitude Control and Dynamics, Part Two. *Journal of Guidance, Control, and Dynamics*, 27(4):536–544, 2004.
- [14] A. Bolle and C. Circi. Solar sail attitude control through in-plane moving masses. *Proceedings of the Institution of Mechanical Engineers, Part G: Journal of Aerospace Engineering*, 222(1):81–94, 2008. Publisher: IMECHE.
- [15] H. Price, J. Ayon, C. Garner, et al. Design for a solar sail demonstration mission. In *Space Technology and Applications International Forum*, 2001.
- [16] Z. Kun. Control Capability and Allocation of Solar Sail Tip Vanes over Bounded Movement. *Journal of Guidance, Control, and Dynamics*, 38(7):1340–1344, 2015. Publisher: American Institute of Aeronautics and Astronautics.
- [17] T. Saiki, Y. Tsuda, R. Funase, et al. Attitude Operation Results of Solar Sail Demonstrator IKAROS. *Transactions of the Japan society for aeronautical and space sciences*, 10(ists28), 2012.

- [18] A. Borggräfe, J. Heiligers, M. Ceriotti, and C. McInnes. Optical Control of Solar Sails using Distributed Reflectivity. In *Spacecraft Structures Conference*, AIAA SciTech Forum. American Institute of Aeronautics and Astronautics, 2014.
- [19] W. K. Wilkie, J. E. Warren, M. W. Thompson, et al. The Heliogyro Reloaded. In *JANNAF 5th Spacecraft Propulsion Subcommittee Joint Meeting*, 2011.
- [20] W. Wilkie, J. Warren, L. Horta, et al. Recent Progress in Heliogyro Solar Sail Structural Dynamics. In L. Ouwehand, editor, *13th European Conference on Spacecraft Structures, Materials & Environmental Testing*, volume 727 of *ESA Special Publication*, page 187, 2014.
- [21] D. Guerrant, K. Wilkie, and D. Lawrence. Heliogyro Blade Twist Control via Reflectivity Modulation. In *53rd Structures, Structural Dynamics and Materials Conference*, Structures, Structural Dynamics, and Materials and Co-located Conferences. American Institute of Aeronautics and Astronautics, 2012.
- [22] D. Guerrant. *Performance quantification of heliogyro solar sails using structural, attitude, and orbital dynamics and control analysis*. PhD thesis, University of Colorado, 2015.
- [23] R. MacNeal. The Heliogyro - An Interplanetary Flying Machine. Technical report, Astro Research Corporation, 1967.
- [24] Macneal-Schwendler corporation. Heliogyro preliminary design, phase II Final Report. Technical report, Jet Propulsion Laboratory, 1978.
- [25] R. S. Blomquist. Design study of a solid-state heliogyro solar sail. Master's thesis, MIT, 1990.
- [26] R. S. Blomquist. *Heliogyro Control*. PhD thesis, Carnegie Mellon University, 2009.
- [27] W. K. Wilkie, J. E. Warren, L. G. Horta, et al. Heliogyro Solar Sail Research at NASA. In M. Macdonald, editor, *Advances in Solar Sailing*, Springer Praxis Books, pages 631–650. Springer, Berlin, Heidelberg, 2014.
- [28] W. K. Wilkie, J. Warren, L. G. Horta, et al. Recent advances in heliogyro solar sail structural dynamics, stability, and control research. In *2nd AIAA Spacecraft Structures Conference*, page 0431, 2015.
- [29] S. Chad Gibbs and E. H. Dowell. Solarelastic stability of the heliogyro. In *Advances in Solar Sailing*, pages 651–665. Springer, 2014.
- [30] D. Guerrant and D. Lawrence. Heliogyro solar sail blade twist stability analysis of root and reflectivity controllers. In *AIAA Guidance, Navigation, and Control Conference*, page 4842, 2012.
- [31] D. V. Guerrant and D. A. Lawrence. Nonlinear torsional dynamics and control of heliogyro solar sail blades. In *2nd AIAA Spacecraft Structures Conference*, page 0435, 2015.
- [32] J. Heiligers, D. Guerrant, and D. Lawrence. Exploring the Heliogyro's Orbital Control Capabilities for Solar Sail Halo Orbits. *Journal of Guidance, Control, and Dynamics*, 40(10):2569–2586, 2017. Publisher: American Institute of Aeronautics and Astronautics.
- [33] J. Heiligers, D. Guerrant, and D. Lawrence. Solving the heliogyro's inverse problem. In *AIAA/AAS Astrodynamics Specialist Conference*. American Institute of Aeronautics and Astronautics, 2016.
- [34] D. Guerrant and D. Lawrence. Tactics for Heliogyro Solar Sail Attitude Control via Blade Pitching. *Journal of Guidance, Control, and Dynamics*, 38(9):1785–1799, 2015. Publisher: American Institute of Aeronautics and Astronautics.
- [35] J. Kang and K.-C. Park. Computational Multibody Dynamics of Heliogyro Solar Sail under Spin-Deployment. In *AIAA Scitech 2020 Forum*, Orlando, FL, 2020. American Institute of Aeronautics and Astronautics.
- [36] M. Bassetto, A. A. Quarta, A. Caruso, and G. Mengali. Optimal heliocentric transfers of a Sun-facing heliogyro. *Aerospace Science and Technology*, 119:107094, 2021. ISSN 1270-9638.

- [37] D. Guerrant and D. Lawrence. Heliogyro Attitude Control Moment Authority via Blade Pitch Maneuvers. In M. Macdonald, editor, *Advances in Solar Sailing*, pages 667–686. Springer Berlin Heidelberg, Berlin, Heidelberg, 2014.
- [38] D. V. Byrnes, J. M. Longuski, and B. Aldrin. Cyclers orbit between Earth and Mars. *Journal of Spacecraft and Rockets*, 30(3):334–336, June 1993.
- [39] G. Mengali and A. A. Quarta. Solar-Sail-Based Stopover Cyclers for Cargo Transportation Missions. *Journal of Spacecraft and Rockets*, 44(4):822–830, 2007.
- [40] R. Stevens and I. M. Ross. Preliminary Design of Earth-Mars Cyclers Using Solar Sails. *Journal of Spacecraft and Rockets*, 42(1):132–137, 2005.
- [41] M. Vergaaij and J. Heiligers. Time-optimal solar sail heteroclinic-like connections for an Earth-Mars cycler. *Acta Astronautica*, 152:474–485, 2018.
- [42] B. A. Campbell and S. J. Thomas. Realistic Solar Sail Thrust. In M. Macdonald, editor, *Advances in Solar Sailing*, pages 407–435. Springer Berlin Heidelberg, Berlin, Heidelberg, 2014.
- [43] Y. Tsuda, T. Saiki, R. Funase, and Y. Mimasu. Generalized Attitude Model for Spinning Solar Sail Spacecraft. *Journal of Guidance, Control, and Dynamics*, 36(4):967–974, 2013. Publisher: American Institute of Aeronautics and Astronautics.
- [44] J. Diebel. Representing attitude: Euler angles, unit quaternions, and rotation vectors. *Matrix*, 58, 01 2006.
- [45] M. Kelly. Cannon example, feb 2015. URL <http://www.matthewpeterkelly.com/tutorials/trajectoryOptimization/canon.html>. [Accessed: 2022-11-20].
- [46] P. Virtanen, R. Gommers, T. E. Oliphant, et al. SciPy 1.0: Fundamental Algorithms for Scientific Computing in Python. *Nature Methods*, 17:261–272, 2020.
- [47] F. L. Markley and J. L. Crassidis. *Fundamentals of spacecraft attitude determination and control*. Springer, 2014.
- [48] F. Müller. Goddard’s rocket problem. https://mintoc.de/index.php/Goddart%27s_rocket_problem, feb 2016. [Accessed: 2022-10-31].



Reference frames transformations

In this appendix the reference frame transformations used throughout the research work are described. Only rotations are presented as they are the only reference frame transformations used.

The basic reference frame rotations for an arbitrary angle γ are [11]:

$$\mathbf{R}_1(\gamma) = \begin{bmatrix} 1 & 0 & 0 \\ 0 & \cos \gamma & \sin \gamma \\ 0 & -\sin \gamma & \cos \gamma \end{bmatrix}, \mathbf{R}_2(\gamma) = \begin{bmatrix} \cos \gamma & 0 & -\sin \gamma \\ 0 & 1 & 0 \\ \sin \gamma & 0 & \cos \gamma \end{bmatrix}, \mathbf{R}_3(\gamma) = \begin{bmatrix} \cos \gamma & \sin \gamma & 0 \\ -\sin \gamma & \cos \gamma & 0 \\ 0 & 0 & 1 \end{bmatrix} \quad (\text{A.1})$$

The attitude of the heliogyro is represented through 3 Euler angles (ϕ , θ , and ψ) using a 3-2-3 rotation sequence, as follows:

$$\mathbf{x}^{[B]} = [BI]\mathbf{x}^{[I]} = \mathbf{R}_3(\psi)\mathbf{R}_2(\theta)\mathbf{R}_3(\phi)\mathbf{x}^{[I]} \quad (\text{A.2})$$

The relation between body-fixed angular velocities $\boldsymbol{\omega}^{[B]}$ expressed in the *Body* reference frame, relative to the *Inertial* reference frame are related to the time-derivative of the Euler angles [44]:

$$\begin{bmatrix} \dot{\phi} \\ \dot{\theta} \\ \dot{\psi} \end{bmatrix} = \frac{1}{\sin \theta} \begin{bmatrix} -\cos \psi & \sin \psi & 0 \\ \sin \theta \sin \psi & \sin \theta \cos \psi & 0 \\ \cos \theta \cos \psi & -\cos \theta \sin \psi & \sin \theta \end{bmatrix} \boldsymbol{\omega}^{[B]} \quad (\text{A.3})$$

The other reference frames transformations used in the paper are presented here. The opposite rotations are obtained by simply inverting (or transposing) the rotation matrices.

- Transformation from *Inertial* to *Solar* reference frame:

$$\mathbf{x}^{[S]} = \mathbf{R}_2(\gamma_2)\mathbf{R}_3(\gamma_1)\mathbf{x}^{[I]} \quad (\text{A.4})$$

with:

$$\gamma_1 = \tan 2^{-1}(r_2, r_1); \gamma_2 = \sin^{-1}\left(\frac{r_3}{|\mathbf{r}^{[I]}|}\right) \quad (\text{A.5})$$

and $\mathbf{r}^{[I]}$ as the spacecraft position expressed in the *Inertial* reference frame and relative to the origin, with the subscript indicating the axis of the vector component:

$$\mathbf{r}^{[I]} = [r_1, r_2, r_3] \quad (\text{A.6})$$

- Transformation from *Inertial* to *Despun* reference frame:

$$\mathbf{x}^{[D]} = [DI]\mathbf{x}^{[I]} = \mathbf{R}_2(\theta)\mathbf{R}_3(\phi)\mathbf{x}^{[I]} \quad (\text{A.7})$$

- Transformation from *Despun* to *Body* reference frame:

$$\mathbf{x}^{[B]} = [BD]\mathbf{x}^{[D]} = \mathbf{R}_3(\psi)\mathbf{x}^{[D]} \quad (\text{A.8})$$

- Transformation from *Blade* to *Body* reference frame:

$$\mathbf{x}^{[B]} = [BL_i]\mathbf{x}^{[L_i]} = \mathbf{R}_3(-\xi_i)\mathbf{R}_1(-\vartheta_i)\mathbf{x}^{[L_i]} \quad (\text{A.9})$$

with i as an arbitrary blade number and:

$$\xi_i = 2\pi \frac{i-1}{N_b} \quad (\text{A.10})$$

with N_b as the number of blades.

- Transformation from *Blade* to *Despun* reference frame:

$$\mathbf{x}^{[D]} = [DL_i]\mathbf{x}^{[L_i]} = \mathbf{R}_3(-\psi_i)\mathbf{R}_1(-\vartheta_i)\mathbf{x}^{[L_i]} \quad (\text{A.11})$$

with:

$$\psi_i = \psi + \xi_i \quad (\text{A.12})$$

B

Verification and validation

In this appendix the verification and validation procedures used throughout the development of the required models and algorithms are presented. The tests used to verify the implementation of the developed models and algorithms are described in section B.1, while the study cases used to validate them are presented in section B.2.

B.1. Verification

Several verification procedures have been used to ensure the correctness of the implemented models and algorithms used throughout this research work. These verification steps are presented in this section, starting from the most basic implemented functionality (reference frames transformations) to the most complex ones.

B.1.1. Reference frames transformations

In order to verify the implemented reference frame transformations, unit-tests are performed for each reference frame transformation from appendix A. In practice, for each reference frame transformation, simple unit-vectors ($[1, 0, 0]^T$, $[0, 1, 0]^T$, and $[0, 0, 1]^T$) are rotated over predictable angles such as zero, $\frac{\pi}{4}$, $\frac{\pi}{2}$, or π radians and the results are compared to the expected ones. It was found that all reference frame rotations matched the expected results up to a maximum component-wise error threshold of 10^{-7} , with the leftover error attributable to numerical round-off.

The implementation is further verified by testing the concatenation of multiple reference frame rotations. An arbitrary vector is rotated to multiple reference frames and then finally back to the original frame, comparing it to the initial vector. This is done by rotating an arbitrary vector using the following frame transformation sequence $L_i \rightarrow D \rightarrow I \rightarrow S \rightarrow I \rightarrow B \rightarrow L_i$. If any of the reference transformations is incorrect the final vector will not match the initial one. The resulting vector was matching the original one up to a maximum component-wise error threshold of 10^{-7} , with the leftover error attributable to numerical round-off errors.

B.1.2. SRP Forces and Moments

In order to verify both the averaged and non-averaged SRP force and moment models, a series of unit-tests are performed to assess the correctness of the results. For all tests (unless specified otherwise) the sailcraft is placed at one astronomical unit away from the Sun (on the \hat{i}_1 axis of the *Inertial* reference frame), Euler angles ϕ and θ are set to π and $-\frac{\pi}{2}$ respectively (heliogyro sail perpendicular to sunlight direction), and the baseline heliogyro design from chapter 2 is used. For such heliogyro orientation and location, axes \hat{i}_3 , \hat{p} , and \hat{d}_1 are aligned, as well as \hat{i}_1 , \hat{d}_3 and \hat{s} , while \hat{i}_2 is in the opposite direction as \hat{d}_2 . The following cases were analyzed for both the spin-averaged and non averaged models to verify the correctness of the SRP force results, with all pitch profiles set to zero:

1. Verify that the SRP force has the same direction as the sunlight direction when the sail normal has the same direction as the sunlight one (cone angle α of zero).

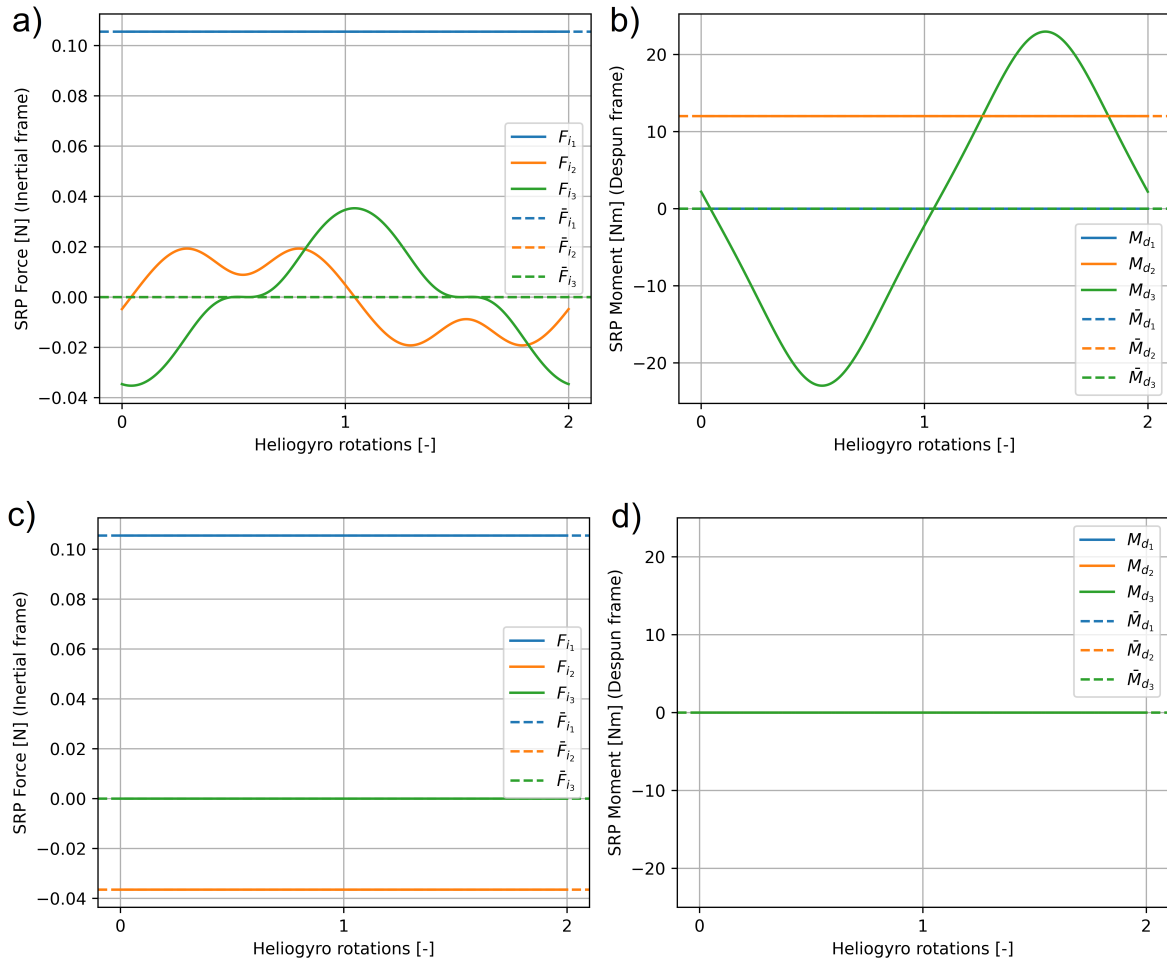


Figure B.1: SRP forces (figures a) and c), *Inertial* reference frame) and moments (figures b) and d), *Despun* reference frame) corresponding to cases eight (figures a) and b)) and nine (figures c) and d)). Non-averaged results displayed with solid line, averaged with dashed lines.

2. Verify that the SRP force has the same direction as the sunlight direction when the sail normal has the opposite direction as the sunlight one (as both sides of the sides are reflective).
3. Verify that the SRP force is zero when the sail normal is perpendicular to the sunlight direction (cone angle α of $\frac{\pi}{2}$).
4. Verify that the SRP force direction has the same or opposite direction as the sail normal for an arbitrary sail normal direction.

The results of all aforementioned tests were verified to be correct up to a negligible error (maximum component-wise error threshold of 10^{-7}).

In order to further verify the moment models (both spin-averaged and non-averaged models), the following cases were also analyzed:

5. Verify that the SRP moment is zero for all aforementioned cases.
6. Setting the collective pitch profile to $\frac{\pi}{4}$ and the sail normal direction aligned with the sunlight one, verify that the SRP moment is pointed along the sunlight direction.
7. Setting the collective pitch profile to $\frac{\pi}{4}$ and the sail normal direction opposite to the sunlight one (cone angle α of π), verify that the SRP moment is pointed along the sunlight direction.

Once again, the results of all aforementioned tests were verified to be correct up to a negligible error (maximum component-wise error threshold of 10^{-7}).

On top of these tests, the implementations of both averaged and non-averaged force and moment models are tested by analyzing two additional cases:

8. Verify that an average lateral moment towards $\hat{\mathbf{d}}_2$ is obtained when setting the half-p pitch profile amplitude to $\frac{\pi}{4}$, its phase to $\frac{\pi}{2}$ and the sail normal direction aligned with the sunlight one.
9. Verify that an average lateral force towards $\hat{\mathbf{d}}_2$ is obtained when setting the cyclic pitch profile amplitude to $\frac{\pi}{4}$, its phase to $\frac{\pi}{2}$ and the sail normal direction aligned with the sunlight one.

The generated SRP forces and moments for these two cases are shown in Figure B.1, with the former case shown in Figure B.1a and b, and the latter one in Figure B.1c and d. As expected, it is clear that for all cases the spin-averaged results are either overlapping or passing through the average of the non-averaged signal (over two heliogyro rotations). As expected for case eight (half-p pitch profile), only an averaged force in the $\hat{\mathbf{i}}_1$ direction (sunlight direction $\hat{\mathbf{s}}$) is present (so no lateral forces), as well as an average moment in the $\hat{\mathbf{d}}_2$ direction. For case nine (cyclic pitch profile), the same force in $\hat{\mathbf{i}}_1$ - $\hat{\mathbf{s}}$ direction is present, as well as a lateral force in the negative $\hat{\mathbf{i}}_2$ direction (corresponding to positive $\hat{\mathbf{d}}_2$ direction) and no moments. For all cases the expected results are achieved.

To further verify the SRP force and moment models some of the results presented in [37] are reproduced. Both the models presented in this research work and the ones from [37] are simulating SRP forces and moments generated by the heliogyro but in slightly different ways (different reference frames definition and equations). If the same results are obtained, the model presented in this paper can be considered validated.

Figure 4 and 5 from [37] are reproduced and the results are shown in Figure B.2 and B.3. In Figure B.2 the SRP forces and moments are visualized as a function of cone angle, while in Figure B.3 the SRP forces and moments are shown as a function of the pitch profile amplitudes, therefore covering all possible cases to verify.

The forces are plotted in the *Solar* reference frame to mimic the paper results, while moments are visualized in *Despun* reference frame. Note that the *Despun* reference frame defined in this research work is different from the one in [37], with the local $\hat{\mathbf{d}}_3$ axis corresponding to the external paper's $\hat{\mathbf{d}}_1$ axis, local $\hat{\mathbf{d}}_1$ corresponding to the external $\hat{\mathbf{d}}_3$, and local $\hat{\mathbf{d}}_2$ corresponding to the external $-\hat{\mathbf{d}}_2$.

As shown in the figures, the results appear the same after considering the difference in the definition of the *Despun* reference frame, therefore the SRP force and moment models can be considered verified.

B.1.3. Dynamics

In order to verify the implemented dynamics, simple tests are performed to assess that the expected results are obtained. Similarly to subsection B.1.2, unless specified otherwise, the sailcraft position is set to one astronomical unit away from the Sun (on the $\hat{\mathbf{i}}_1$ axis of the *Inertial* reference frame) and the baseline heliogyro design is used. The sailcraft is set to orbit the Sun counter-clockwise (on a circular orbit when ignoring SRP forces, with the same orbital velocity as Earth) and the ending time for all propagation is set to one quarter of the equivalent circular orbit period. For all propagation a Runge-Kutta (RK)45 integrator is used with a value of 10^{-12} for the absolute and the relative tolerance to minimize integrator errors.

The translational dynamics (both averaged and non-averaged model) are tested by setting all pitch profiles to zero (therefore having the heliogyro acting as a fixed-area sailcraft) and varying the attitude to assess if the expected results are obtained. The cases are described as follows, with a visualization in Figure B.4 for better understanding.

1. The sailcraft orientation is modified such that the normal is initially oriented towards the velocity vector (therefore perpendicular to $\hat{\mathbf{s}}$) and stays constant (relative to the inertial frame) throughout the test. As the sailcraft revolves around the Sun, the sunlight should propel the spacecraft forward and increase the orbit's semi-major axis.
2. The sailcraft orientation is set such that the normal is initially aligned with $\hat{\mathbf{s}}$ and stays constant (relative to the *Inertial* reference frame) throughout the test. As the sailcraft revolves around the Sun, the generated SRP forces will act opposite to the tangential velocity (after the initial condition) and therefore decrease the orbit's semi-major axis.
3. The sailcraft normal is oriented above the orbit plane (slightly towards $\hat{\mathbf{i}}_3$), such that the sailcraft SRP force should propel the sailcraft out-of-plane, with a final positive $\hat{\mathbf{i}}_3$ position component.
4. The sailcraft normal is oriented below the orbit plane (slightly towards $-\hat{\mathbf{i}}_3$), such that the sailcraft SRP force should propel the sailcraft out-of-plane, with a final negative $\hat{\mathbf{i}}_3$ position component.

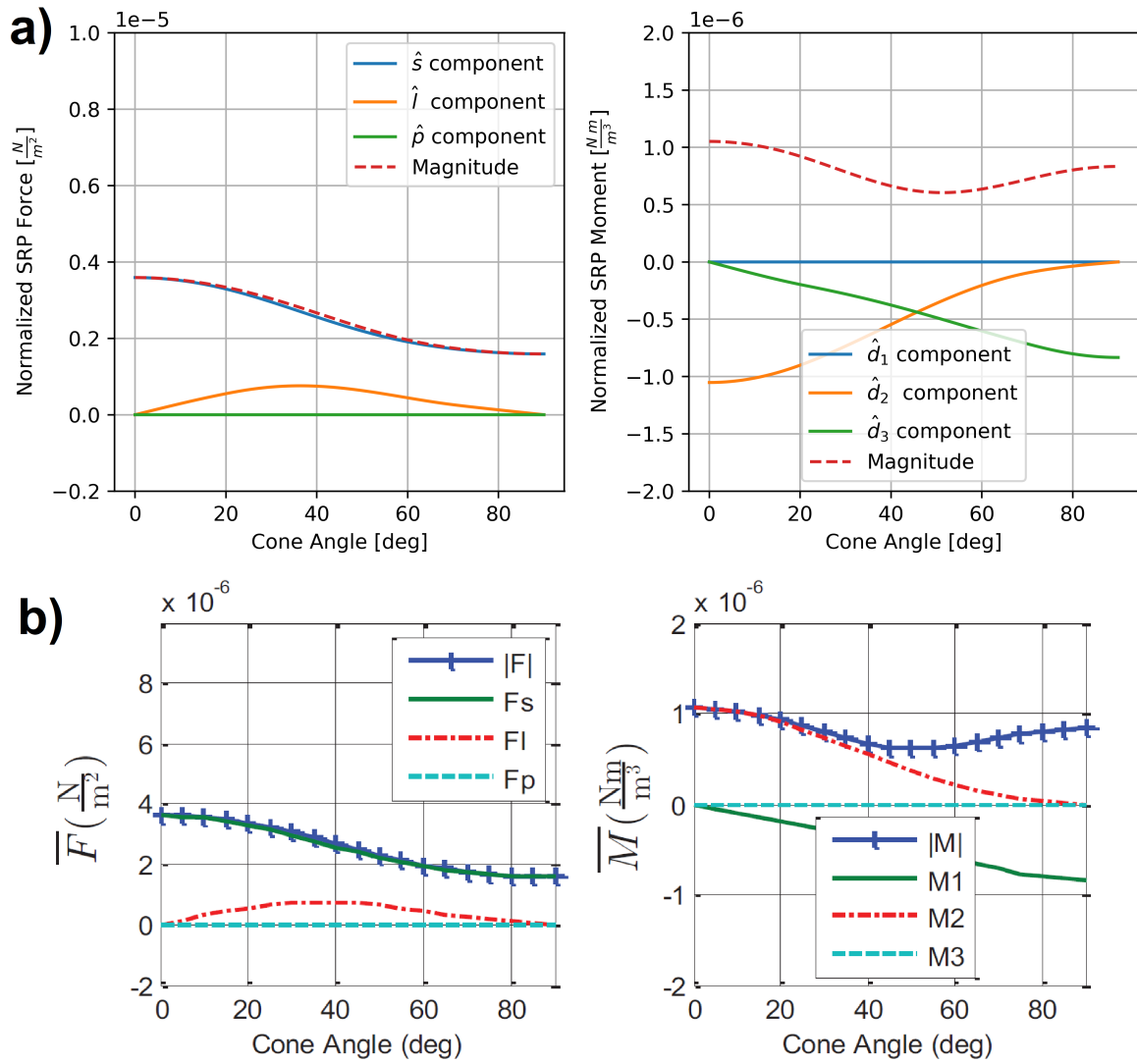


Figure B.2: Verification of SRP force and moment models, varying cone angle. Results from the implemented model in plot a), while the original results from Figure 4 of [37] in plot b).

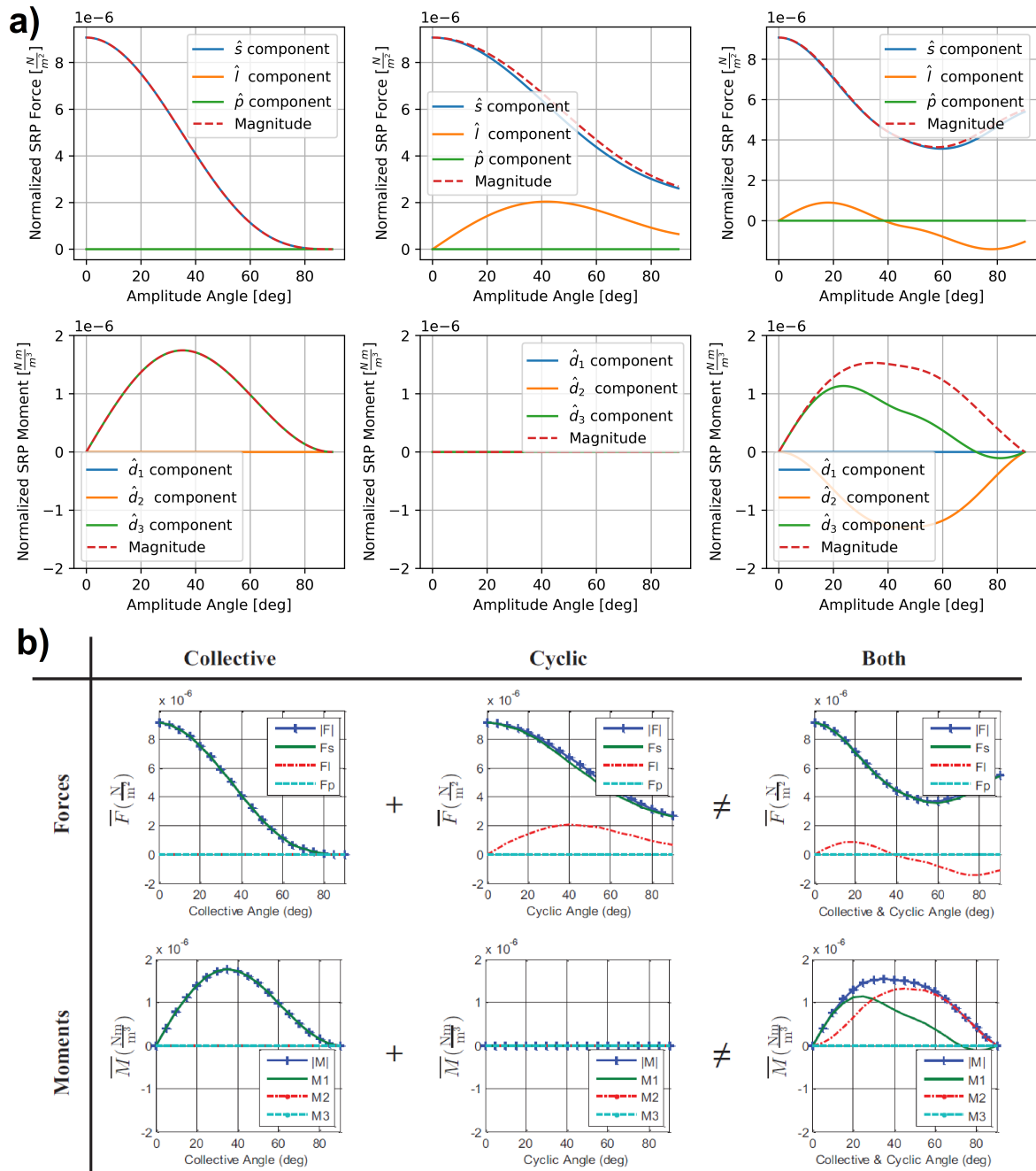


Figure B.3: Verification of SRP forces and moment models, varying pitch profiles. Results from the implemented model in plot a), the original results from Figure 5 of [37] in b).

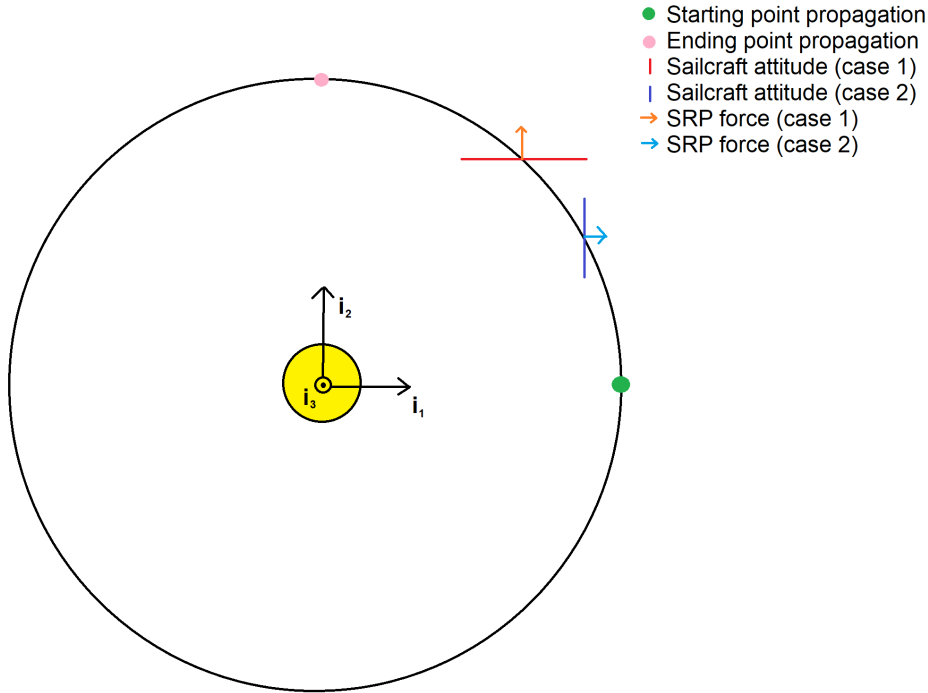


Figure B.4: Visualization of geometry and sail orientation for Cases 1 and 2 of the translational dynamics verification.

All cases were simulated and produced the expected results, therefore the translational dynamics are considered verified.

The rotational dynamics (both averaged and non-averaged model) are verified by performing similar tests. See sections 3.2 and 3.3 of chapter 2 to better understand the effect of control inputs on rotational dynamics. Similarly to before, the baseline heliogyro design is used, the sailcraft is placed at one astronomical unit away from the Sun (on the \hat{i}_1 axis of the *Inertial* reference frame), and Euler angles ϕ and θ are set to π and $-\frac{\pi}{2}$ respectively (sail normal aligned with \hat{i}_1 and \hat{s}).

1. The collective pitch profile is modified with a positive amplitude, such that the spin-rate of the sailcraft should increase.
2. The collective pitch profile is modified with a negative amplitude, such that the spin-rate of the sailcraft should decrease.
3. The half-p pitch profile is modified with a positive amplitude (phase to zero), such that the SRP moments in $\hat{\mathbf{a}}_1$ direction are generated and θ should increase.
4. The half-p pitch profile is modified with a positive amplitude (phase to π), such that the SRP moments in $-\hat{\mathbf{a}}_1$ direction are generated and θ should decrease.
5. The half-p pitch profile is modified with a positive amplitude (phase to $\frac{\pi}{2}$), such that the SRP moments in $\hat{\mathbf{a}}_2$ direction are generated and ϕ should decrease (note the negative θ).
6. The half-p pitch profile is modified with a positive amplitude (phase to $-\frac{\pi}{2}$), such that the SRP moments in $-\hat{\mathbf{a}}_2$ direction are generated and ϕ should increase (note the negative θ).

Once again, all expected results were obtained proving that rotational dynamics are verified.

The coupling of the rotational and translational dynamics is verified by reproducing a circular closed Sun-centered Non-Keplerian Orbit (NKO). Such case is analyzed because the results can be compared to existing literature [1] and both the rotational and translational dynamics of the heliogyro need to be implemented correctly to obtain the expected result. The baseline design of the heliogyro is used, with the sailcraft initially placed one astronomical unit away from the origin on the \hat{i}_1 axis and the spinning axis aligned with the \hat{i}_1 axis (such that sail orthogonal to the incoming sunlight). The scenario is simulated

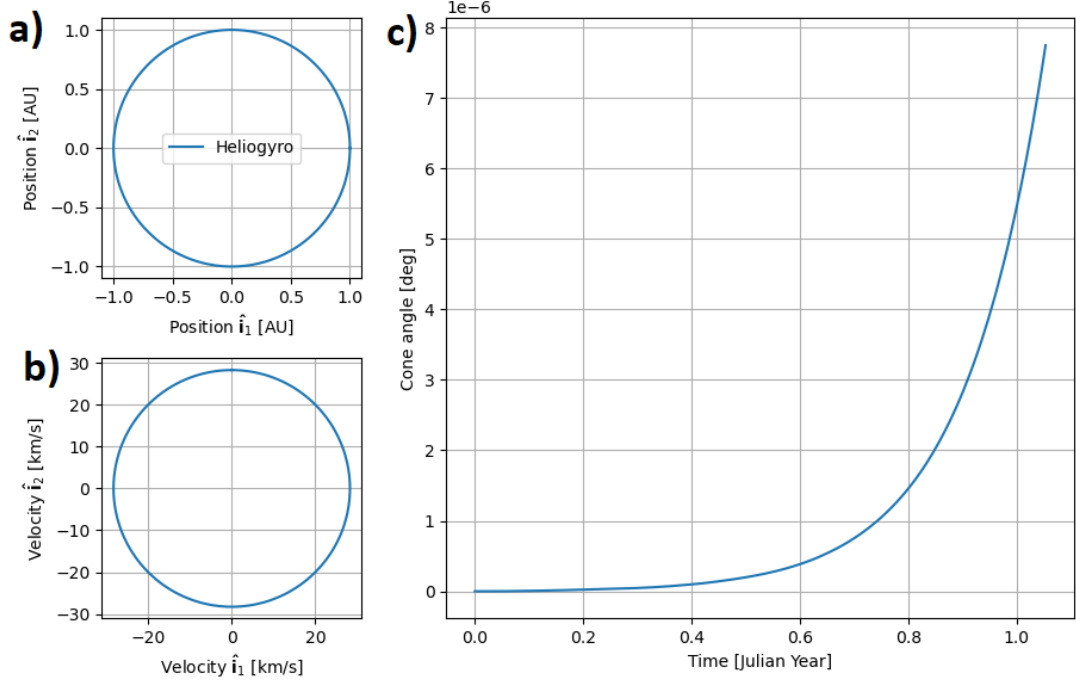


Figure B.5: Closed Non-Keplerian orbit for heliogyro dynamics validation. Position and velocity of the heliogyro shown respectively in Figures a) and b), while the cone angle of the sailcraft plotted as a function of time in Figure c).

using the averaged coupled roto-translational dynamical model. The objective is to obtain a circular orbit with a radius of one astronomical unit, always orienting the sail orthogonally to the incoming sunlight to achieve a different orbital period than the corresponding Keplerian orbit.

The heliogyro rotates using the half-p profile throughout the orbital revolution to keep the cone angle equal to zero. In order to achieve that, the appropriate amplitude value for the half-p pitch profile needs to be found. As the half-p pitch profile is active, the radial SRP acceleration will be lower than the equivalent SRP acceleration that a flat solar sail with the same lightness number and orientation would experience. The effective lightness number β_{eff} of the heliogyro is defined, representing the lightness number of a sailcraft with the sail fully orthogonal to the incoming sunlight and experiencing the same radial acceleration as the heliogyro:

$$\beta_{eff} = \beta \frac{acc_{SRP;hp}}{acc_{SRP;max}} \quad (B.1)$$

with $acc_{SRP;hp}$ representing the average SRP acceleration experienced by the heliogyro when the half-p profile is active and $acc_{SRP;max}$ as the maximum achievable SRP acceleration experienced by the sailcraft (when the sail is orthogonal to the incoming sunlight with all pitch profiles set to zero). The process to generate the NKO is iterative and consists of the following steps:

1. The orbital period P of the NKO is computed as [1]:

$$P = \frac{2\pi}{\sqrt{\mu_{\odot}}} (1 - \beta_{eff})^{-1/2} r^{3/2} \quad (B.2)$$

using $\beta_{eff} = \beta$ as an initial guess, with P as the orbital period.

2. The required rotation rate of the heliogyro $\dot{\phi}$ is computed from the orbital period:

$$\dot{\phi} = \frac{2\pi}{P} \quad (B.3)$$

3. The moment required to achieve the computed $\dot{\phi}$ is computed using Equation 21 of the research article.

4. The amplitude of the half-p pitch profile to achieve the desired moment is computed iteratively using Newton's method, with the gradient computed numerically using central difference (step of 10^{-5} radians) and a convergence criterion of 10^{-8} radians.
5. The effective lightness number is computed using Equation B.1.

The iterative process is considered converged when the residual of the effective lightness number between two iterations is less than 10^{-12} . It was found that a half-p amplitude of approximately 9.71 degrees allows the heliogyro to follow a closed NKO at 1 AU, with a corresponding period of approximately 1.0529 Julian years and an effective lightness number $\beta_{eff} = 0.09787$. Using the computed amplitude of the half-p pitch profile, the initial heliogyro state is propagated numerically using a RK4 integration for the complete period of the NKO. The initial heliogyro velocity V is computed as:

$$V = \sqrt{\frac{\mu_{\odot}(1 - \beta_{eff})}{r}} \quad (\text{B.4})$$

The results are shown in Figure B.5. Figure B.5a and b show the orbital position and velocity of the heliogyro, demonstrating that the NKO is closed as no discontinuities occur. The cone angle of the heliogyro is shown in Figure B.5c, highlighting that it is almost zero for the complete period of the NKO, slightly diverging at the end. The implementation of the coupled roto-translational dynamics of the heliogyro can therefore be considered verified as a closed NKO was generated, matching the expectations from [1].

B.1.4. Multiple Shooting algorithm

The correct implementation of the multiple shooting algorithm is verified by first testing the algorithm independently from the heliogyro cyclor problem, and later by testing the specific adaptation of the algorithm for the heliogyro cyclor problem.

Shooting problem

Firstly, the implementation is tested by optimizing a simple optimization problem where a projectile is launched and a target needs to be hit using minimum initial projectile speed. For the dynamical model controlling the motion of the projectile gravity and drag are modeled (drag coefficient of 0.4 and gravitational acceleration of 1 m/s^2), boundary conditions are set such that the projectile starts at the origin and reaches the target, and a RK4 integrator with a time-step of 10^{-2} seconds is used. A full description of the problem is given in [45].

The target is placed five meters away (horizontally) from the target. The trajectory is divided in five segments with the initial guess trajectory consisting of constant horizontal velocity (2.5 m/s) and a total trajectory time of two seconds. Constraint tolerances are set to 10^{-3} , with the convergence tolerances for both the objective function and the state vector set to 10^{-8} . The "SLSQP" optimization algorithm from Scipy [46] is selected as it is easily interfaceable, suitable for the non-linear problem and can handle multiple equality and inequality constraints. Nonetheless, note that the focus of this test is on the transcription algorithm and any other Non-Linear Programming (NLP) solver that can handle multiple constraints would have sufficed.

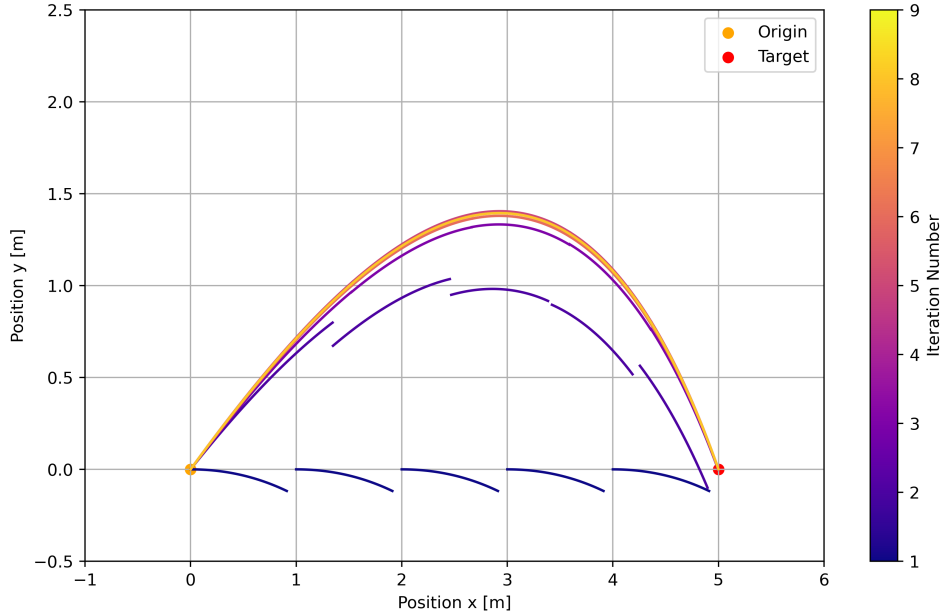
The resulting trajectories are shown in Figure B.6, also visualizing the initial guess trajectory (in blue) and the intermediate steps (various colors). The main expected features of the multiple shooting transcriptions are clear: in the initial iterations the segments are separated (defect constraints not satisfied) and the target is missed (final boundary condition not satisfied). With increasing iteration number, the trajectory gets more and more continuous, up to the final one (in yellow) where no discontinuities are visible and the target is hit. The initial velocity and trajectory period of the optimal results are tabulated in Table B.1. It is clear how the period, horizontal velocity, and vertical velocity were increased from the initial guess to satisfy the constraints and boundary conditions. As the problem converged successfully and all constraints and boundary conditions are achieved, the multiple shooting algorithm transcription can be considered verified. Further validation with benchmark problems (assessing the optimality of the solution) is presented later in subsection B.2.2.

Heliogyro Jacobian analysis

In order to verify the specific implementation of the heliogyro cyclor problem with the multiple shooting algorithm, the Jacobian matrix $\frac{\partial \mathbf{f}}{\partial \boldsymbol{\chi}}$ of the fitness vector \mathbf{f} (objective, boundary conditions and constraints) relative to the design vector $\boldsymbol{\chi}$ needs to be verified.

Table B.1: Optimal result of the verification problem.

Variable	V_x [m/s]	V_y [m/s]	Δt [s]
Value	2.82	2.22	3.31

**Figure B.6:** Visualization of the verification problem iteration process.

The Jacobian matrix as computed in the paper is compared to the one obtained through numerical differences (scaled step of 10^{-8}). The comparison between the two is shown in Figure B.7 for a optimal control problem as described in section 3 of chapter 2, but with three segments per phase instead of 48 to reduce computational time. The heliogyro states and control inputs used for this validation are selected arbitrarily to be similar to the expected trajectories and are tabulated in Table B.2.

Firstly, the similarities between the Jacobian computed as presented in the paper and the numerical one (Figures a and b) are clear, as the same pattern is present. A sparsity pattern similar to the one from the paper can be recognized. The errors between the numerical and multiple-shooting algorithm Jacobian entries are shown in figure c, where a maximum error of less than 10% is found. This error is associated with the State Transition Matrix (STM) of the first segments of each phase, which can be attributed to non-linearities in the problem. Increasing the number of segments will decrease the non-linearities and therefore the error in the Jacobian.

Consequently, the implementation of the Jacobian for the specific heliogyro problem can be considered verified, demonstrating that the multiple shooting transcription behaves as expected both for a general problem and the specific one tackled in this research work. Validation of the algorithm by comparing it to benchmark solutions and a simple heliogyro test problem is presented later in subsection B.2.2

B.2. Validation

In this section the validation procedures for the models and algorithms implemented for this research work are presented. The validation method is based on the comparison of the obtained results with well-known analytical results or results from external research. Note that validation of the SRP force and movement models is not performed directly as no such analytical model exists for the heliogyro, but it is indirectly validated by validating the heliogyro dynamics.

Table B.2: States and controls used for heliogyro problem validation. All values scaled as explained in the paper, positions in AU, velocity in AU/syn periods, angles in radians, angular speeds in RPM.

		\mathbf{X}_r						\mathbf{U}_r		
		\mathbf{r}_1	\mathbf{r}_2	$\dot{\mathbf{r}}_1$	$\dot{\mathbf{r}}_2$	ϕ	ω_3	a_{co}	a_{hp}	a_{cy}
EM phase	Segment 1	1	0	0	13	π	0.26	0	0	$\frac{1}{18}\pi$
	Segment 2	0	1.2	-12	0	$\frac{3}{2}\pi$	0.26	0	0	$\frac{1}{18}\pi$
	Segment 3	-1.5	0	0	-10.8	2π	0.26	0	0	$\frac{1}{18}\pi$
ME phase	Segment 1	0	-1.5	10.8	0	$\frac{1}{2}\pi$	0.26	0	0	$\frac{1}{18}\pi$
	Segment 2	1.2	0	0	12	π	0.26	0	0	$\frac{1}{18}\pi$
	Segment 3	0	1	-13	0	$\frac{3}{2}\pi$	0.26	0	0	$\frac{1}{18}\pi$

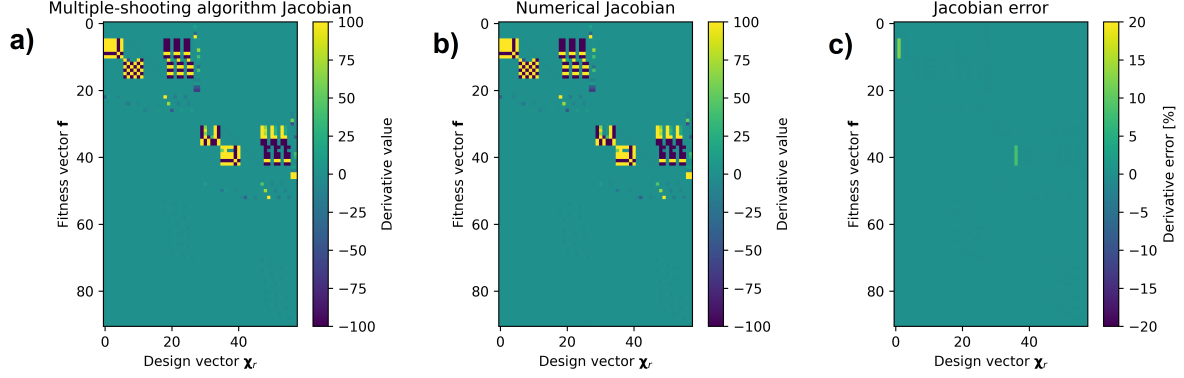


Figure B.7: Visualization of resulting Jacobian and associated errors, multiple shooting implementation in plot a), fully numerical one in b), and the difference in c).

B.2.1. Dynamics

The dynamics are validated by analyzing separately the translational and rotational dynamical models.

Translational dynamics

Firstly, the translational dynamics are validated by reproducing Figure 4.17 from [1], where a spiral trajectory from Earth to Mars is simulated (through an analytical model based on logarithmic spirals, the same as the one used in section 5.2 of chapter 2). By reproducing these results, the translational model can be considered validated as both gravitational and SRP accelerations need to be correctly modeled to obtain the same trajectory.

As stated in [1], a solar sail with a lightness number β of 0.05 is used, with all pitch profiles set to zero (reducing the heliogyro to a fixed-area solar sail). The departure sailcraft positions from the figure are used, with the starting velocity computed as [1]:

$$\begin{aligned}
 v_{tang} &= \sqrt{\frac{\mu_{\odot}}{r}} [1 - \beta \cos^2 \alpha (\cos \alpha - \tan \gamma \sin \alpha)]^{1/2} \cos \gamma \\
 v_{rad} &= \sqrt{\frac{\mu_{\odot}}{r}} [1 - \beta \cos^2 \alpha (\cos \alpha - \tan \gamma \sin \alpha)]^{1/2} \sin \gamma \\
 \gamma &= \arctan \left(\frac{2\beta \cos^2 \alpha \sin \alpha}{1 - \beta \cos^3 \alpha} \right)
 \end{aligned} \tag{B.5}$$

with v_{rad} as the radial velocity, v_{tang} as the tangential one, and setting the cone angle α to the optimal value of $35.26deg$ [1]. The initial state is propagated for the transfer time computed from Equation 43 from chapter 2 using an RK4 integrator with a time-step of 1 day. The resulting trajectory is shown and compared to the one from literature [1] in Figure B.8. It is clear that the two trajectories match, as they end at the same point and have the same shape, therefore the translational dynamics can be considered validated.

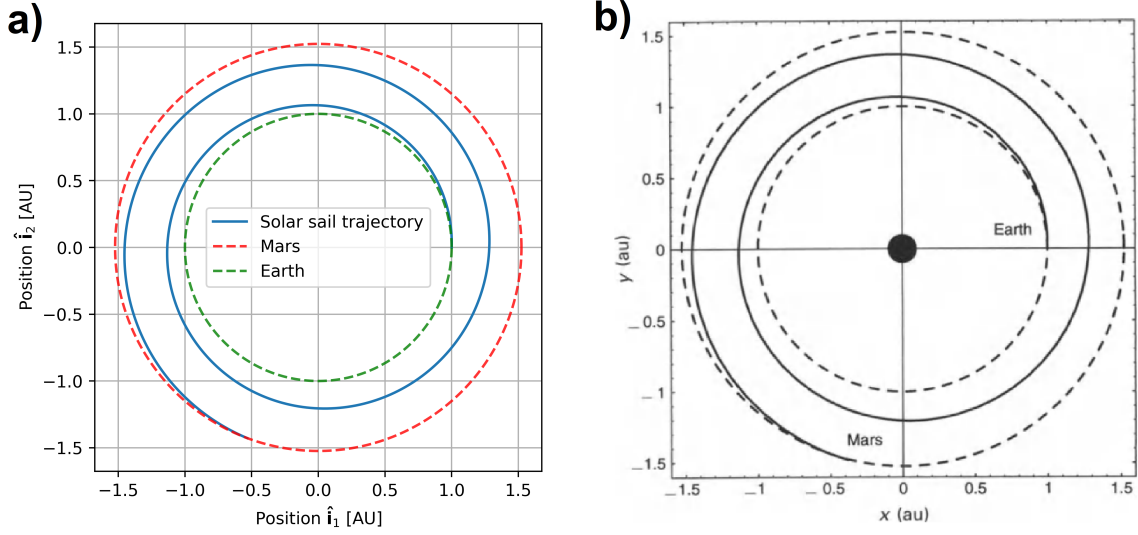


Figure B.8: Comparison between propagated Earth-Mars spiral trajectory in a) and trajectory from [1] in b).

Rotational dynamics, torque-free

The rotational dynamics is validated by simulating two cases with known analytical solutions. Firstly, the non-averaged rigid body rotational dynamics are validated by comparing numerical results to the analytical solution of the torque-free motion of an axis-symmetric body (like the heliogyro).

The analytical solutions presented in [11] and [47] need to be re-adapted for an Euler 3-2-3 attitude representation (like the one used in this research work). First, in order to simply the problem, the initial conditions of the heliogyro are selected such that the angular momentum of the spacecraft $\mathbf{H}^{[I]}$ is aligned with \hat{i}_3 , by enforcing:

$$\mathbf{H}^{[B]} = \begin{bmatrix} J_1\omega_1 \\ J_2\omega_2 \\ J_3\omega_3 \end{bmatrix}^{[B]} = \mathbf{R}_{B/I}\mathbf{H}^{[I]} = \mathbf{R}_{B/I} \begin{bmatrix} 0 \\ 0 \\ H \end{bmatrix} = H \begin{bmatrix} -s\theta c\psi \\ s\theta s\psi \\ c\theta \end{bmatrix} \quad (\text{B.6})$$

The initial Euler angle ϕ is set to zero, while from the last row of the equation it is clear that the Euler angle θ is constant (as the spin-rate ω_3 is constant due to the axis-symmetry of the body) and can be computed from the selected angular rates. The spin-rate of the heliogyro is set to 0.26 Rotations Per Minute (RPM), with the non-spin angular rate $\omega_{1,2}$ as:

$$\omega_{1,2} = \sqrt{\omega_1^2 + \omega_2^2} = 0.05 \text{ RPM} \quad (\text{B.7})$$

The angular velocities can be obtained by using the inverse of Equation A.3 and noting that $\dot{\theta}$ is zero:

$$\begin{aligned} \omega_1(t) &= -\dot{\phi} \sin(\theta) \cos(\psi(t)) \\ \omega_2(t) &= \dot{\phi} \sin(\theta) \sin(\psi(t)) \\ \omega_3(t) &= \dot{\psi} + \dot{\phi} \cos(\theta) \end{aligned} \quad (\text{B.8})$$

Substituting the relations from Equation B.8 in Equation 17 from chapter 2 and noting that ω_3 is constant due to the axis-symmetry of the heliogyro, the Euler angles are found as:

$$\begin{aligned} \phi(t) &= \phi(t_0) + \dot{\phi}t = \frac{J_3\omega_3}{J \cos(\theta)}t \\ \psi(t) &= \psi(t_0) + \dot{\psi}t = \psi(t_0) + \frac{(J - J_3)\omega_3}{J}t \end{aligned} \quad (\text{B.9})$$

with J_3 as the spin-axis Mass Moment Of Inertia (MMOI), J as the MMOI of the other axes, t as time and t_0 as initial time.

Using the baseline heliogyro design presented in chapter 2, the initial state is numerically propagated (using an RK4 integrator and 0.1 seconds time-step) for 500 seconds. The difference between the analytical solution is visualized in Figure B.9. It is immediately clear that the numerical solution matches the analytical one very well, with negligible differences that can be attributed to numerical integration and round-off errors.

Generalized rotational dynamics

In order to validate the non-averaged dynamics in the presence of SRP moments, the analytical solution presented in [12] for the “Spinning Sailcraft with a CM/CP Offset” (corresponding to a case with a constant lateral moment) is adapted for an Euler 3-2-3 attitude representation and compared to the numerical solution obtained by propagating the non-averaged rotational dynamics. The analytical solution is obtained starting from Equation 9 of chapter 2, setting $M_{\hat{\mathbf{b}}_2}$ and $M_{\hat{\mathbf{b}}_3}$ to zero (assuming only a lateral moment around $\hat{\mathbf{b}}_1$), omitting the superscript notation for simplicity and defining $\lambda = \frac{J-J_3}{J}\omega_3$. The time derivative of the angular velocity can be rewritten as:

$$\begin{bmatrix} \dot{\omega}_1 \\ \dot{\omega}_2 \end{bmatrix} = \begin{bmatrix} \lambda\omega_2 + \frac{M_1}{J} \\ -\lambda\omega_1 \end{bmatrix} \quad (\text{B.10})$$

Using Equation A.3 and setting $\theta(t_0) = 0.5\pi$:

$$\begin{bmatrix} \dot{\phi} \\ \dot{\theta} \\ \dot{\psi} \end{bmatrix} = \begin{bmatrix} -\cos(\psi)\omega_1 + \sin(\psi)\omega_2 \\ \sin(\psi)\omega_1 + \cos(\psi)\omega_2 \\ \omega_3 \end{bmatrix} \quad (\text{B.11})$$

Defining $a = \frac{M}{J}$, the solution to Equation B.10 when $\omega_1(0) = \omega_2(0) = 0$ is:

$$\begin{bmatrix} \omega_1 \\ \omega_2 \end{bmatrix} = \begin{bmatrix} \frac{a}{\lambda} \sin(\lambda t) \\ -\frac{a}{\lambda} (1 - \cos(\lambda t)) \end{bmatrix} \quad (\text{B.12})$$

Solving Equation B.11 similarly as [12], the analytical solution is found:

$$\begin{bmatrix} \phi \\ \theta \\ \psi \end{bmatrix} = \begin{bmatrix} \frac{aJ}{\lambda J_3 \omega_3} [1 - \cos(\frac{\omega_3 J_3}{J} t)] + \frac{a}{\lambda \omega_3} [\cos(\omega_3 t) - 1] + \phi(t_0) \\ \frac{aJ}{\lambda J_3 \omega_3} \sin(\frac{J_3 \omega_3}{J} t) - \frac{a}{\lambda \omega_3} \sin(\omega_3 t) + \theta(t_0) \\ \omega_3 t \end{bmatrix} \quad (\text{B.13})$$

The validation scenario is run using the baseline heliogyro design presented in chapter 2, with the initial Euler angles set as $\phi = \pi$, $\theta = 0.5\pi$, $\psi = 0$, and all angular velocities set to zero except the spin-rate $\omega_3 = 0.26$ RPM. The initial conditions are propagated (using an RK4 integrator and a 0.01 second time-step) for 500 seconds and the difference between the numerical and analytical solutions is visualized in Figure B.10. Angular rates and Euler angle variations are periodic and consequently overlap in Figure B.10a and b. As shown in Figure B.10c, the differences are minor and can be attributed to integration errors, round-off errors, and assumptions of the analytical model (see [12] for more information).

Overall, the non-averaged model has been validated for torque-free and constant torques cases, the only cases with simple analytical solutions. In addition, the averaged rotational model has been also validated for an heliogyro interplanetary trajectory by comparing it to the validated non-averaged one, in section 6.3 of chapter 2.

B.2.2. Multiple shooting

Validating the multiple shooting algorithm is performed in two complementary ways: firstly, the multiple shooting algorithm is tested on a known optimal control problem (not related to the heliogyro) with a well-known optimal solution, to assess if optimal convergence is achieved; secondly, a simple case for the heliogyro is constructed such that the optimal solution is known, and the multiple shooting algorithm is tested comparing the numerical solution with the expected solution.

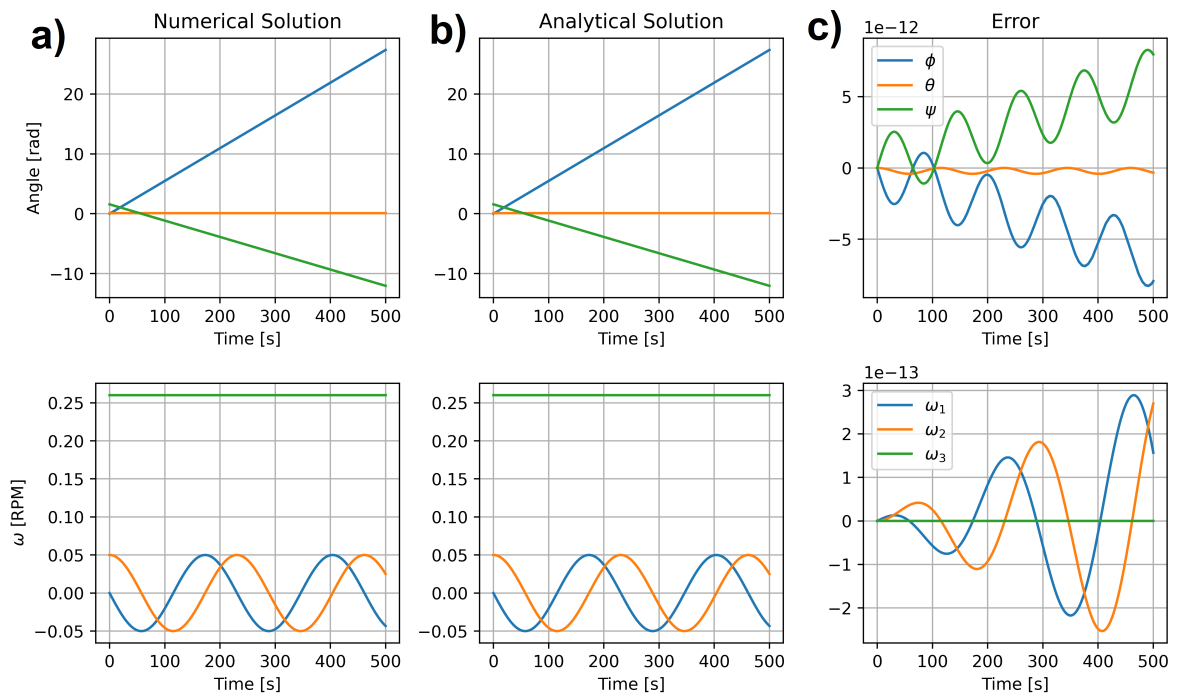


Figure B.9: Difference between analytical and numerical solution for torque free motion of an axis-symmetric body. Figure a) (top and bottom row) shows the numerical solution, b) the analytical one, and c) the difference between the two.

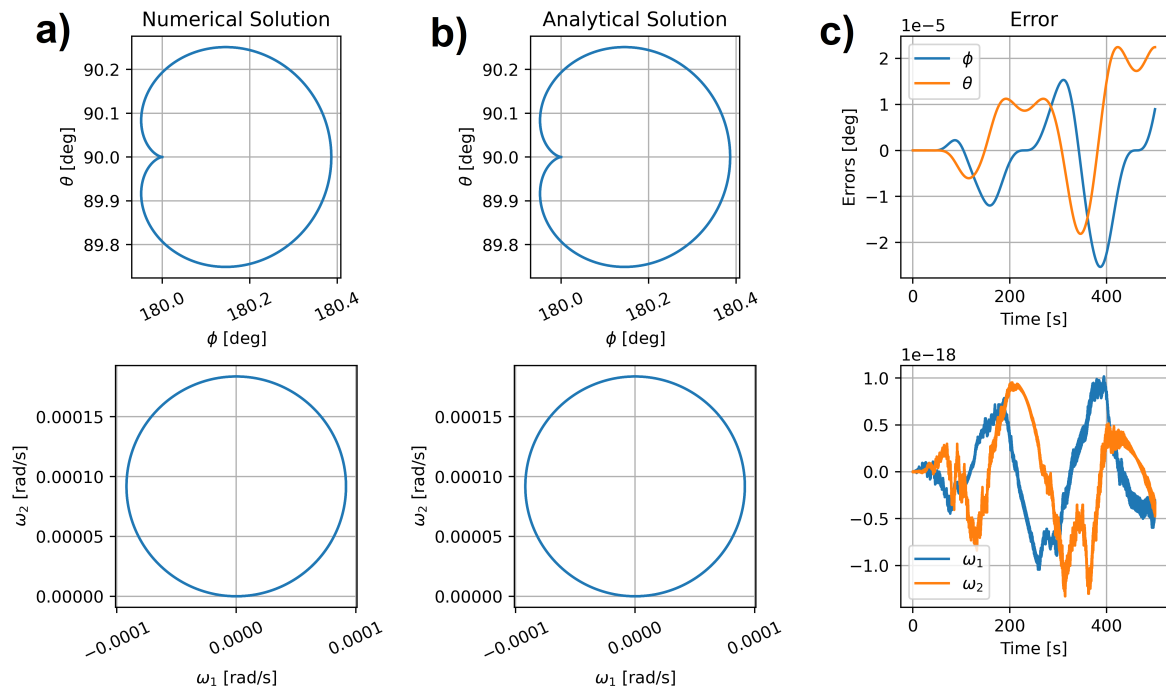


Figure B.10: Difference between analytical and numerical solution for constant lateral moment motion of spinning sailcraft. Figure a) (top and bottom row) shows the numerical solution, b) the analytical one, and c) the difference between the two.

Goddard's rocket problem

Firstly, the algorithm is tested on a well-known benchmark optimal control problem, Goddard's rocket problem, tackling the optimal control of one-dimensional rocket ascension when the rocket is subject to gravitational forces and atmospheric drag. The problem formulation and relevant parameters parameter are taken from [48] in order to compare to the provided benchmark solution. The control goal is to reach a certain final altitude r_f minimizing the fuel consumption (equivalent to maximizing the final mass). The problem is described as [48]:

$$\begin{array}{ll}
 \min_{m,r,v,u,T} & -m(T) \\
 \text{State derivatives} & \dot{r} = v \\
 & \dot{v} = -\frac{1}{r^2} + \frac{1}{m} (T_{\max} u - \Lambda(r, v)) \\
 & \dot{m} = -bT_{\max} u \\
 \text{Control variable} & u(t) \in [0, 1] \\
 \text{Boundary conditions} & r(0) = r_0 \\
 & v(0) = v_0 \\
 & m(0) = m_0 \\
 & r(T) = r_f \\
 \text{Path constraint} & \Lambda(r, v) \leq C
 \end{array} \tag{B.14}$$

with r , v , and m as the state variables, describing altitude, speed and mass respectively. $u(t)$ is the control input representing the thrust level, T_{\max} is the maximum thrust and b is a constant related to the mass-rate. Constant C is the maximum achievable drag, while the drag Λ is computed as:

$$\Lambda(r, v) := Av^2\rho(r), \text{ with } \rho(r) := e^{-k \cdot (r-r_0)} \tag{B.15}$$

with k as a scale-height constant, A as the cross-sectional area and ρ as the atmospheric density.

The values of all parameters are given in Table B.3. With those parameters, the benchmark optimal objective is -0.63389 [48].

Table B.3: Parameters of Goddard's rocket 1D problem [48].

Parameter	r_0	v_0	m_0	r_f	b	T_{\max}	A	k	C
Values	1	0	1	1.01	7	3.5	310	500	0.6

The initial guess is generated by setting the thrust level always at maximum value and the duration of the trajectory to a value of 0.05 (following the normalization by the problem). The trajectory is split into 200 segments and an RK4 integrator with a step size of 10^{-4} is used to propagate the segments. The resulting optimal trajectory has an objective value of -0.63389 (the same as the benchmark solution) and is plotted in Figure B.11. Note that the visualized benchmark solution does not reach the required height in the figure as it had to be traced from the plot in [48], which led to some errors (no numerical solution was provided). Nonetheless, it is clear that the optimal solution reaches the target altitude and traces the shape of the benchmark solution well, with a few minor differences in the mid part of the trajectory, probably due to numerical reasons related to the transcription. As the benchmark objective value as provided by [48] is reached, the multiple shooting algorithm is considered validated.

Heliogyro sample problem

In order to validate the algorithm for the specific heliogyro problem treated in this research work, another validation case is performed. Using the baseline heliogyro design, the values in Table B.4 as initial state, and all pitch profiles control input set to zero, the initial state is propagated for 30 days (using an RK4 integrator with a time-step of roughly 7 hours) to generate a benchmark trajectory to follow. The benchmark trajectory is split in ten segments and perturbed using a random normal distribution with uncertainties from Table B.4.

Table B.4: Initial state, control and perturbation for the heliogyro multiple shooting validation.

Parameter	\mathbf{r}	$\dot{\mathbf{r}}$	ϕ	ω_3	\mathbf{u}	t_t
Initial states	[1,0]	[15,28]	180	0.26	[0,0,0]	30
Perturbation ($1-\sigma$)	[0.05,0.05]	[0.5,0.5]	10	0	10	0
Units	AU	km/s	deg	RPM	deg	days

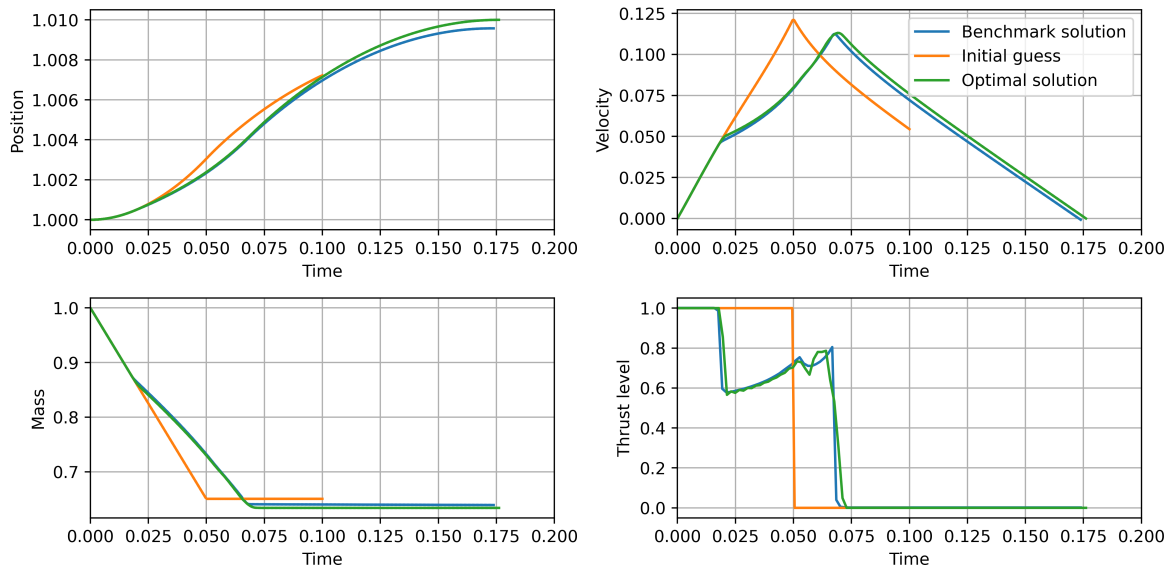


Figure B.11: Benchmark, initial and optimal solution trajectory related to the 1D Goddard's rocket problem [48].

The perturbed trajectory is then used as an initial guess for an optimal control problem with the boundary condition set-up such that the initial and final point of the benchmark trajectories need to be matched and with the objective of minimizing the squared sum of all pitch profile inputs (thereby trying to re-create the benchmark trajectory as close as possible).

The benchmark, perturbed and optimal trajectories are shown in Figure B.12 where it is clear that the optimal trajectories overlap with the benchmark trajectories as desired. This is further confirmed by the fact that all control inputs are within 0.15 degrees (not shown), close to the ideal value of zero. The multiple shooting algorithm can therefore be considered validated also for the specific case of the heliogy problem studied in this research work.

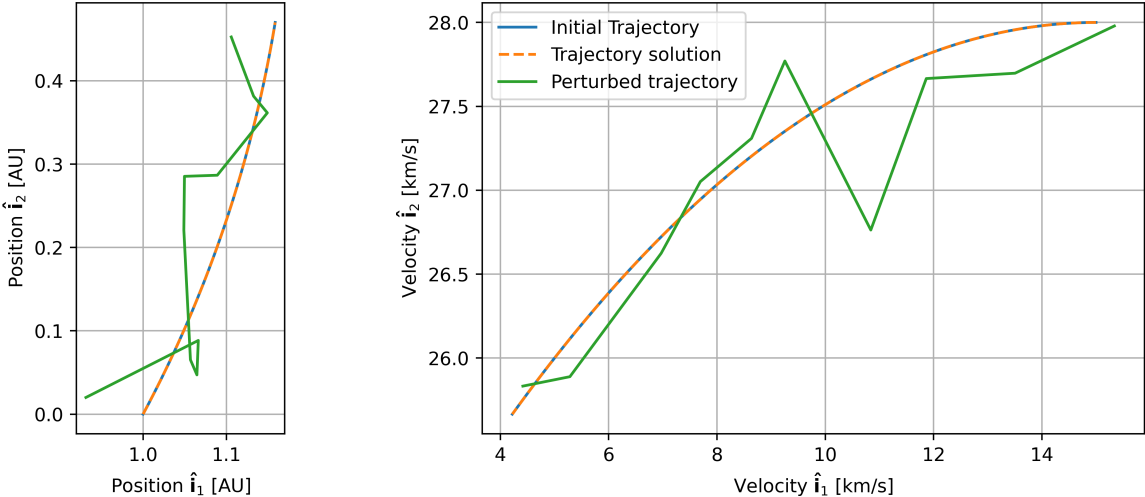
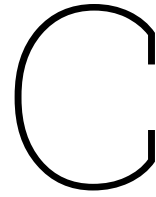


Figure B.12: Initial, perturbed and optimal solution trajectory related to the multiple shooting algorithm validation.



Numerical parameters selection

The rationale behind the selection of the values for various numerical parameters used in this research work are presented in this appendix. Firstly, the selection of the constraint tolerance value is presented in section C.1, followed by the selection the integrator step in section C.2. The selection of the number of steps for the computation of the SRP forces and moments is presented in section C.3, while the selection of the numerical steps used in the computation of the finite differences numerical derivatives is explained in section C.4.

C.1. Constraint tolerance selection

The tolerance values are selected considering the accuracy of the adopted models: as most of them are low-fidelity, it is not useful to have strict tolerances as they would simply increase the computational effort without increasing the fidelity.

The fidelity of the adopted models is therefore analyzed. The maximum ephemerides error due to the non-modelled Martian orbital inclination for the co-planar trajectories is approximately 0.05 AU. In addition, Earth and Mars's spheres of influence (where the gravitational influence of the planet exceeds the Sun's gravitational influence) have a radius of approximately 6×10^{-3} AU and 3×10^{-3} AU, respectively.

As a consequence of this, the constraints tolerance for the boundary conditions and defect constraints related to positions are set to a conservative value of 10^{-4} AU, one order of magnitude smaller than the sphere of influence values listed earlier. For simplicity, the tolerance for all other constraints is also set to the same value, noting that scaled velocities and Euler angles have higher amplitude than the positions and therefore the velocity constraints will introduce less inaccuracies compared to the position constraints with the same tolerance.

C.2. Integrator step selection

The time-step of the RK4 integrator is selected to have integration errors for each segment with a comparable order of magnitude as the constraints tolerance (scaled values of 10^{-4}). In order to analyze the integrator error as a function of time-step, two scenarios representing the EM and Mars-Earth (ME) legs are propagated with different time-steps. The baseline heliogyro design from chapter 2 is used with the sailcraft placed on the $\hat{\mathbf{t}}_1$ axis at Earth's and Mars's distance from the Sun (depending on the leg), with circular orbit velocity (to match the planetary departure states), and the sail normal perpendicular to the sunlight direction. All pitch profiles are set to zero, except for the half-p amplitude (which generates lateral moments) set to one degree (arbitrary value) to simulate the need of rotating the sailcraft as it revolves around the Sun. Each trajectory is propagated for the expected segment duration, assuming a transfer time of 0.55 (as described in section 6.1 from chapter 2) and 48 segments per leg.

Results for time-steps ranging from 10^{-2} to 10^{-5} synodic periods are shown in Figure C.1, computing the final position error for one segment, relative to a more accurate solution (10^{-6}). From the figures it is clear that the integration error behavior follows the expected truncation error for a fixed-step integrator (linear in log-log space). A time-step of 10^{-3} is selected as it corresponds to a position error value of 10^{-4} AU for the segment of the EM leg, the one with larger errors.

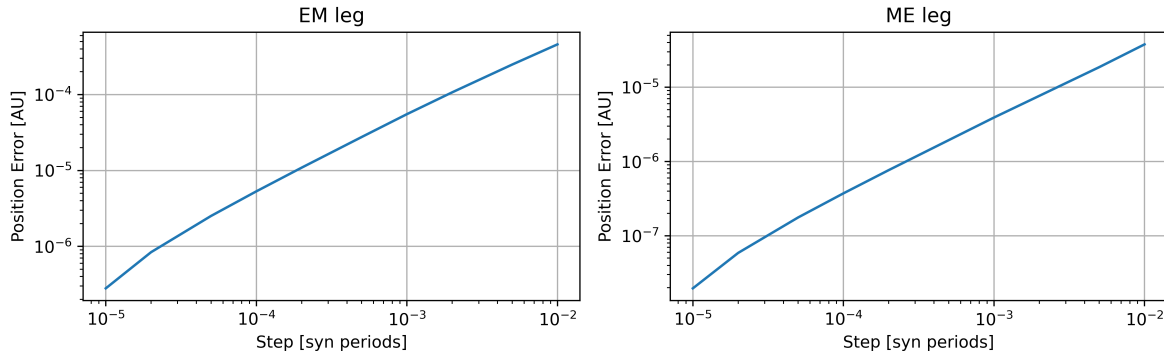


Figure C.1: Final position error analysis as a function of integrator time-step, for segments in the EM and ME leg.

C.3. Average force/ moment computation step selection

The computation of the average SRP forces and moments requires numerical integration, as explained in section 2.4 of chapter 2. The trapezoidal rule is used for the numerical integration as it simple and was used for the same application in the *HGForce* algorithm from [22, 37]. The selection of the number of steps to be used for the trapezoidal rule is a trade-off between accuracy and computational effort. The adopted SRP force model (and therefore also the SRP moment one model) is already low-fidelity and ignores non-ideal optical effects, wrinkles, and sail deformation, which can induce significant errors in the SRP force, in the order of 10 to 20% [42]. Therefore, for the selection of the number of steps, more priority is put on low computational effort.

The error of the SRP force and moment computation is analyzed as a function of the number of integration steps to select an appropriate number of steps. The relative error x_{err} is computed as:

$$x_{err} = \frac{x - x_{base}}{x_{base}} \quad (C.1)$$

where x is the force or moment and x_{base} is the baseline value (assumed to be as close to reality as possible) computed with 200 integration steps. The corresponding error in acceleration and derivatives of the Euler angles is also computed using the relations from chapter 2. Errors are computed using the baseline heliogyro design from chapter 2, placing the sailcraft 1 AU away from the Sun with the sail perpendicular to the incoming sunlight. The results are shown in Figure C.2, displaying the mean and 95th percentile obtained by computing the error for different pitch profiles, sampling amplitudes and phases from a random uniform distribution between $\pm\pi$.

As shown in the figures, the relative errors in force and moments are well below the expected errors due to the low-fidelity SRP force model. In addition, the resulting maximum expected errors in acceleration and Euler angle derivatives are small, indicating that the influence on the resulting trajectory is quite limited. Consequently, the number of integration steps selected is 50, which is a good compromise between accuracy and low computational effort, considering the fact that high accuracy is not needed.

C.4. Numerical derivative step selection

The multiple shooting algorithm relies on the numerical computation of some of the state derivatives which cannot be obtained analytically, as explained in section 5.1 of chapter 2. The selection of the step is therefore critical to avoid injecting unwanted errors in the optimization process.

The Jacobian matrices $\frac{\partial \dot{\mathbf{X}}(t, \mathbf{X}(t))}{\partial \mathbf{X}(t)}$ and $\frac{\partial \dot{\mathbf{X}}(t, \mathbf{X}(t))}{\partial \mathbf{u}(t)}$, associated with the dynamical model and contributing to the creation of the State Transition and Sensitivity matrices, are computed through numerical differentiation. The entries of these matrices are therefore analyzed as a function of the differentiation step adopted for both position and angle (the two most influential components of the states on the matrices entries), using the baseline heliogyro design from chapter 2, placing the sailcraft 1 AU away from the Sun with the sail perpendicular to the incoming sunlight.

The variation of selected Jacobian matrices entries as a function of the numerical step is shown in Figure C.3. The selected matrix entries are displayed as they are the most influential entries of the

matrices, but the other entries also display similar behavior. As expected, for small steps the numerical round-off error dominates, resulting in an error in the derivative value, while for large steps the truncation errors due to non-linearities dominate. The central plateaux represent the ideal regions to evaluate the numerical derivatives (as they minimize errors). Consequently, the step for the position is set to 10 km, while the one for angles is set to 10^{-6} radians.

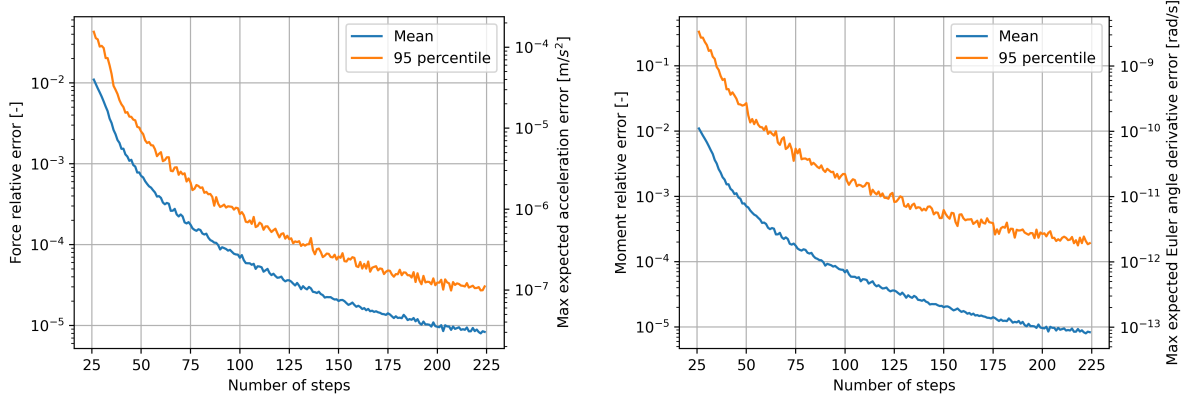


Figure C.2: Averaged SRP force and moment model errors as a function of numerical integration steps.

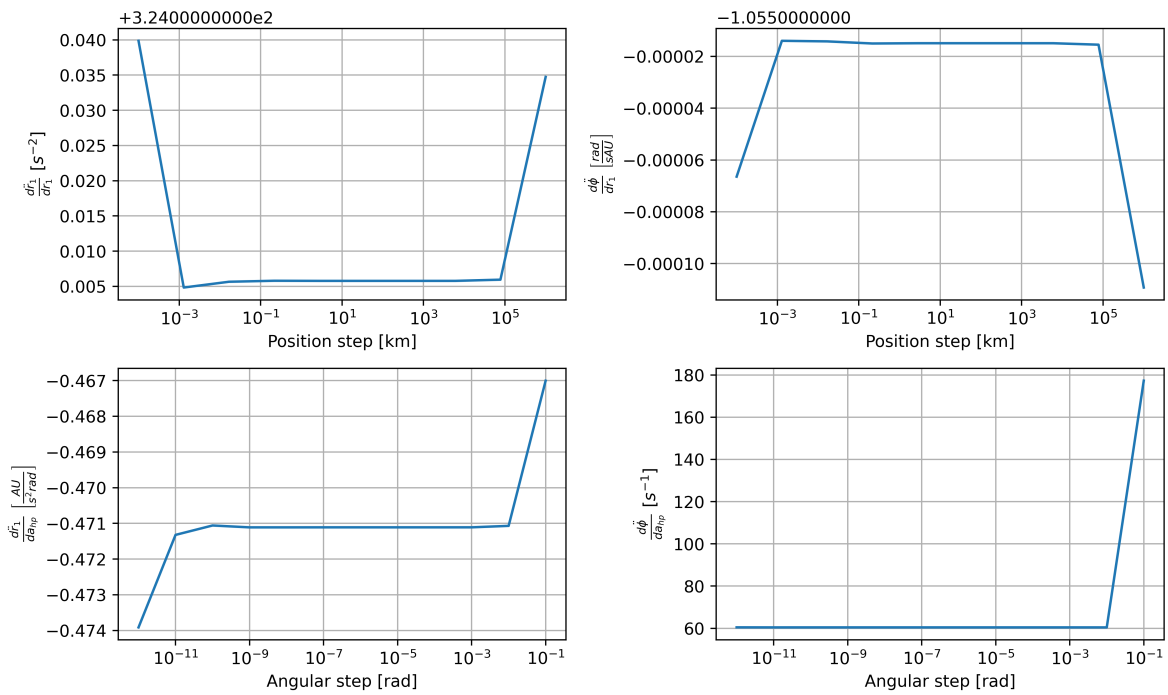


Figure C.3: Sensitivities of numerical derivative to numerical steps.